Doctoral Dissertation

Innovative study on non-tidal environmental variations of the Seto Inland Sea by the external forcing

（外部強制により瀬戸内海に発生する非潮汐周期環境変動に関する先端的研究）

September 2015

Graduate School of Engineering

Hiroshima University

Chuanzheng Zhang

TABLE OF CONTENTS

Chapter 1 Introduction

1.1 Present status in coastal sea observations

As have been seen, oceans cover more than 70 percent of the earth surface, and the oceans play a key role in the change of world's climate, but information on the ocean is still restricted in both space and time. Oceanographers have been making continuous effort to accumulate the knowledge on the ocean. At present, there are two fundamental ways to learn about the ocean: field observation [Wunsch, 2002] and numerical simulation model [Blumberg and Mellor, 1987]. Field observation is an unique method to know what occur in the ocean, and serves to validate the performance of numerical model. Recently, observation data are incorporated into the ocean circulation model as an initial condition to give in situ data to the model and the time growth of the ocean is proceeded by the model until the acquisition of next observation data. Prediction values by the models are updated with the next observation data. This is the procedure of data assimilation based on the ensemble Kalman filter [Evensen, 1994]. Close collaboration of observation and model is an essential point of data assimilation.

Observations are particularly difficult in the coastal sea around Japan with heavy fisheries activity and shipping traffic. One point and ship track observation are possible by small ships equipped with the shipboard conductivity, temperature and depth (CTD) system and acoustic Doppler current profiler (ADCP). The distribution of current and temperature is severely deformed because it is reconstructed from data, obtained with changing time. More systematic oceanographic observation can be performed on the basis of moored instruments. However the execution of such moored observations is quite difficult because of the constraints imposed by heavy fisheries and shipping traffic.

Remote sensing technique is applicable to the coastal seas, using both electric-

magnetic waves and sound waves. Coastal-sea current can be measured by high-frequency (HF) radars, located on a coast although measurement is restricted to the surface [Maul, 1985; Robinson, 1985; Stewart, 1985]. The HF radar is not suited to the coastal seas with complicated shorelines and scales smaller than 10 km. Also the expensive cost imposed on the HF radar is not balanced to coastal sea studies usually supported by smaller funds. Coastal acoustic tomography (CAT) is another innovative remote sensing technique because coastal seas are transparent for sound waves. The coastal sea is characterized with a sophisticated fluid system in which dynamical processes and phenomena occur over a wide range of space and time scales. Furthermore subsurface measurement is critical to make a progress because there are internal-mode phenomena such as internal tides and waves, coastal fronts and density currents.

1.2 Coastal Acoustic Tomography (CAT)

The ocean acoustic tomography (OAT) was proposed as a key technology to map the 3D mesoscale structure of temperature and current by using a long-range underwater sound transmission [Munk and Wunsch, 1979; Munk et al., 1995]. The tomography can make a snapshot of current and temperature over the observation domain because of the rapid spatial coverage by using sound speed. The first experiment was performed by the OAT Group to measure mesoscale eddies from travel times between several source-receiver pairs [Ocean Tomography Group, 1982]. The eddy fields which were reconstructed by the inverse analysis were validated by the shipborne and airborne surveys. The early measurement demonstrated the feasibility of sound transmission to measure an average temperature, using the integrating nature of sound transmission. The ocean tide [Dushaw, et al., 2011; Stammer, et al. 2014], shallow-bay internal scattering [Apel, et al., 1997] and deep convection [Worcester, et al, 1993] were also measured by the OAT. The OAT made the largest advantage on the mapping (snap shot) of rapidly

varying phenomena like deep convection.

When compared with the deep sea, shallow-sea sound transmission is much complicated by bottom reflection. In the shallow sea, environmental changes strongly interact with people's lives, but the systemic observation of environments are so difficult owing to heavy fisheries activity and shipping traffic. CAT provides an intelligent way to monitor coastal environments inside an observation domain, surrounded by multi-stations. The CAT system, which is a coastal-sea application of OAT, has been constructed and operated by the Hiroshima University Group since 1993. They successfully applied it to the measurement of current and temperature structures in the coastal and inland seas.

In 1995, a reciprocal sound transmission experiment was performed between the two acoustic stations in Neko-Seto of the Seto Inland Sea. In comparison with the ADCP data, the feasibility of current measurement by the CAT was validated [Zheng et al., 1997a; Zheng, 1997b; Zheng et al., 1998]. The reciprocal sound transmission method, which has been applied to the measurement of current profiles in the deep sea [Worcester, 1977; Worcester, et al,1985; Howe, et al,1987], was also proposed as a proven method to make cross-channel measurement of current and temperature in straits and channels [Send, et al, 2002; Adityawarman, et al, 2011; Adityawarman, et al, 2012]. By using the reciprocal sound transmission method (the simplest unit of CAT system), sudden variations in current and river discharge caused by the passage of Qiantang river’s tidal bores were successfully captured [Zhu, et al., 2012].

On the basis of the reciprocal sound transmission method, the multi-station measurement of current structures were performed by the pioneering works of the Hiroshima University Group. By using the multi-station travel time data, the horizontal distribution of current were reconstructed by the function-expansion inverse method, based on the damped least squares method. The results showed that the CAT is an accurate and efficient observational method for continuously mapping tidal current structures in the coastal seas [Yamaoka et al., 2002; Yamaguchi et al., 2005; Zhu, et al., 2013].

Beside the horizontal-slice studies, vertical-slice measurement of currents is another challenge which was executed in the Kuroshio Origin (Luzon Strait and East-of-Taiwan) [Taniguchi et al., 2010; Taniguchi et al., 2013]. The inverse method for the vertical slice was developed using the Kuroshio origin data.

1.3 Seto Inland Sea environments influenced by external forcing (Kuroshio and typhoon)

The Seto Inland Sea is the largest inland sea in Japan, facing the Pacific Ocean with the Kuroshio Current at the western and eastern inlets (the Bungo and Kii Channels, respectively) and surrounded by three of the Japanese main islands (Honshu, Kyushu and Shikoku). All regions of the inland sea are characterized by strong tidal current which flows among one thousand islands [Yanagi et al, 1982] and developed as fishing grounds. Part of the Kuroshio Current intrudes into the Seto Inland Sea sporadically through the Bungo and Kii Channels and significantly influences the inland sea environment [Akiyama and Saitoh, 1993; Takeuchi, et al,1998]. However, direct observation of the Seto Inland Sea throughflow has never been attempted. The throughflow is a splendid target of the reciprocal sound transmission method because long-term measurement by other methods are hopeless [Zhang et al., 2015b].

Hiroshima Bay, located in the western part of the Seto Inland Sea, is the biggest oyster aquaculture field in Japan. The bay is elliptical, with a north-south length of 50 km and an east-west length of 10 km. The northern part of the bay is semi-enclosed (for about 10 km) by the coast of Hiroshima City on the northern side and three islands (Miyajima, Etajima and Ninoshima) on the southern side. Dynamic events such as anomalous sea level rises (ASLRs), internal seiches and coastal upwelling are known to occur in Hiroshima Bay. The measurement of such dynamic events is quite difficult without using

a multi-station of CAT, distributed to surround the bay [Zhang et al., 2014; Zhang et al., 2015a].

All the previous inverse analyses on a horizontal slice were performed to reconstruct current structures [Yamaoka, et al, 2002; Yamaguchi, et al, 2005; Zhu et al. 2013]. In this study, an inverse analysis is first applied to the variations of temperature structures, reconstructing the horizontal-slice structures of coastal upwelling and the associated internal tides [Zhang et al., 2015a]. The pronounced environmental events which occur in Hiroshima Bay are strongly linked with winds due to typhoons passing the east of the bay (one of external forcing).

1.4 Outline

This thesis is intended to study the environmental changes of the Seto Inland Sea (Aki-nada Sea and Hiroshima Bay) by the external forcing such as the Kuroshio and typhoon. The Seto Inland Sea throughflow and the anomolous sea level rise (ASLR) associated with coastal upwelling, internal tides and internal seiches in Hiroshima Bay are environmental events to be studied. This thesis is composed of the following chapters. In Chapter 2, methods and formulation are described. The regularized inversion accompanied by the grid method are introduced as a method for both horizontal and vertical slices. A position correction method which is required for temperature measurement is also proposed. Environmental variations of the Seto Inland Sea by the external forcing are presented in Chapters 3, 4 and 5. Chapter 3 describes the ASLRs which often occurs during the spring tide along the north shore of Hiroshima Bay in September after the blowing of strong northerly wind due to the typhoon. Chapter 4 is devoted to report the long-term measurement of the Seto Inland Sea throughflow in Aki-nada Sea. Chapter 5 describes coastal upwelling and the associated internal tides generated in the northern part of Hiroshima Bay by the typhoon which passes east of the

bay. The regularized inversion accompanied by the grid method is presented for reconstructing the horizontal distribution of temperature. Integrated discussion and conclusions are presented in Chapters 6 and 7, respectively.

References

Adityawarman, Y., A. Kaneko, K. Nakano, N. Taniguchi, K. Komai, X. Guo, and N. Gohda. (2011). Reciprocal sound transmission measurement of mean current and temperature variations in the central part (Aki-nada) of the Seto Inland Sea, Japan, *J. Oceanogr*. **67**, 173-182.

Adityawarman, Y., A. Kaneko, N. Taniguch, H. Mutsuda, K. Komai, X. Guo, and N. Gohda. (2012). Tidal current measurement in the Kurushima Strait by the reciprocal sound transmission method, *Acoustical Science and Engineering*, **33**, 45-51.

Akiyama, H. and S. Saitoh. (1993). The Kyucho in Sukumo Bay induced by Kuroshio warm filament intrusion. *J. Oceanogr.*, **49**, 667-682.

Apel, J. R., M. Badiey, C. S. Chiu, S. Finette, R. Headrick, J. Kemp, J. F. Lynch, A. Newhall, M. H. Orr, B. H. Pasewark, D. Tielbuerger, A. Turgut, K. von der Heydt, and S. Wolf. (1997). An overview of the 1995 SWARM shallow-water internal wave acoustic scattering experiment, 1997, *IEEE Journal of Oceanic Engineering,* **22**: 465-500.

Blumberg, A. F. and G. L. Mellor. (1987). A description of a three-dimensional coastal ocean circulation model. Three-Dimensional Coastal Ocean Models, edited by N. Heaps, 208 pp., American Geophysical Union.

Dushaw, B. D., P. F. Worcester and M. A. Dzieciuch. (2011). On the predictability of mode-1 internal tides, *Deep-Sea Res.*, *Part Ⅱ*, **58**, 677–698.

Evensen, G. (1994). Sequential data assimilation with a nonlinear quasi-geostrophic model using Monte Carlo methods to forecast error statistics, *J. Geophys. Res.*, **99**, 10143-10162.

Howe, B. M., P. F. Worcester, and R. C. Spindel. (1987). Ocean acoustic tomography: Mesoscale velocity, *J. Geophys. Res.*, **92**, 3785-3805.

Maul, G. A. (1985). Introduction to Satellite Oceanography, 599 pp, Martinus Nijhoff

Publishers, Dordrecht.

Munk, W. and C. Wunsch. (1979). Ocean acoustic tomography: a scheme for large scale monitoring, *Deep-Sea Res.*, **26A** , 123-161.

Munk, W., P. F. Worceser, and C. Wunsch. (1995). Ocean acoustic tomography, 433pp, Cambridge Univ. Press, Cambridge.

Ocean Tomography Group. (1982). A demonstration of ocean acoustic tomography, *Nature*, **299**, 121-125.

Robinson, I. S. (1985). Satellite oceanography: An introduction for oceanographers and remote-sensing scientists. 455 pp, Ellis Horwood Ltd, Chichester.

Stewart, R. H. (1985). Methods of Satellite Oceanography. 360 pp, University of California Press, Berkeley.

Send, U., P. Worcester, B. Cornuelle, C. Tiemann and B. Baschek. (2002). Integral measurement of mass transport and heat content in the Strait of Gibraltar from acoustic transmissions, *Deep-Sea Res., Part Ⅱ*, **49**, 4069-4095.

Stammer, D., R. D. Ray, O. B. Andersen, B. K. Arbic,W. Bosch, L. Carrère, Y. Cheng, D. S. Chinn, B. D. Dushaw, G. D. Egbert, S. Y. Erofeeva, H. S. Fok, J. A. M. Green, S. Griffiths, M. A. King, V. Lapin, F. G. Lemoine, S. B. Luthcke, F. Lyard, J. Morison, M. Müller, L. Padman, J. G. Richman, J. F. Shriver, C. K. Shum, E. Taguchi and Y. Yi. (2014). Accuracy assessment of global barotropic ocean tide models, *Reviews of Geophysics*, **52**, 243–282.

Takeuchi, J., N. Honda, Y. Morikawa, T. Koike and Y. Nagata. (1998). Bifurcation current along the southwest coast of the Kii Peninsula. *J. Oceanogr.*, **53**, 45-52.

Taniguchi, N., A. Kaneko, Y. Yuan, N. Gohda, H. Chen, G. Liao, C. Yang, M. Minamidate, Y. Adityawarman, X.-H. Zhu, and J. Lin. (2010). Long-term acoustic tomography measurement of ocean currents at the northern part of the Luzon Strait, *Geophys. Res. Lett.*, **37**, L07601.

Taniguchi, N., C.-F. Huang, A. Kaneko, B. M. Howe, Y.-H. Wang, Y. Yang, J. Lin, X.-H. Zhu and N. Gohda. (2013). Measuring the Kuroshio Current with ocean acoustic tomography, *J. Acoust. Soc. Am.*, **134**, Pt.2: 3272-3281.

Worcester, P. F., J. F. Lynch, W. M. L. Morawitz, R. Pawlowicz, P. J. Sutton, B. D. Cornuelle, O. M. Johannessen, W. H. Munk, W. B. Owens, R. Shuchman and R. C. Spindel. (1993). Evolution of the large-scale temperature field in the Greenland Sea during 1988-1989 from tomographic measurements, *Geophys. Res. Lett,* **20**: 2211-2214.

Worcester, P. F. (1977). Reciprocal acoustic transmission in a midocean environment, *J. Acoust. Soc. Am.*, **62**, 895–905.

Worcester, P. F., R. C. Spindel and B. M. Howe. (1985). Reciprocal acoustic transmissions: Instrumentation for mesoscale monitoring of ocean currents, *IEEE J. Oceanic Eng.*, **OE-10**, 123-137.

Wunsch C. (2002). Ocean observations and the climate forecast problem. In: Meteorology at the Millennium, Edited by R.P. Pearce. London: Royal Meteorological Society: 233–245.

Yamaguchi K., J. Lin, A. Kaneko, T. Yamamoto, N. Gohda, H.-Q. Nguyen and H. Zheng. (2005). A continuous mapping of tidal current structures in the Kanmon Strait, *J. Oceanogr.*, **61**, 283-294.

Yamaoka H., A. Kaneko, J.-H. Park, H. Zheng, N. Gohda, T. Takano, X.-H. Zhu and Y. Takasugi. (2002). Coastal acoustic tomography system and its field application, *IEEE Journal of Oceanic Engineering*, **27**, 283-295.

Yanagi, T., H. Takeoka and H. Tsukamoto. (1982). Tidal energy balance in the Seto Inland Sea, *J. Oceanogr. Soc. Jpn*, **38**, 293-299.

Zhang, C.-Z, A. Kaneko, X.-H. Zhu and J. Lin. (2014). Non-tidal sea level changes in Hiroshima Bay, Japan, *Acta Oceanologica Sinica*., **33**, 47-55.

Zhang, C.-Z, A. Kaneko, X.-H. Zhu and N. Gohda. (2015a). Tomographic mapping of a coastal upwelling and the associated diurnal internal tides in Hiroshima Bay, Japan, *J. Geophys. Res.*, doi: 10.1002/2014JC010676.

Zhang, C.-Z, A. Kaneko, K. Komai, X.-H Zhu, B M. Howe and N. Gohda. (2015b). Acoustic measurement of the net transport through the Seto Inland Sea, *Acoustical Science and Technology* (in press).

Zheng, H., N. Gohda, H. Noguchi, T. Ito, H. Yamaoko, T. Tamura, Y. Takasugi and A, Kanko. (1997a). Reciprocal Sound Transmission Experiment for Current Measurement in the Seto Inland Sea, Japan, *J. Oceanogr.*, **53**, 117-127.

Zheng, H. (1997b). Study on Development and Application of the Coastal Acoustic Tomography System, *Doctor Dissertation*, Hiroshima Univ., 115pp.

Zheng, H., H. Yamaoko, N. Gohda, H. Noguchi, and A. Kanko. (1998). Design of the acoustic tomography system for velocity measurement with an application to the coasral sea, *J. Acoust. Soc. Jpn.* **19**, 199-210.

Zhu, X.-H., C.-Z. Zhang, Q.-S. Wu, A. Kaneko, X.-P. Fan and B. Li. (2012). Measuring discharge in a river with tidal bores by use of the coastal acoustic tomography system, *Estuarine, Coastal and Shelf Sci.*, **104-105**: 54-65.

Zhu, X.-H. , A. Kaneko, Q.-S. Wu, C.-Z. Zhang, N. Taniguchi, and N. Gohda. (2013). Mapping Tidal Current Structures in Zhitouyang Bay, China, Using Coastal Acoustic Tomography, *IEEE J. Oceanic Eng.*, **38**, 285-296.

Chapter 2 Method and formulation

2.1 Forward formation

We shall consider the reciprocal sound transmission between the acoustic stations S1 and S2, as shown in Fig.2.1.1. The traveling rays are refracted, forming the upper and lower turning points. The refracted ray paths depend on the vertical profiles of sound speed and current velocity [Munk et al., 1995]. The environmental factors (sound speed and current velocity) which influence sound transmission can be measured in the observational domain through which sound signals pass. The reciprocal travel times $t_i^{\pm}$ along the i-th ray path can be expressed by:

$$t_i^{\pm} = \int_{\Gamma_i^{\pm}} \frac{dL}{C_0(z) + \delta C(x,z) \pm v_s(x,z)} \qquad (2.1)$$

where the superscripts + and – indicate the positive and negative directions between S1 and S2, dL is the arc length along the rat path. The $C_0(z)$, $\delta C(x,z)$ and $v_s(x,z)$ represent the reference sound speed, sound speed deviation and current velocity along the ray path, respectively. The $\Gamma_i^{\pm}$ indicate the i-th ray path in the reciprocal sound transmission between the two stations.

The reference travel time along the i-th ray path Γ_{0i} can be calculated through the numerical simulation, using the reference sound speed C_0, calculated by using the CTD data in the observation domain and the sound speed formula [MacKenzie, 1981].

$$t_{0i} = \int_{\Gamma_{0i}} \frac{dL}{C_0(z)} \qquad (2.2)$$

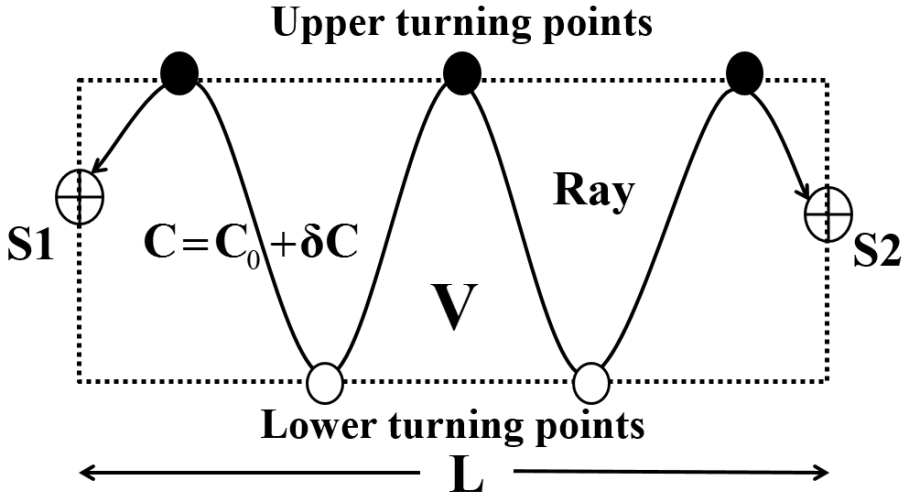

Fig.2.1.1 Sketch of the reciprocal sound transmission between S1 and S2. The upper and lower turning points are shown with the solid and blank circles.

Taking the subtraction of (2.2) from (2.1), and considering $C_0(z) >> \Delta C(x,z)$, $C_0(z) >> v_s(x,z)$ and $\Gamma_i^{\pm} \approx \Gamma_{0i}$, we obtain the reciprocal travel time deviation [Yamaguchi et al., 2005]:

$$\tau_i^{\pm} = t_i^{\pm} - t_{0i} = \int_{\Gamma_i^{\pm}} \frac{dL}{C_0(z) + \delta C(x,z) \pm v_s(x,z)} - \int_{\Gamma_{0i}} \frac{dL}{C_0(z)}$$
$$\approx -\int_{\Gamma_{0i}} \frac{(\delta C(x,z) \pm v_s(x,z))}{(C_0(z))^2} dL \qquad (2.3)$$

The differential ($\Delta\tau_i$) and mean travel time deviation ($\delta\tau_i$) for the i-th ray path can be expressed by:

$$\Delta\tau_i = \tau_i^+ - \tau_i^- = -2\int_{\Gamma_{0i}} \frac{\mathrm{v}_s(x,z)}{\left(C_0(z)\right)^2} dL$$

$$\delta\tau_i = \tau_i^+ + \tau_i^- = -2\int_{\Gamma_{0i}} \frac{\delta C(x,z)}{\left(C_0(z)\right)^2} dL \qquad (2.4a,b)$$

In the analysis of travel time data, the range-averaged current must require reciprocal travel time data and strict clock accuracy, whereas the range-averaged sound speed (temperature) can be calculated with strict positioning accuracy from one-way travel time data [Munk et al., 1995]. The accurate position is very important for temperature calculation, so the new position correction method will be proposed later. Data gaps can be greatly reduced by using one-way data. By considering one-way travel time and neglecting the effect of current in sound transmission, equation (2.1) can be approximated by

$$t_i = \int_{\Gamma_{0i}} \frac{dL}{C_0(z) + \delta C(x,z)} \qquad (2.5)$$

where t_i is one-way travel time obtained along the i-th ray path. Subtracting (2.2) from (2.5) and approximating Γ_i by Γ_{0i}, we obtain the travel time deviation:

$$\delta\tau_i = t_i - t_{0i} \approx -\int_{\Gamma_{0i}} \frac{\delta C(x,z)}{\left(C_0(z)\right)^2} dL \qquad (2.6)$$

The error, caused by the current effect will be discussed in the Charpter5.

2.2 Inverse analyses

2.2.1 Grid method

We shall here introduce the inverse analyses for reconstructing the horizontal-slice distribution and the layered profile on the vertical slice of sound speed deviation and current. The configuration of station position and ray paths are sketched in Fig. 2.2.1 for the horizontal slice and Fig. 2.2.2 for the vertical slice. For both the horizontal and vertical slice inversions, we shall divide the tomography domain into a series of rectangular grids, numbered with $j = 1, 2, \cdots, N$. From Eqs 2. 4(a) and (b), the differential ($\Delta\tau_i$) and mean travel time deviation ($\delta\tau_i$) for the i-th ray path reduce in a discrete form:

$$\Delta\tau_i = -2\int_{\Gamma_{0i}} \frac{\mathrm{v}_s(x,z)}{\left(C_0(z)\right)^2} dL = -2\sum_{j=1}^{N} \frac{l_{ij} v_j}{C_{0j}^{\ 2}} \qquad (i = 1, 2, \cdots, M)$$

$$\delta\tau_i = -2\int_{\Gamma_{0i}} \frac{\delta C(x,z)}{\left(C_0(z)\right)^2} dL = -2\sum_{j=1}^{N} \frac{l_{ij} \delta C_j}{C_{0j}^{\ 2}} \qquad (j = 1, 2, \cdots, N) \quad (2.7a,b)$$

where v_j and δC_j denote the velocity and sound speed deviation for the j-th sub- domain (layer), respectively. C_{0j} is the reference sound speed for the j-th sub-domain (layer) and l_{ij} the arc length of the i-th ray crossing the j-th sub-domain (layer).

2.2.2 Regularized inversion

In the matrix form, the equations (2.7a,b) reduce

$$\mathbf{y} = \mathbf{E}\mathbf{x} + \mathbf{n} \qquad (2.8)$$

where $\mathbf{y} = \{\Delta\tau_i\}$ *or* $\{\delta\tau_i\}$, $\mathbf{E} = \left\{\frac{-2l_{ij}}{C_{0j}^{\ 2}}\right\}$, $\mathbf{x} = \{v_j\}$ *or* $\{\delta C_j\}$ and $\mathbf{n} = \{n_i\}$.

The horizontal-slice and vertical-slice distributions of the sound speed and current deviation are reconstructed by the regularized inversion, which was proposed in geo-tomography [Rajan et al., 1987]. The cost function (**J**) consists of the data misfit and smoothness measure (**H**) of the solution vector (**x**):

$$\mathbf{J} = (\mathbf{y} - \mathbf{E}\mathbf{x})^{\mathbf{T}} (\mathbf{y} - \mathbf{E}\mathbf{x}) + \lambda \mathbf{x}^{\mathbf{T}}\mathbf{H}^{\mathbf{T}}\mathbf{H}\mathbf{x} \qquad (2.9)$$

where $\boldsymbol{\lambda}$ is the Lagrange multiplier. The two-order derivative factor **S** may be expressed by:

$$\mathbf{S}(\mathbf{x}) = \nabla^2 x = \mathbf{x}^{\mathbf{T}}\mathbf{H}^{\mathbf{T}}\mathbf{H}\mathbf{x} \qquad (2.10)$$

where ∇^2 is the Laplacian multiplier. The weighted average of the solution with the smoothness factor **H** is required for the grid method to suppress biases, whereas the smoothing process is implicitly embedded in the function expansion method [Yamaoka et al., 2002; Yamaguchi et al., 2005]. Note that the selection method of smoothness factor **H** is different between the horizontal and vertical slices.

a) Horizontal slice

For the horizontal slice, the inversion problem is configured as a case with M ray paths and N sub-domains. The typical arrangement of sub-domains and ray paths is illustrated in Fig.2.2.1 for the case of numbers 6 and 9, respectively.

By using five neighboring subdomains, the two-order derivative factor S may be expressed by:

$$\mathbf{S}(\mathbf{x}) = \nabla^2 \mathbf{x} = \sum\left(\mathbf{x}_{i,j-1} + \mathbf{x}_{i-1,j} - 4\mathbf{x}_{i,j} + \mathbf{x}_{i,j+1} + \mathbf{x}_{i+1,j}\right) = \mathbf{x}^T\mathbf{H}^T\mathbf{H}\mathbf{x} \tag{2.11}$$

$$\mathbf{H} = \begin{bmatrix} -4 & 1 & 0 & 1 & 0 & 0 & 0 & 0 & 0 \\ 1 & -4 & 1 & 0 & 1 & 0 & 0 & 0 & 0 \\ 0 & 1 & -4 & 0 & 0 & 1 & 0 & 0 & 0 \\ 1 & 0 & 0 & -4 & 1 & 0 & 1 & 0 & 0 \\ 0 & 1 & 0 & 1 & -4 & 1 & 0 & 1 & 0 \\ 0 & 0 & 1 & 0 & 1 & -4 & 0 & 0 & 1 \\ 0 & 0 & 0 & 1 & 0 & 0 & -4 & 1 & 0 \\ 0 & 0 & 0 & 0 & 1 & 0 & 1 & -4 & 1 \\ 0 & 0 & 0 & 0 & 0 & 1 & 0 & 1 & -4 \end{bmatrix} \tag{2.12}$$

The weighted average of solution **H** for the case of Fig. 2.2.1 is required to suppress the side and corner effects of sub-domains.

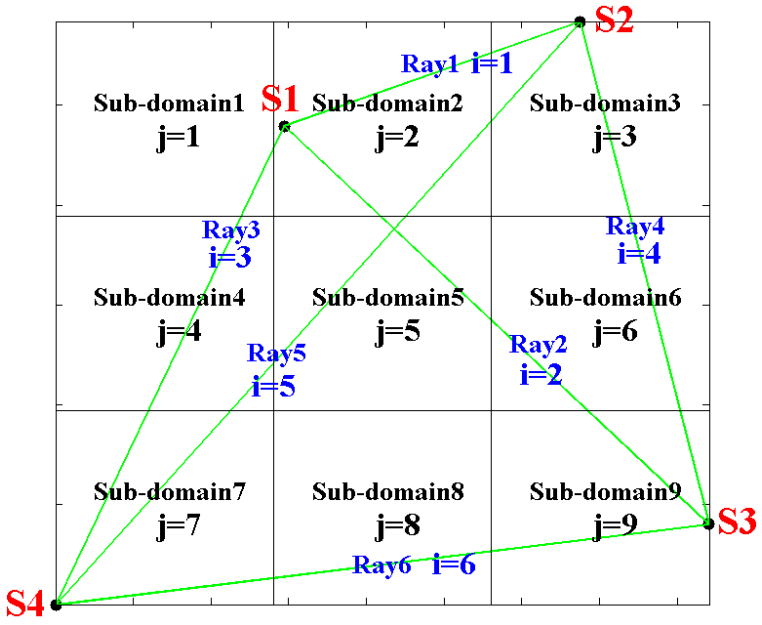

Fig.2.2.1 Horizontal-slice case with six ray paths and nine rectangular sub-domains.

Owing to the insufficient smoothing, two kinds of weighting factors ($\beta 1$ and $\beta 2$) are imposed on the corner sub-domains (1, 3, 7 and 9) and the side sub-domains (2, 4, 6 and 8), respectively. In consideration of the additional weighting factors, equation (2.9) is rewritten as:

$$\mathbf{J} = (\mathbf{y}-\mathbf{Ex})^{\mathbf{T}} (\mathbf{y}-\mathbf{Ex}) + \lambda \mathbf{x}^{\mathbf{T}}\mathbf{H}^{\mathbf{T}} \boldsymbol{\beta} \mathbf{Hx} \qquad (2.13)$$

$$\boldsymbol{\beta} = \begin{bmatrix} \beta 1 & 0 & 0 & 0 & 0 & 0 & 0 & 0 & 0 \\ 0 & \beta 2 & 0 & 0 & 0 & 0 & 0 & 0 & 0 \\ 0 & 0 & \beta 1 & 0 & 0 & 0 & 0 & 0 & 0 \\ 0 & 0 & 0 & \beta 2 & 0 & 0 & 0 & 0 & 0 \\ 0 & 0 & 0 & 0 & 1 & 0 & 0 & 0 & 0 \\ 0 & 0 & 0 & 0 & 0 & \beta 2 & 0 & 0 & 0 \\ 0 & 0 & 0 & 0 & 0 & 0 & \beta 1 & 0 & 0 \\ 0 & 0 & 0 & 0 & 0 & 0 & 0 & \beta 2 & 0 \\ 0 & 0 & 0 & 0 & 0 & 0 & 0 & 0 & \beta 1 \end{bmatrix} . \qquad (2.14)$$

b) Vertical slice

As a minimum unit of the vertical-slice inversion, the slice is divided into five horizontal layers, spanned by two ray paths (Fig.2.2.2). The number of layers is counted from the end layer located near a ray with the smallest amplitude.

The inversion problem is configured for five horizontal layers and two ray paths (Fig.2.2.2). By using three sequential layers, the two-order derivative factor S may be expressed by:

$$\mathbf{S}(\mathbf{x}) = \frac{\partial^2 x}{\partial z^2} = \sum (\mathbf{x}_{i-1} - 2\mathbf{x}_i + \mathbf{x}_{i+1}) = \mathbf{x}^{\mathbf{T}}\mathbf{H}^{\mathbf{T}}\mathbf{Hx} \qquad (2.15)$$

$$\mathbf{H} = \begin{bmatrix} -2 & 1 & 0 & 0 & 0 \\ 1 & -2 & 0 & 0 & 0 \\ 0 & 1 & -2 & 1 & 0 \\ 0 & 0 & 1 & -2 & 1 \\ 0 & 0 & 0 & 1 & -2 \end{bmatrix} \qquad (2.16)$$

One more weighting factor (β) is here introduced to suppress the edge effects (layers 1, and 5).

$$\boldsymbol{\beta} = \begin{bmatrix} \beta & 0 & 0 & 0 & 0 \\ 0 & 1 & 0 & 0 & 0 \\ 0 & 0 & 1 & 0 & 0 \\ 0 & 0 & 0 & 1 & 0 \\ 0 & 0 & 0 & 0 & \beta \end{bmatrix} \qquad (2.17)$$

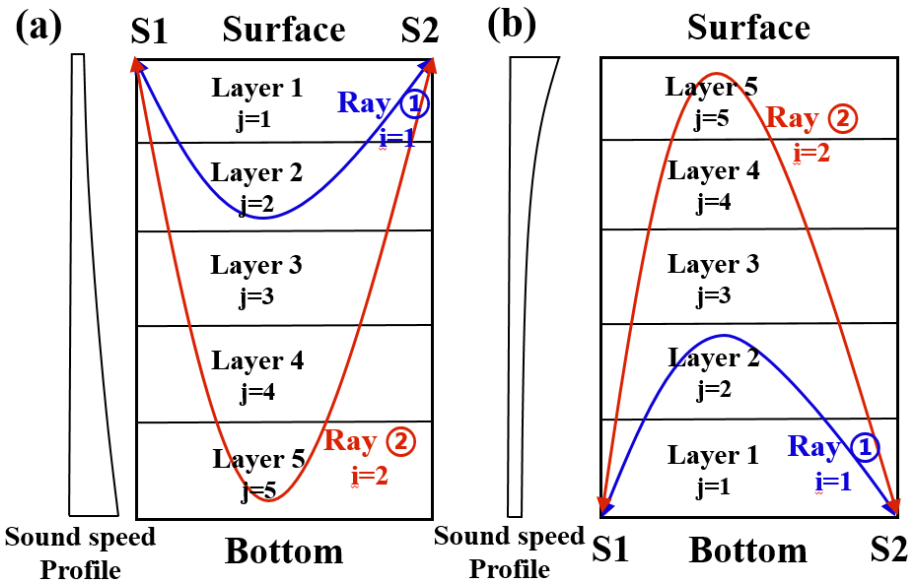

Fig.2.2.2 Numbering of the ray paths and the horizontal layers for two cases: (a) downward and (b) upward convex ray patterns.

c) Expected solution

For both cases of the horizontal and vertical slices, the expected solution is obtained by minimizing J

$$\hat{\mathbf{x}} = \left(\mathbf{E}^{\mathrm{T}}\mathbf{E} + \lambda\mathbf{H}^{\mathrm{T}}\boldsymbol{\beta}\mathbf{H}\right)^{-1}\mathbf{E}\mathbf{y} \qquad (2.18)$$

where $\boldsymbol{\lambda}$ is so chosen that the residual defined by $\|\hat{\mathbf{n}}\|^2 = \|\mathbf{y} - \mathbf{E}\hat{\mathbf{x}}\|^2$ is less than a predetermined value 0.14 $(\mathrm{ms})^2$ and 0.2 $(\mathrm{ms})^2$ for the sound speed and velocity inversion, corresponding to 0.05 ^{o}C for the 10-km range and 2.5 cm/s for the 10-km range, respectively.

This inversion gives the expected error of solution:

$$\hat{\mathbf{x}}_{\mathbf{e}} = \left(\mathbf{E}^{\mathrm{T}}\mathbf{E} + \lambda\mathbf{H}^{\mathrm{T}}\boldsymbol{\beta}\mathbf{H}\right)^{-1}\mathbf{E}\hat{\mathbf{n}} \qquad (2.19)$$

where $\hat{\mathbf{n}}$ denotes the expected travel time error.

2.3 Position correction method

Position correction is required because offsets exist between the subsurface acoustic transducer and the GPS antenna. A new method for correcting position is proposed here. This method uses one or two CTD datasets along each sound transmission line. The range (L_c) between acoustic transducers was estimated using $L_c = C_0 t$, where C_0 is the average sound speed calculated from the CTD data on the transmission lines and t is the acoustically observed travel time. Furthermore, this method requires that all transmission

lines (with the corrected lengths) are placed to create a focal point at each geographical transducer position.

For the case of four acoustic stations, the offset from the original position $\left(x_p,\ y_p\right)$ of the p-th station (determined by GPS) is expressed by $\left(\Delta x_p,\ \Delta y_p\right)$ in the (x, y) direction (where p=1, 2, 3, 5). The station-to-station ranges for all four corrected station positions $\left(x_p+\Delta x_p, y_p+\Delta y_p\right)$ are calculated from the following set of coupled equations:

$$\begin{aligned}
H1H2 &= \sqrt{(x_1+\Delta x_1-x_2-\Delta x_2)^2+(y_1+\Delta y_1-y_2-\Delta y_2)^2} = L_{c12} \\
H1H5 &= \sqrt{(x_1+\Delta x_1-x_5-\Delta x_5)^2+(y_1+\Delta y_1-y_5-\Delta y_5)^2} = L_{c15} \\
H2H3 &= \sqrt{(x_2+\Delta x_2-x_3-\Delta x_3)^2+(y_2+\Delta y_2-y_3-\Delta y_3)^2} = L_{c23} \\
H2H5 &= \sqrt{(x_2+\Delta x_2-x_5-\Delta x_5)^2+(y_2+\Delta y_2-y_5-\Delta y_5)^2} = L_{c25} \\
H3H5 &= \sqrt{(x_3+\Delta x_3-x_5-\Delta x_5)^2+(y_3+\Delta y_3-y_5-\Delta y_5)^2} = L_{c35} \quad .
\end{aligned} \tag{2.20}$$

Applying a Taylor expansion for $\left(\Delta x_q-\Delta x_p\right)<<\left(x_q-x_p\right)$ and $\left(\Delta y_q-\Delta y_p\right)<<\left(y_q-y_p\right)$, neglecting second and higher order terms, and substituting $\Delta x_5=\Delta y_5=0$ for station 5 (which is used as a reference point), equation (2.20) reduces to a first-order coupled equation with six unknown variables: Δx_k and Δy_k (where k=1, 2, 3), as follows:

$$\begin{aligned}
&\frac{\Delta x_1^{(n+1)}-\Delta x_2^{(n+1)}}{y_1^{(n)}-y_2^{(n)}}+\frac{\Delta y_1^{(n+1)}-\Delta y_2^{(n+1)}}{x_1^{(n)}-x_2^{(n)}} \approx \frac{L_{c12}{}^2-L_{12}^{(n)}{}^2}{2\left(x_1^{(n)}-x_2^{(n)}\right)\left(y_1^{(n)}-y_2^{(n)}\right)} \\
&\frac{\Delta x_1^{(n+1)}}{y_1^{(n)}-y_5^{(n)}}+\frac{\Delta y_1^{(n+1)}}{x_1^{(n)}-x_5^{(n)}} \approx \frac{L_{c15}{}^2-L_{15}^{(n)}{}^2}{2\left(x_1^{(n)}-x_5^{(n)}\right)\left(y_1^{(n)}-y_5^{(n)}\right)} \\
&\frac{\Delta x_2^{(n+1)}-\Delta x_3^{(n+1)}}{y_2^{(n)}-y_3^{(n)}}+\frac{\Delta y_2^{(n+1)}-\Delta y_3^{(n+1)}}{x_2^{(n)}-x_3^{(n)}} \approx \frac{L_{c23}{}^2-L_{23}^{(n)}{}^2}{2\left(x_2^{(n)}-x_3^{(n)}\right)\left(y_2^{(n)}-y_3^{(n)}\right)}
\end{aligned} \tag{2.21}$$

$$\frac{\Delta x_2^{(n+1)}}{y_2^{(n)} - y_5^{(n)}} + \frac{\Delta y_2^{(n+1)}}{x_2^{(n)} - x_5^{(n)}} \approx \frac{L_{c25}{}^2 - L^{(n)}{}_{25}{}^2}{2\left(x_2^{(n)} - x_5^{(n)}\right)\left(y_2^{(n)} - y_5^{(n)}\right)}$$

$$\frac{\Delta x_3^{(n+1)}}{y_3^{(n)} - y_5^{(n)}} + \frac{\Delta y_3^{(n+1)}}{x_3^{(n)} - x_5^{(n)}} \approx \frac{L_{c35}{}^2 - L^{(n)}{}_{35}{}^2}{2\left(x_3^{(n)} - x_5^{(n)}\right)\left(y_3^{(n)} - y_5^{(n)}\right)}$$

where the superscript (n) shows the iteration number. Equation (2.21) is numerically solved by the generalized inverse under the fixed ranges and the geographical positions are updated. This process is iterated to know better geographical position under the repeat update of the ranges. The proceeding of n is terminated when both $\left|\Delta x^{(n)}\right| < 10^{-3}$ and $\left|\Delta y^{(n)}\right| < 10^{-3}$ are satisfied. Note that the number of unknown variables are generally not equated to that of equations.

References

MacKenzie, K. V. (1981). Nine-term equation for sound speed in the ocean, *J. Acoust. Soc. Am.*, **70**, 807-812.

Munk, W., P. F. Worceser, and C. Wunsch. (1995). Ocean acoustic tomography, 433pp, Cambridge Univ. Press, Cambridge, U. K.

Rajan, S. D., J. F. Lynch and G. V. Frisk. (1987). Perturbative inversion methods for obtaining bottom geoacoustic parameters in shallow water, *J. Acoust. Soc. Am.*, **82**, 998–1017.

Yamaoka, H., A. Kaneko, J-H. Park, H. Zheng, N. Gohda, T. Takano, X-H. Zhu and Y. Takasugi. (2002). Coastal acoustic tomography system and its field application, *IEEE J. Oceanic Eng.*, **27**, 283-295.

Yamaguchi, K., J. Lin, A. Kaneko, T. Yamamoto, N. Gohda, H-Q. Nguyen and H. Zheng. (2005). A continuous mapping of tidal current structures in the Kanmon Strait, *J. Oceanogr.*, **61**, 283-294.

Chapter 3 Anomalous sea level changes in Hiroshima Bay

3.1 Introduction

This study is motivated by an anomalous sea level rise (hereinafter ASLR) that occurred along the north shore of Hiroshima Bay in calm weather at the spring tide of September 28, 2011. As the ASLR events synchronized with the spring tide in September, flood waters were over the floor level of the Itsukushima Shrine, constructed on the north shore of Miyajima Island in the northwestern part of Hiroshima Bay and preserved as one of world heritage sites (Fig.3.1.1). In this chapter the terminology “ASLR” is defined as an anomalous event which occurs in the sub-tidal range (2 day to 1 month) in Hiroshima Bay. Similar ASLR events accompanied by the flood water of the Itsukushima Shrine were reported on September 17, 2001 [Tokeshi and Yanagi, 2004] and September 25, 2003 (broadcast in TV and the newspapers). This chapter focuses on all ASLR events that occurred in September in several days after a typhoon passed the Pacific Ocean off the Kii Peninsula, located at about 400 km east of Hiroshima Bay.

Subsurface temperature variations due to internal modes are critical factors in the environmental management and protection in aquaculture fields like Hiroshima Bay with the biggest oyster aquaculture industry in Japan. Generally speaking, sea level changes due to steady internal modes are only 0.1% of their amplitudes and negligible in practical purposes [Lemmin et al., 2005; Hutter, 2012]. On the other hand, the upwelling and the associated sea level depression, generated transiently by the sporadic cross-shore wind (the northerly wind in Hiroshima Bay, opened southward), have been less studied although the anomalous sea level changes overwhelm the sea level change for the steady cases.

The non-tidal sea level changes in Hiroshima Bay are studied in the summation of all period range components: the sub-tidal (2 d to 1 month), intra-seasonal (1 month to 8

months), seasonal (8 months to 2 years) and inter-annual (>2 years), paying attention to the dynamics of sub-tidal range phenomena.

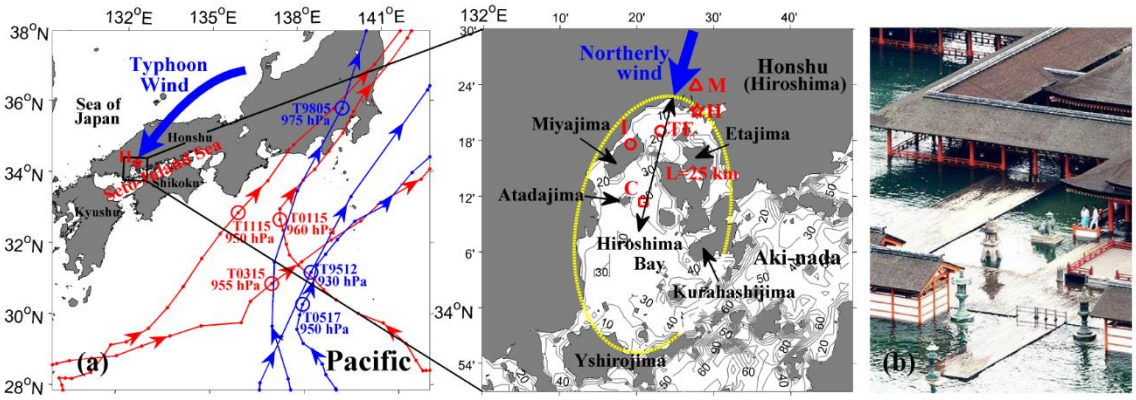

Fig. 3.1.1 *Map of the Seto Inland Sea and the adjacent regions (left). The typhoon trajectories are shown with the red lines for T0115, T0315, and T1115; and the blue lines for T9512, T9805, and T0517. The core position and moving direction of all the six typhoons are shown with a circle and arrow accompanied by the typhoon number and the air pressure. Hiroshima Bay opened southward (see the dashed curve) is shown in a magnified scale at the center of the figure. Point I is the Itsukushuma Shrine, which is preserved as one of world heritage sites; point H is the Hiroshima Tide Gauge Station of the Japan Coast Guard (JCG); M is the metrological station of JMA; and C is the station for the monthly CTD survey of HPTRI. Point TE is the position of the JCG buoy with a thermistor at 2 m. L (=25 km) is half of the north-south length of the bay. The contour interval is 10 m. The right panel shows a picture of the Itsukushima Shrine flooded in September 2011. The rough position of the typhoon-derived wind directed to Hiroshima Bay is indicated with a thick blue arrow in the figure.*

3.2 Site and methods

Hiroshima Bay, located in the western part of the Seto Inland Sea, is the biggest oyster aquaculture field in Japan (Fig. 3.1.1). The eastern and southern sides are also semi-enclosed by island chains (Kurahashi-jima to the east and Yashiro-jima to the south) with a gap at the southeast part. Such a sequence of shorelines makes us imagine half an ellipse with a north-to-south length of 25 km (see the dashed curve in Fig. 3.1.1). The narrow channel (Miyajima-seto) between Miya-jima with the Itsukushima Shrine (mark I in Fig. 3.1.1) and Eta-jima separates Hiroshima Bay into two parts (the narrower northern and the wider major regions). The major region has a relatively flat seafloor ranging from 20 to 30 m. By contrast, the floor depth is less than 20 m in the northern region.

The tide gauge station data over 21 years (1991-2011) for Hiroshima (mark H in Fig.3.1.1), provided by the Japan Coast Guard (JCG) with an interval of 30 s, are used to construct the hourly mean data. Then the hourly mean data are corrected with a conversion rate of 0.01 cm/Pa, using the air pressure data (explained later). The tidal components included in the pressure correction data are removed through the tide-killer filter [Hanawa and Mitsudera, 1985]. The resulting sea level data are processed through band-pass filters (Butterworth filters) including a (2 d to 1 month) filter, a (1 month to 8 months) filter, and a (8 months to 2 years) filter to pick up the sub-tidal component, intra-seasonal component and seasonal component, respectively. The inter-annual component is retrieved through a 2 year low-pass filter (Butterworth filter), and the long-term trend is provided with the regression line that includes the effect of global warming and ground level shift.

The sea level data are supplemented by atmospheric data (air pressure and wind speed) provided by the Hiroshima Branch of Japan Meteorological Agency (JMA) (mark M in Fig. 3.1.1). The data interval is one hour for data collected before June 25, 2008 and

10 min after that time. These data are used to make the air pressure corrections to the sea level data and also to calculate the wind speed blowing over the bay. The water temperature data at hourly intervals at 2 m depth are provided in the northern part of Hiroshima Bay from the JCG surface buoy, moored to make the shipping traffic safe (mark TE in Fig. 3.1.1).

3.3 Results

3.3.1 Low-frequency sea level variations

The hourly mean non-tidal sea level data with the pressure correction (SSHAC) are shown in Fig. 3.3.1a with the time plots together with the 2 year low-pass filtered data (inter-annual component). The resulting data oscillate in a range of about ±30 cm, implying that they are dominated by seasonal changes. The inter-annual component oscillates within a range of about ±10 cm, with a long-term trend of 4.9 mm/year. The vertical lines indicate the time when ASLRs occurred as post-typhoon events in Hiroshima Bay (six events in September during the last 21 years). The red vertical lines are assigned for the cases that the ASLR events were concomitant with the spring tide in several days after the corresponding typhoon passage.

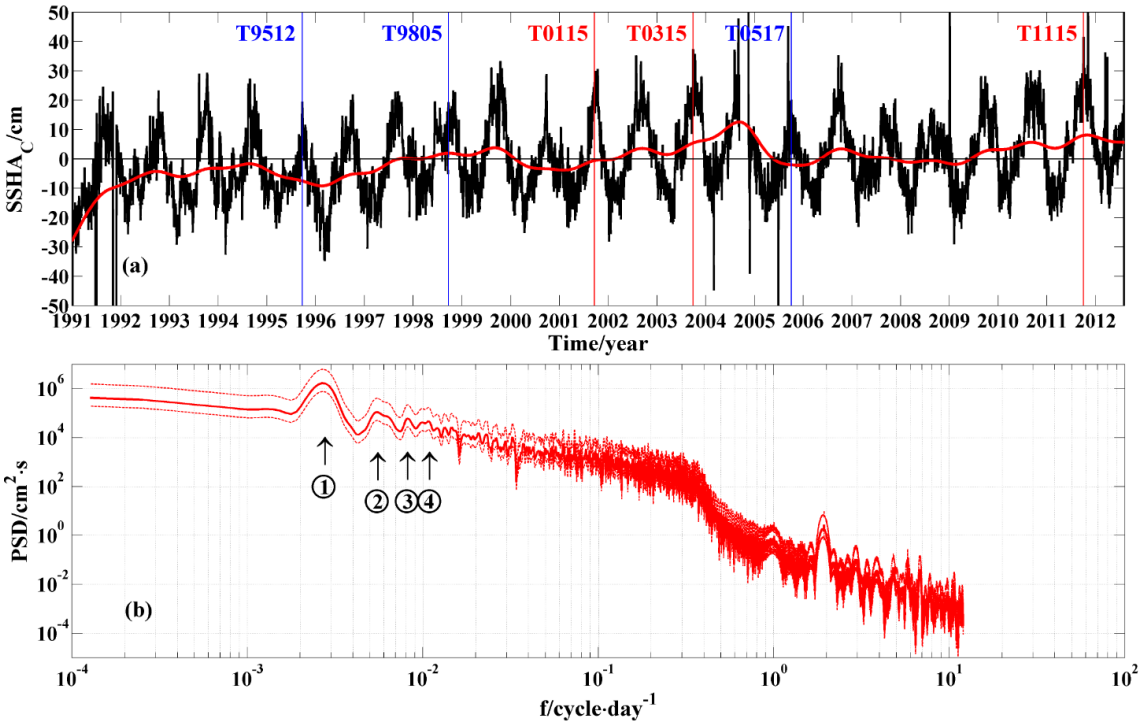

Fig. 3.3.1 *Time plots of the hourly mean non-tidal sea level data with the pressure correction (black line) accompanied by the inter-annual component (red line) (a), and the power spectral density diagrams with 95% confidence intervals for the non-tidal SSHAC data (b). The vertical lines in Fig. 3..3.1a with the typhoon names indicate the occurrence of ASLR events (six events during the past 21 years).The significant spectral peaks are pointed out by the vertical up-arrows with numbers ①, ②, ③ and ④ in Fig. 3..3.1b.*

The power spectral density diagrams for the non-tidal data are shown in Fig .3.3.1b with a 95% confidence interval (dashed lines). There are spectral peaks in the seasonal range (①) and the intra-seasonal ranges of half year (②), 4 months (③), and 3 months (④). The major tidal components (semidiurnal, diurnal and fortnightly) are well deleted by the tide-killer filter.

The time plot of the 2 year low-pass filtered (inter-annual) sea-level data (SSHAC) is shown in Fig .3.3.2a with the regression lines, showing a long-term trend. The power spectral densities are calculated from the inter-annual component after the removal of the long-term trend and shown in Fig .3.3.2b. The long-term trend shows an annual increment of 4.9 mm/year for the data extending from 1991 to 2011 (red sloping line). This annual increment is reduced to 1.0 mm/year for the 2001-2011 data (black sloping line). There is a spectral peak around 4.9 and 2.5 year as indicated with a black and red vertical arrow, respectively. The spectral peak (blue vertical arrow) for the seasonal range is still present because of its robustness.

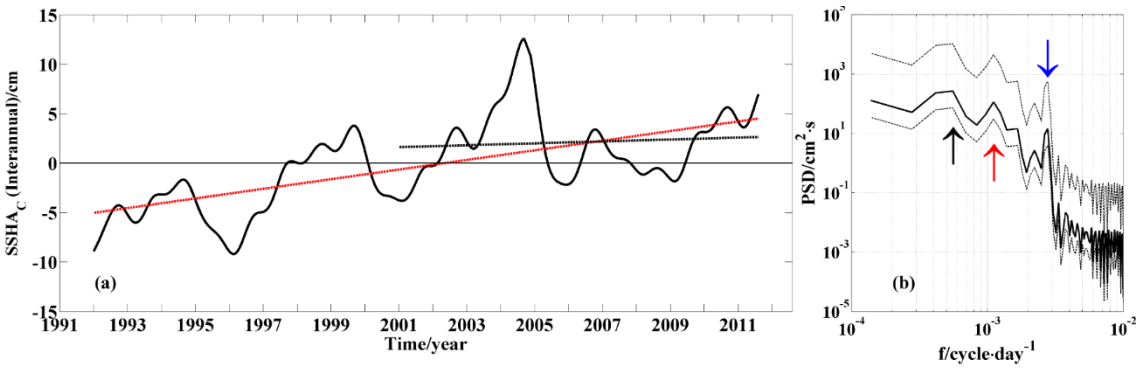

Fig. 3.3.2 *Time plots of the inter-annual component with the regression lines (a) and the power spectral density diagrams with a 95% confidence interval for the inter-annual component after the removal of long-term trend (b). The vertical arrows point out prominent spectral peaks.*

As shown in Figs. 3.3.3 and 3.3.4, the seasonal component (8 months to 2 years range) oscillates with a STD of 9.8 cm larger than the intra-seasonal component (1 month to 8 months range) with a STD of 4.7 cm. In Fig .3.3.4 the 106-d duration data are magnified around the corresponding ASLR event. The seasonal component always forms

a significant peak in September and the intra-seasonal component forms a peak especially near the ASLR events of 2001 and 2011.

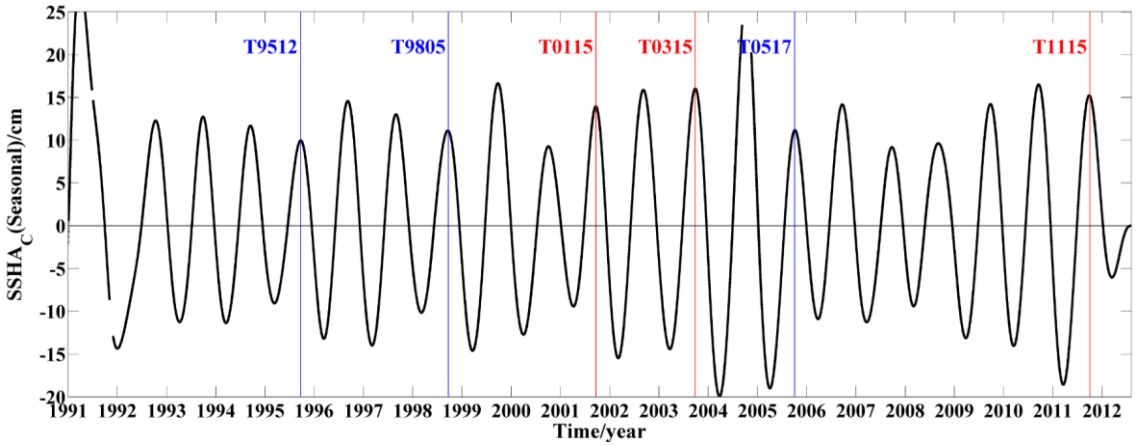

Fig. 3.3.3 *Time plots of the sea level variations for the seasonal component. The vertical lines with the typhoon names indicate the occurrence of ASLR events.*

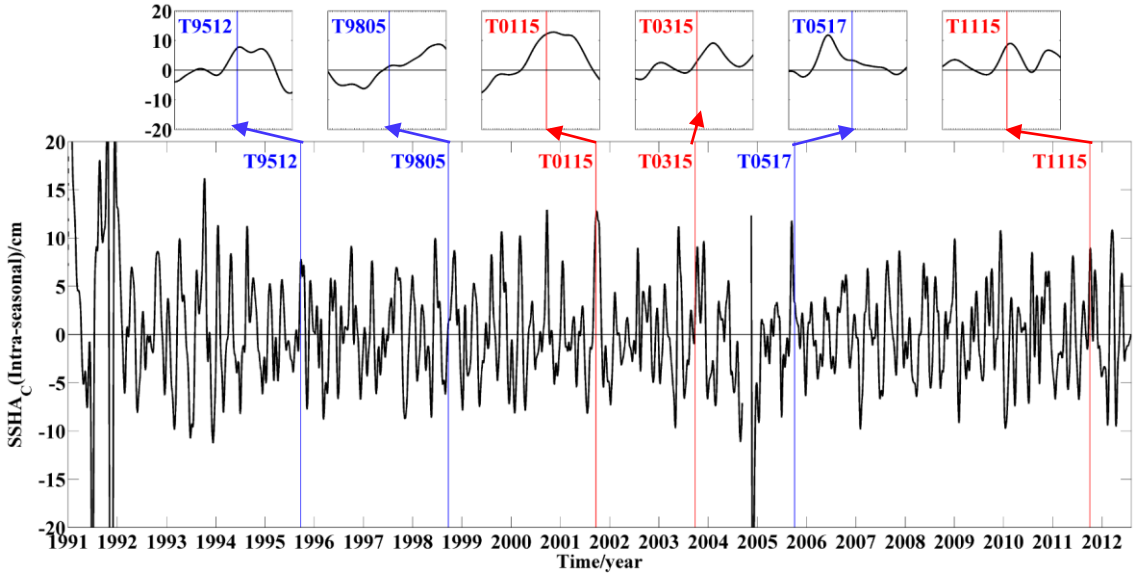

Fig. 3.3.4 *Time plots of the sea level variations for the intra-seasonal component. The vertical lines with the typhoon names indicate the occurrence of ASLR events. The 106 d duration data of intra-seasonal component, closed up around the corresponding ASLR*

events, are shown on the upper side of the figure.

The sea level rise from the 21-year mean sea level data is determined at the occurrence of each ASLR event as seen in Table 3.3.1**.** The total sea level rise is the summation of four components: inter-annual with a long-term trend (> 2 years), seasonal (8 months to 2 years), intraseasonal (1 month to 8 months), and sub-tidal (2 d to 1 month). The sub-tidal component is determined by subtracting the other three components from the total sea level rise. The total sea level rise at the ASLR events increases continuously and reaches 26.3 cm in the 2001 event and is further increased toward 36.9 cm in the 2011 event. There are three noticeable components with a significant effect for the ASLR events. The first is the seasonal component which exceeds 10 cm for all the events occurring in September. The second is the intra-seasonal component which reaches 12.2 cm for the 2001 event and 8.4 cm for the 2011 event. The third is the sub-tidal component determined as a remnant from other three components in the total sea level rise. It varies in a range of 2.3 to 15.5 cm.

Table 3.3.1 *Contribution of individual components to the six ASLR events*

	STD	1995	1998	2001	2003	2005	2011
Total sea level rise/cm (> 2 d)	12.5	22.7	21.1	26.3	36.6	18.6	36.9
Long-term trend/cm	—	-3.2	-1.8	-0.3	0.7	1.7	4.6
Inter-annual/cm (> 2 years)	3.4	-4.3	3.7	-0.2	4.7	-3.7	3.4
Seasonal/cm	9.8	10.0	11.1	14.0	16.0	11.2	15.2

(8 months-2 years)							
Intraseasonal/cm (1-8 month)	4.7	7.5	1.3	12.2	3.0	3.3	8.4
Sub-tidal/cm (2 d-1 month)	4.2	11.6	7.0	2.3	15.5	10.5	12.2

The sea level changes for the total, inter-annual, seasonal, intra-seasonal, and sub-tidal components are quantified in the standard deviations (STDs) from the 21-year mean data (Table 3.3.1). The inter-annual, seasonal, intra-seasonal and sub-tidal components make a STD contribution of 3.4, 9.8, 4.7, and 4.2 cm to a total value of 12.5 cm, respectively.

We shall here consider the time series data $X(t)$, constructed as the summation of the subcomponent of M pieces.

$$X(t) = x_1(t) + x_2(t) + \cdots + x_M(t) \tag{3.1}$$

Taking the temporal mean of the data, we get

$$\begin{aligned} X_m &= \frac{1}{N}\sum_{i=1}^{N} X_i = \frac{1}{N}\sum_{i=1}^{N}\{x_{1i} + x_{2i} + \cdots + x_{Mi}\} \\ &= x_{1m} + x_{2m} + \cdots + x_{Mm} \end{aligned} \tag{3.2}$$

where N is the number of data. The STD (d_s) of X may be expressed by

$$d_s(X) = \sqrt{\frac{\sum_{i=1}^{N}(X_i - X_m)^2}{N}}$$

The substitution of Eqs. (3.1) and (3.2) reduces to:

$$d_s(X) = \sqrt{\frac{\sum_{i=1}^{N}\left[w_{1i} + w_{2i} + \cdots + w_{Mi}\right]^2}{N}}$$

where $w_{1i} = x_{1i} - x_{1m}$; $w_{2i} = x_{2i} - x_{2m}$; and $w_{Mi} = x_{Mi} - x_{Mm}$. Considering $\sum_{i=1}^{N} x_{pi}x_{qm} = 0$ and $\sum_{i=1}^{N} x_{pi}x_{qi} = 0$ for $p \neq q$ (orthogonal condition), the above equation gives:

$$d_s(X) = \sqrt{\frac{\sum_{i=1}^{N} w_{1i}{}^2 + \sum_{i=1}^{N} w_{2i}{}^2 + \cdots + \sum_{i=1}^{N} w_{Mi}{}^2}{N}} = \sqrt{d_{s,1}{}^2 + d_{s,2}{}^2 + \cdots + d_{s,\mathrm{M}}{}^2} \qquad (3.3)$$

For the case of four components as examined in this paper, we get:

$$d_{s,\mathrm{total}}{}^2 = d_{s,\mathrm{inter}}{}^2 + d_{s,\mathrm{seas}}{}^2 + d_{s,\mathrm{intra}}{}^2 + d_{s,\mathrm{subt}}{}^2 \qquad (3.4)$$

where $d_{s,\mathrm{total}}$ is the total STD; $d_{s,\mathrm{inter}}$ is the inter-annual STD; $d_{s,\mathrm{seas}}$ is the seasonal STD; $d_{s,\mathrm{intra}}$ is the intra-seasonal STD; and $d_{s,\mathrm{subt}}$ is the sub-tidal STD.

3.3.2 Sub-tidal sea level variations

The significant sub-tidal sea level changes in the range of 2 d to 1 month occurred in several days after the typhoon passages in 1995, 1998, 2001, 2003, 2005, and 2011. These typhoons are named T9512 (the 12th typhoon of 1995), T9805, T0115, T0315, T0517, and T1115) by the JMA terminology. All the typhoon trajectories are shown in Fig .3.1.1, using the JMA data. The core position of each typhoon at the time when the maximum typhoon-derived northerly wind blew over Hiroshima Bay is also shown with

a circle accompanied by the typhoon number and core pressure. In particular, the red lines indicate the trajectory of the three typhoons (T0115, T0315, and T1115) which triggered the ASLR events on September 17, 2001; September 25, 2003; and September 28, 2011 in phases matched with the spring tide and were broadcasted on the TV and newspapers because the sea level was over the floor level of the Itsukushima Shrine, one of the world heritage sites designed about 30 cm above the high sea level of the spring tide in autumn.

The sea level data, processed through the (2 d to 1 month) band-pass filter, are shown in Fig. 3.3.5 together with the composite maps of the monthly STD variation, determined by assessing the same month data over whole years. The sea level data for 16 days are magnified around the corresponding ASLR event and shown on the upper side of the figure. Large sea level variations over 10 cm appear sporadically in the upper figure. The ASLR peak for T0315 and T1115 is especially prominent. The sea level variations occur in a STD range of 4.2 cm (Table 3.3.1), forming the biggest STD peak in September together with smaller STD peaks visible in June and November.

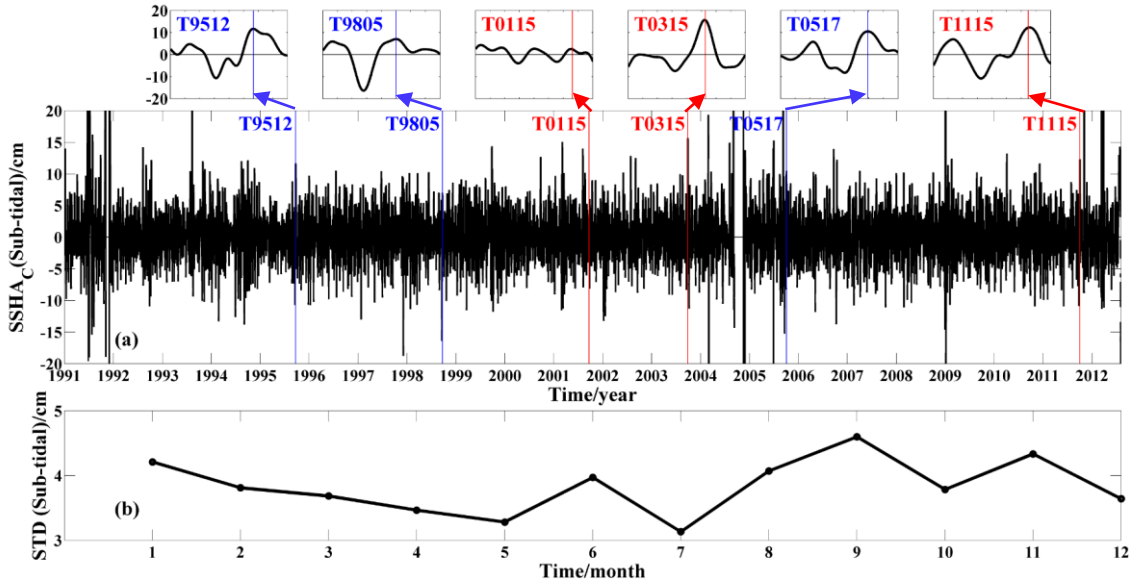

Fig. 3.3.5 *Time plots of sea level variations for the sub-tidal component. The vertical lines*

with the typhoon names indicate the occurrence of the ASLR events. The 16 d sea level data, closed up around the corresponding ASLR events, are shown on the upper side of the figure. The composite map of the averaged STD calculated by gathering the same monthly data over 21 years is shown in Fig .3.3.5b.

The sub-tidal sea level variation for 16 d around the ASLR events is shown in a magnified scale together with the sub-tidal wind and 2-d interval sea level data in Figs 3.3.6a-f. The vertical lines and thick vertical up-arrows indicate the occurrence of the maximum northerly wind and the ASLR events, respectively. The elapsed time (d) from the maximum wind is taken as the scale on the horizontal axis. For all the six cases, the sea level is remarkably depressed during the strong northerly wind, forming an upwelling. The sea level is slowly raised with weakened wind, and it reaches its maximum value 4 to 8 d later (ASLR event). The total sea levels' heights are over 30 cm (the Itsukushima Shrine floor level) for T0315 and T1115. The 2 m depth temperature data, obtained at the point TE, are added in Figs 3.3.6d-f in comparison with the sea level data. The peak-to-peak difference in temperature between the maximum wind and sea level varies in a range of 1.5 to 2.0 ℃ . In the developing phase of the northerly wind, the water temperature falls behind the sea level variation by about 1-d while this delay time is enlarged to about 2-d in the diminishing period of the wind, implying the weakened density stratification due to mixing.

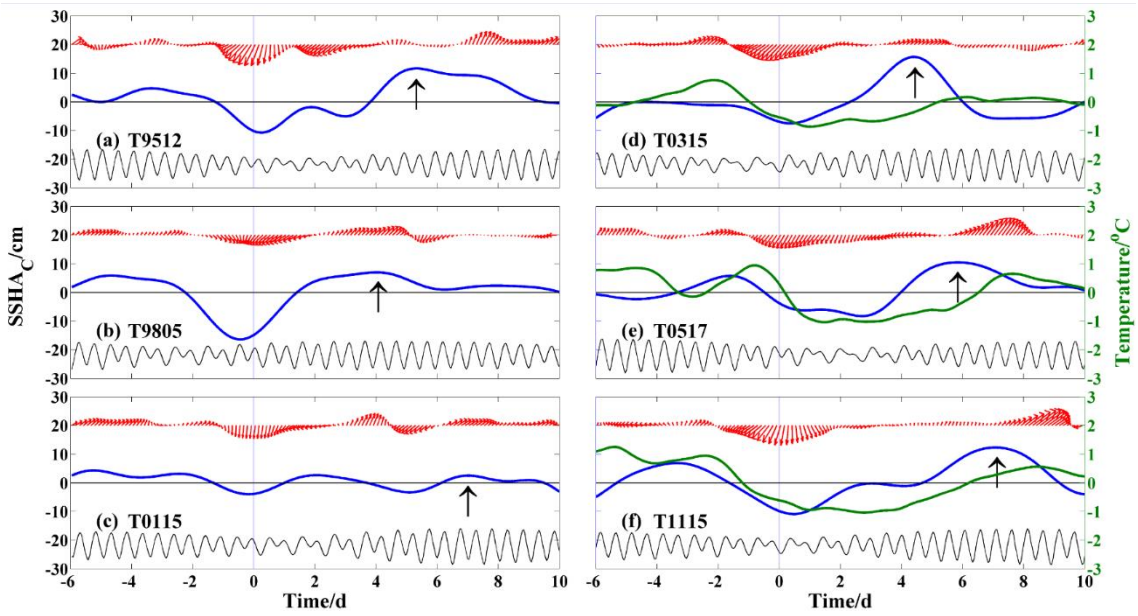

Fig. 3.3.6 *Sea level variations of the sub-tidal component for 16 d including the occurrence of all ASLR events (Figs 3.3.6a-f). The 2m depth water temperature variation is added in Figs 3.3.6d-f. The 4-h interval wind data smoothed through the (2 d to 1 month) filter are also shown at upper portion of the same figure. The vertical lines indicate the occurrence of the maximum northerly wind (corresponding to the start time of the events). The thick vertical up-arrows indicate the ASLR events.*

The dynamic mode analysis is here applied to understand the dynamics of sea level changes in the sub-tidal range, using the CTD data at Sta. C, obtained on October 3, 2011 by Hiroshima Prefectural Technology Research Institute (HPTRI). The vertical profiles of the temperature, the salinity, and the σ_t – density are shown in Fig .3.3.7a together with the amplitude function of vertical velocity for the first, second, and third internal modes (Fig.3.3.7b). Half a month after the maximum northerly wind (September 21) due to Typhoon T1115, the water temperature in Hiroshima Bay is almost homogenized while

the salinity stratification is still present. As a result, the σ_t − density is mostly determined not by temperature, but by salinity. The upper layer from the surface to 15 m contains colder and less saline water discharged from the Ota River. The observed time (d) of the ASLR events delayed from the maximum northerly wind is plotted against the estimated propagation time of the first internal mode in Fig .3.3.7c. The observed time of the ASLR event matches closely with the time estimated from the phase speed of the first internal mode. Six data points are scattered around a best-fit line with a slope of 1: the amplitude of ASLRs (half the peak-to-peak height) is plotted in Fig .3.3.7d against the wind speed averaged for a period with northerly winds over 7 m/s including their maximum values. The ASLR amplitude is roughly proportional to the wind speed, which dominates the offshore transfer of the upper layer water. The time difference of ASLR events from the nearest spring tide is plotted in Fig .3.3.7e against the delay time of ASLR events from the maximum northerly wind. The ASLR events for 1998, 2001, 2003, and 2011 phases are matched with the nearest spring tides.

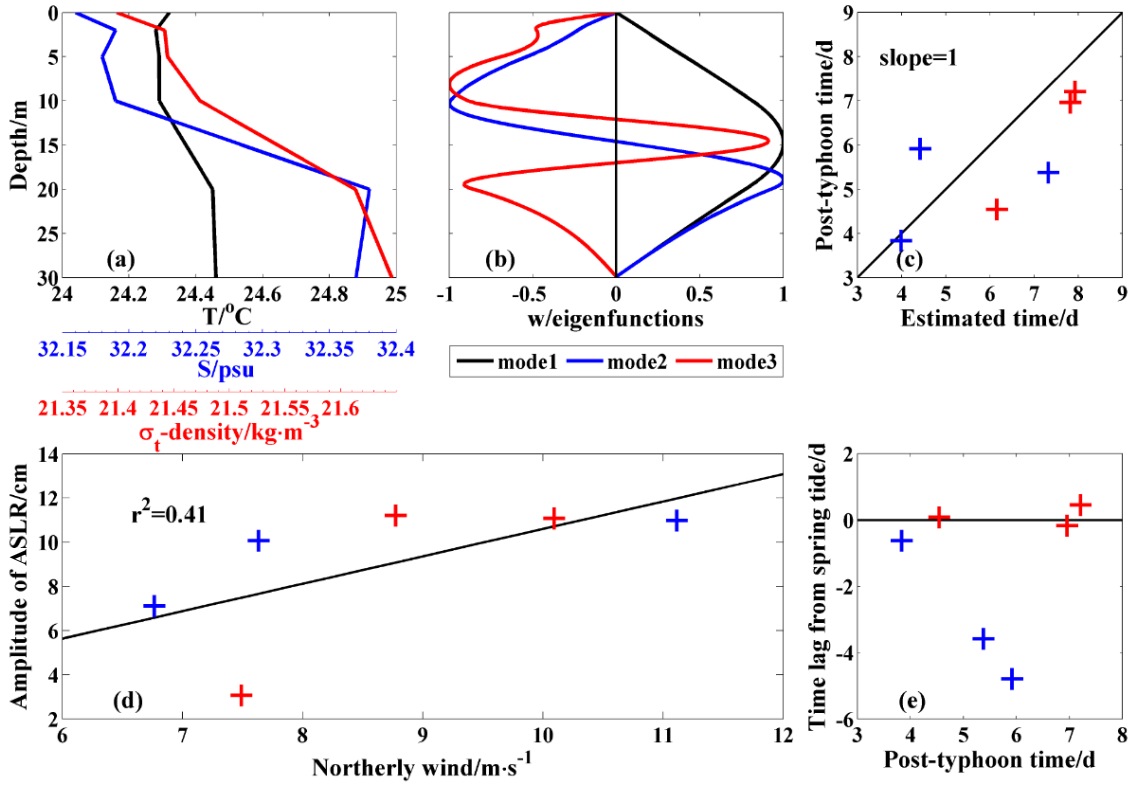

Fig. 3.3.7 *Vertical profiles of temperature, salinity, and σ_t – density (a) and the amplitude function of vertical velocity for the first, second, and third internal modes (b). The post-typhoon time plotted against the estimated propagation time for the first internal mode (c), the ASLR amplitude plotted against the northerly wind speed (d), and the time lag of the ASLR events from the nearest spring tide (e). The six crosses in Figs. 3.3.7c-e are data for the ASLR events during the last 21 years, and the red points indicate the 2001, 2003, and 2011 events in which the flood water was over the floor level of Itsukushima Shrine. The CTD data on October 3, 2011 are used for Figs. 3.3.7 a-b, and the CTD data at the nearest time of post-typhoon are used for Fig. 3.3.7c.*

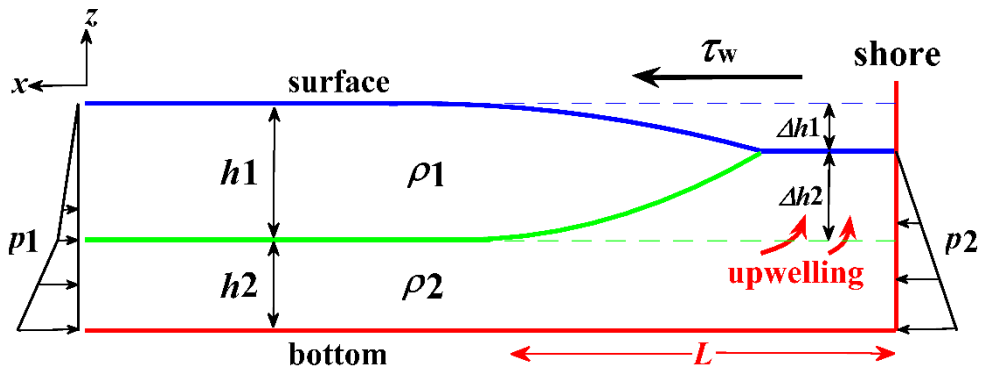

Fig. 3.3.8 *Sketch of upwelling and the associated sea surface depression, caused by the cross-shore wind blowing offshore. τ_w is the wind stress acting on the sea surface, and L is the width of the upwelled region. The points ($\rho 1$, h1) and ($\rho 2$, h2) are the density and the water depth for the upper and lower layers, respectively. $\Delta h1$ is the surface deviation, and $\Delta h2$ is the interfacial deviation. p1 and p2 are the horizontal pressures acting on the south and north boundaries of the observation domain.*

The upwelling and associated sea level changes, generated by the strong northerly wind crossing the north shore of Hiroshima Bay, are sketched in Fig .3.3.8. The wind

stress acting on the sea surface transfers the lighter (warmer) upper-layer water southward, forming an upwelling of the heavier (colder) lower-layer water. As the wind gathers speed, the upwelled water is accumulated along the northern coast, and the horizontal pressure acting on the south and north boundaries of the observation domain is balanced in the form:

$$\int_{-h1}^{0}(-\rho 1gz)dz+\int_{-(h1+h2)}^{-h1}(-\rho 2gz)dz=\int_{-(h1+h2)}^{-\Delta h1}(-\rho 2gz)dz+L\tau_W \qquad (3.5)$$

where z is the vertical coordinate taken upward. Notice that the wind stress term is removed from Eq. (3.5) because the offshore wind stress cannot make the sea surface slope in water, which continues offshore infinitely. This simplification is more easily manifested for the one-layer case. Thus Eq. (3.5) reduces to:

$$\Delta h1=h1\sqrt{\frac{\rho 2-\rho 1}{\rho 2}} \qquad (3.6)$$

where $\Delta h2$ is the interfacial deviation, which does not appear in Eq. (3.6). The anomalous sea level depressions ($\Delta h1$) for the six ASLR events, calculated from Eq. (3.6), are presented in Table 3.3.2 together with the wind and ASLR data. The data range from 5.6 cm for 2011 to 13.2 cm for 1998. The $\Delta h1$ values are distributed around the ASLR values. The weekly density data at depths 0, 2, 5, and 10 m are provided by Hiroshima City Agriculture, Forestry, and Fisheries Promotion Center (HCAFFPC). They are averaged values for five stations distributed over the northern Hiroshima Bay.

Table 3.3.2 *Parameter list related to upwelling and associated sea level changes*

Event No.	1995	1998	2001	2003	2005	2011
$W_m(m\cdot s^{-1})$	11.1	7.6	7.5	8.8	6.8	10.1

ASLR (m)	11.6	7.0	2.3	15.5	10.5	12.2
$\rho 1(kg \cdot m^{-3})$	1022.1	1021.1	1022.0	1021.4	1021.4	1021.4
$\rho 2(kg \cdot m^{-3})$	1022.4	1021.8	1022.1	1021.6	1021.7	1021.6
$h1\,(m)$	5	5	5	5	5	5
$\Delta h1\ (cm)$	8.0	13.2	6.8	7.6	9.3	5.6
$R_1\ (m)$	966.3	1773.7	892.9	1149.8	1602.4	905.2

Note that W_m denotes wind speed, ASLR is abbreviated from anomalous sea level rise, and R_1 denotes the Rossby internal radius of deformation for the first internal mode.

After the half period of the first internal mode, this heavier water, exposed to the sea surface and influenced by the sea level depression, falls down suddenly and is replaced by the lighter water coming back from offshore. The width (L) of the shoreline upwelling zone may be determined by the Rossby internal radius (R_1) of deformation for the first internal mode:

$$R_1 = \frac{C_1}{f} \qquad (3.7)$$

where C_1 denotes the phase speed of the first internal mode, and f is the Coriolis parameter. The R_1 values for individual events are also presented in Table 3.3.2.

3.4 Summary and discussion

The non-tidal sea level variations in Hiroshima Bay are studied over various time scales: inter-annual (>2 years), seasonal (8 months to 2 years), intra-seasonal (1 month to 8 months), and sub-tidal (2 d to 1 month) variations; using the 21-year sea level data. Special attention is paid to the sub-tidal component, of which the major source is provided by the upwelling and associated anomalous sea level changes, generated along the northern coast of Hiroshima Bay (opened southward) by the northerly cross-shore wind. In September, a strong northerly wind is sporadically generated by the remote effect from the typhoon passages off the Kii Peninsula in the 400 km east of Hiroshima Bay, and the associated sea level changes reach about 10 cm or more. Another factor contributes to the significant sea level rises in September: the sea level rise caused by thermal expansion is the largest in the seasonally warmest water of September, when the sea level rises by over 10 cm.

The total sea level variation has a standard deviation of 12.5 cm. The inter-annual component of the sea level variation in Hiroshima Bay oscillates with a standard deviation of 3.4 cm, forming a long-term trend of 4.9 mm/year. The standard deviation is 9.8 cm for the seasonal component and 4.7 cm for the intra-seasonal component. The seasonal component is the result of thermal expansion of water, and its effect is the biggest in September when the water temperature is highest. The intra-seasonal component makes a significant contribution to the 2001 and 2011 ASLR events, with sea level rises of 12.2 and 8.4 cm, respectively. The importance of the intra-seasonal component in the 2001 event was already pointed out by Tokeshi and Yanagi, although its generation process was not understood well (2004). Further study is required to understand the intra-seasonal sea level changes at a deeper level.

The sub-tidal component plays a significant role in some ASLR events as understood with a standard deviation of 4.2 cm. Its role is strengthened especially in the 2003 and

2011 events with a contribution of 15.5 and 12.2 cm, respectively (Table 3.3.1). It is reported that internal mode activity (such as internal waves and tides) is strong in the northern part of Hiroshima Bay in summer and early autumn [Nguyen et al., 2009]. A significant part of the internal mode activity in the sub-tidal range may be attributed to internal seiches/surges, generated in the northern half of Hiroshima Bay, shaped with a half ellipse of 25 km north-south length.

The following scenario of the internal mode generation is here proposed. In September, the water in Hiroshima Bay is separated into two regions - the warm, less saline upper layer and the cold, saline lower layer - with the density stratification moderated during the cooling season. Under such density stratification, the typhoon-derived northerly wind transports the near-surface lighter water southward, forming the upwelling of cold, saline water and the associated anomalous sea level changes along the northern coast. The temperature decrease follows behind the sea level depression since it takes about 1-d for the process of upwelling. The sea level depression due to the upwelling of heavier water ranges by about 10 cm (Table 3.3.2). After the northerly wind terminates, the upwelling stops, and the heavier water falls down suddenly, triggering the internal seiches/surges. Then the upper layer water is replaced by the lighter water, which comes back from the offshore region with the phase speed of the internal seiches. This leads a gradual sea level rise equivalent to the sea level depression. It is likely that this anomalous sea level oscillation overwhelms that expected from the steady internal wave phenomena, and so the oscillation decays rapidly toward a steady state.

The interdependency of sea level and near-surface temperature variations during the ASLR event provides evidence of the internal mode generation, although it was not observed directly (Fig .3.3.6). The phase speed of the internal seiches is determined by the dynamic mode analysis, which uses the CTD data obtained in the nearest time after each ASLR event [Gill, 1982]. The post-event data may be more preferable than the pre-event data because the density stratification is largely broken by the typhoon-derived

strong wind. The phase speed of the first internal mode ranges from 7.3 to 14.5 cm/s. This provides a period of 8.0 to 15.9 d, considering the wavelength (λ=4L), L (=25 km) is half the north-south length of the bay. The timing of the ASLR events is well explained by half the period of internal seiches (Fig .3.3.7c). This also provides further evidence of the internal mode generation.

Six ASLR events occurred in September of the corresponding years (1995, 1998, 2001, 2003, 2005, and 2011) as post-typhoon events during the last 21 years, although the major contribution from the sub-tidal component is replaced by the intra-seasonal component in the 2001 event. When these ASLR events are synchronized with the spring tide, flood water rises over the floor level of the Itsukushima Shrine as in 2001, 2003, and 2011. The sea level rises in the sub-tidal range vary from 2.3 cm (minimum, as in the 2001 event) to 15.5 cm (maximum in 2003). The sub-tidal range contribution to the sea level rise for the 2011 event is as large as 12.2 cm.

Internal seiches/surges have never been measured in Hiroshima Bay, in spite of finding the strong internal mode activity [Nguyen et al., 2009]. The major reason for this is that long-term mooring observations are strictly prohibited due to heavy oyster aquaculture and fisheries' activity. Instead of mooring works, a coastal acoustic tomography experiment was initiated in October 2012 to measure the internal mode activity in the sub-tidal range [Park and Kaneko, 2000]. Direct evidence of internal mode activity in the sub-tidal range is expected from this experiment.

Internal seiches/surges have often been reported in lakes with a steep-sided shape, through wind processes analogous to the present post-typhoon event [Thorpe, 1971, 1972, 2005; Hunkins and Fliegel, 1973; Farmer, 1978]. In spite of a number of previous studies of lakes, little attention has been paid to water level changes caused by the internal seiches/surges [Hutter, 2012]. The water surface level changes associated with the internal seiches were measured in Lake Geneva, although its amplitude was only 0.1% of the

internal-seiche amplitude (20 m maximum) [Lemmin et al., 2005]. As for the ASLR events in Hiroshima Bay, the sea level changes are initiated as a anomalous process by the cross-shore wind, accompanied by the upwelling of heavier water. The resulting sea level changes reach about 10 cm (about 2% of the interface deviation 5 m) and are much larger than those above the steady internal seiches.

Finally, this paper concludes that the upwelling and associated anomalous sea level changes generated by the strong northerly wind can play a significant role in the sub-tidal sea level rise events in Hiroshima Bay. The sea level rises above the floor level of the shrine (30 cm above the high tide in September) when the sub-tidal component coincides with both the seasonal component (with the maximum in September) and the intra-seasonal component (with phases matching the sub-tidal component).

References

Farmer D M. (1978). Observations of long nonlinear internal waves in a lake. *J Phys Oceanogr*, **8**: 63–73.

Gill A E. (1982). Atmosphere-Ocean Dynamics. *New York: Academic Press*, 622.

Hanawa K, Mitsudera H. (1985). On the data processing of daily mean values of oceanographically data—Note on daily mean sea-level data. *Bull Coast Oceanogr (in Japanese)*, **23**: 79–87.

Hunkins K, Fliegel M. (1973). Internal undular surges in Seneca Lake: a natural occurrence of solitons. *J Geophys Res,* **78**: 539–548.

Hutter K. (2012). Nonliear Internal Waves in Lakes. *New York: Springer*, 277.

Lemmin U, Mortimer C H, Bäuerle E. (2005). Internal seiche dynamics in Lake Geneva. *Limnology and Oceanography,* **50(1)**: 207–216.

Nguyen H , Kaneko A, Lin J, et al. (2009). Acoustic measurement of multi sub-tidal internal modes generated in Hiroshima Bay, Japan. *IEEE J Oceanic Eng,* **34(2)**: 103-112.

Park J H, Kaneko A. (2000). Assimilation of coastal acoustic tomography data into a barotropic ocean mode. *Gophys Res Lett,* **27**: 3373-3376.

Thorpe S A. (1971). Asymmetry of the internal seiche in Loch Ness. *Nature*, **231**: 306-308.

Thorpe S A. (1972). The internal surge in Loch Ness. *Nature*, **237**: 96-98.

Thorpe S A. (2005). The Turbulent Ocean. Cambridge: *Cambridge Univ Press*, 439.

Tokeshi C, Yanagi T. (2004). High sea level caused flood damage at Hiroshima in September 2011. *Umi-No-Kenkyu (Ocean Reaserch) (in Japanese)*, **13(5)**: 475-491.

Chapter 4 Long-term measurement of the Seto Inland Sea throughflow in Aki-nada

4.1 Introduction

The Seto Inland Sea, the largest inland sea in Japan, faces the Pacific Ocean with the Kuroshio Current at the western and eastern inlets (the Bungo and Kii Channels, respectively) and is surrounded by three of the main Japanese islands (Honshu, Kyushu and Shikoku) as shown in Fig. 4.1.1. It is characterized with east-west and north-south lengths of about 450 and 50 km, respectively, and a mean depth of 38 m. All regions of the inland sea have a strong tidal current, which flows among the approximately one thousand islands [Yanagi et al., 1982], and heavy fishing activity. The latter has led to a prohibition of moorings, including oceanographic moorings, the most standard method for long-term measurement of current and temperature. Part of the Kuroshio Current flows into the Seto Inland Sea sporadically through the Bungo and Kii Channels and significantly affects the inland sea environment [Akiyama and Saitoh, 1993; Takeuchi et al, 1998]. However, the Kuroshio intrusion rate, defined as the net flow rate through the Bungo and Kii Channels, has never been observed owing to the fishing-related restrictions.

Water exchange in the Seto Inland Sea has mostly been studied on the basis of the turbulent dispersion and diffusion due to the interaction between strong tidal currents and islands. An estimated inland sea residence time of 1.4 years was first determined using a dispersion coefficient and an associated advection rate that can explain the annual mean salinity distributed over the inland sea [Hayami and Unoki, 1970]. The residence time was also estimated to be 1.25 years from the turbulent diffusion of a tracer injected in a laboratory model of the inland sea [Takeoka, 1984]. However, the adopted dispersion and

diffusion coefficients have never been validated by field observation. Recently, Komai et al. [Komai et al, 2008] estimated the rate of Kuroshio intrusion through the Bungo and Kii Channels by coupling a Seto Inland Sea model for the depth-averaged (barotropic) current with a Kuroshio model that covers the area north of the Kuroshio stream axis and south of Shikoku and satisfies the geostrophic balance. Open boundary conditions were imposed on the Kuroshio stream axis with onshore-offshore shifts using the sea level and density data provided by the Japan Coast Guard (JCG). The rate of Kuroshio intrusion (corresponding to the Seto Inland Sea throughflow), which is primarily caused by the sea level difference between the Bungo and Kii Channels, was estimated to be 6,944 m^3s^{-1} with an associated residence time of 4.0 years for Period-1 (1982-1988), -8,488 m^3s^{-1} and 3.3 years for Period- 2 (1989-1993), and -9,259 m^3s^{-1} and 3.0 years for Period-3 (1994-1999). These periods correspond to the meander, transient and straight phases of the Kuroshio stream path variation, respectively. The first and second phases and the third phase may correspond to the offshore non-large-meander path and the nearshore non-large-meander path, respectively, as proposed by Kawabe [Kawabe, 1995]. It is likely that some transport will be added by introducing the baroclinic component in the inland sea model. Note that the positive and negative intrusion rates mean the intrusion at the Bungo and Kii Channels and correspond to the eastward and westward net transport in the inland sea, respectively. Until now, direct measurement of the net transport has never been attempted.

Coastal acoustic tomography (CAT) is an innovative technology well suited to measuring the environmental variations of coastal and inland seas with heavy fishing activity [Park and Kaneko, 2000; Yamaguchi, et al, 2005; Lin et al, 2005; Zhu et al, 2013]. It is a coastal-sea application of mesoscale ocean acoustic tomography, proposed in the 1970s as a key technology to map the 3D mesoscale structure of temperature and current [Munk and Wunsch, 1979; Munk et al, 1995]. The reciprocal sound transmission method, which has been applied to the measurement of current profiles in the deep sea [Worcester,

1977; Worcester et al, 1985; Howe et al, 1987; Taniguchi et al, 2010; Taniguchi et al, 2013], is also a proven method of cross-channel measurements of the current and temperature in straits and channels with crowded shipping traffic and fishing [Send et al, 2002; Adityawaman et al, 2011; Adityawaman et al, 2012]. Because of its positive path-averaging attributes and remote sensing capability (i.e., measuring from the periphery of the domain and avoiding fishing-related issues), CAT is a viable and robust method for observing the coastal sea.

In this chapter, CAT systems were operated over ten months to measure the variation of current and temperature in the Aki-nada Sea of the Seto Inland Sea. In Sects. 4.2-4.4, the acoustic data are described and the conversion of acoustic measurements to along-channel velocity and net throughflow is presented. Sect. 4.5 discuss error estimation for the acoustic model. Sect. 4.6 summarizes the transport and residence time estimates obtained by the acoustic method.

4.2 Site and Methods

A reciprocal sound transmission experiment using the CAT systems was carried out between two sound transmission and reception (acoustic transceiver) stations (T1 and T2) on both sides of the Aki-nada Sea in the western part of the Seto Inland Sea (see Fig. 4.2.1). T1 is at the edge of Kikuma breakwater and T2 is on the breakwater offshore of Osaki-Shimojima, as shown in Fig.4.2.2. Travel times were measured at each acoustic station, and the path-averaged (along-line) current and sound speed (temperature) were calculated from the differential travel time and mean (or one-way) travel time, respectively. The reciprocal sound transmission between the two acoustic stations is sketched in Fig. 4.3.1.

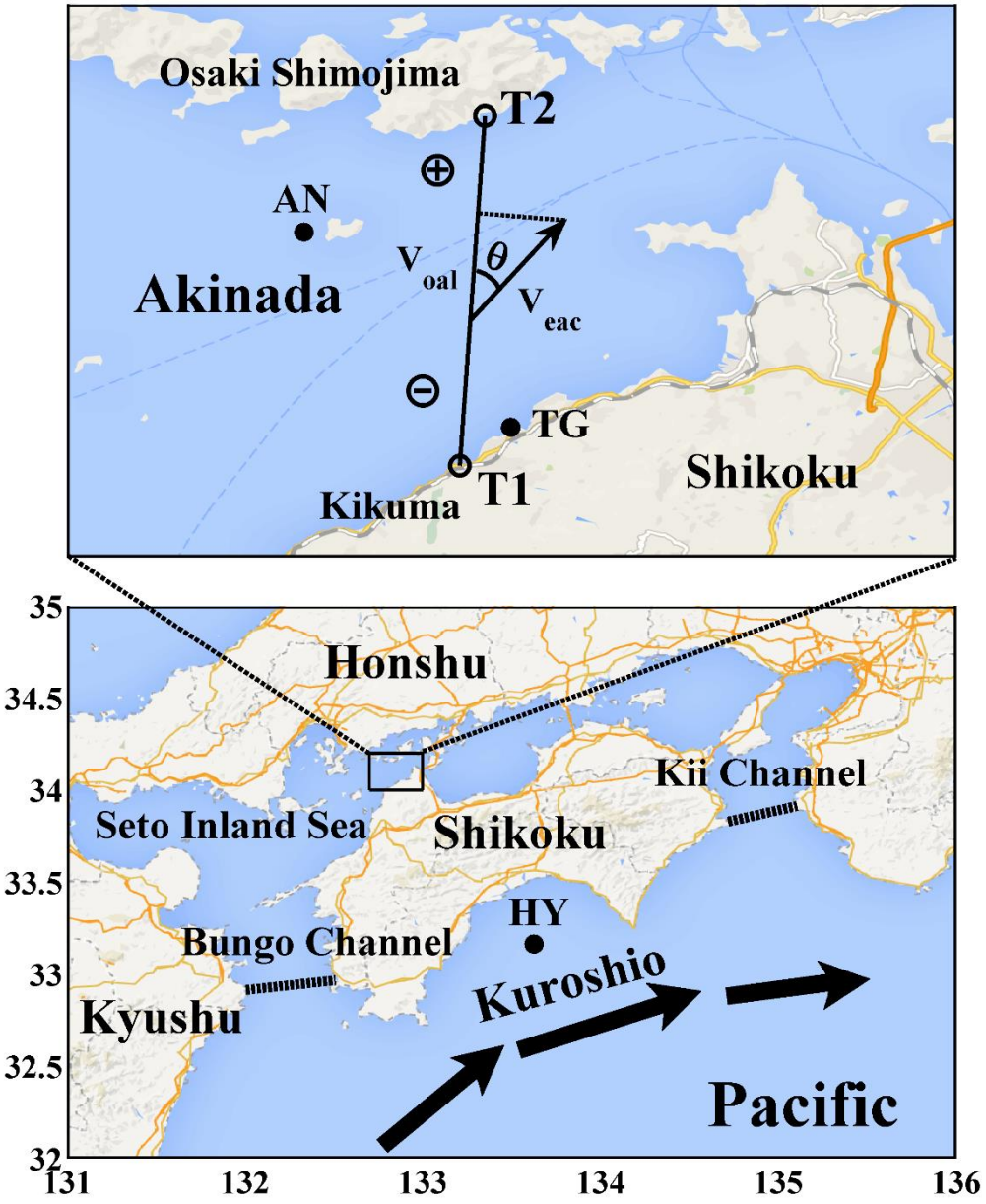

Fig.4.2.1 *Location map for the Seto Inland Sea and the adjacent regions. The experimental site in Aki-nada Sea is shown in a magnified scale in the upper of the figure. The sound transmission line is indicated with a solid line between T1 and T2. An along-line positive velocity is to the north.* V_{eac} *is the estimated along channel current, taken positive eastward. TG is the KIKUMA tide gauge station. HY is the data position for*

HYCOM. The border of the inland sea is indicated with broken lines at the inlet of the Bungo and Kii Channels.

The experiment started on 2 February 2012 and continued uninterrupted until 18 November 2012. During this period, the memory card was changed bimonthly. The performance of the preamplifier in the receiver circuit was improved on 12 April by replacing it with a back-up system so that the signal-to-noise ratio (SNR) was significantly increased. Because offsets between the subsurface acoustic transducer and the GPS antenna were not measured, the range between transducers was estimated using $L=Ct$, where C is the sound speed calculated from the conductivity-temperature-depth (CTD) data at Station AN, and t is the acoustically observed travel time. By using the 2-day mean data around the CTD acquisition time, a range of 13,769 m was determined with an accuracy of better than 1 m.

The seafloor depth gradually increased from 10 m at T1 to 45 m at 5 km, decreased to 25 m between 7 and 9 km, increased again to 60 m at 12 km, and rapidly decreased to 9 m at T2, as shown in the seafloor topographies in Fig. 4.3.2. The acoustic level of the received signals was considerably larger for T1 than for T2. This asymmetry of the acoustic amplitude may be caused by the non-reciprocity of the ray paths and the unequal setting of the system for receiving gain. More accurate knowledge on the asymmetry would require further study. As a result of the asymmetric effect, the T2-T1 data are relatively continuous and gap-free, while there are sometimes larger data gaps in the T1-T2 travel time data. For February-October 2012, the current and temperature were estimated using the reciprocal data with higher accuracy in spite of fewer data. For November 2012 using the one-way T2-T1 data, the temperature was estimated with an error that included the effect of currents.

The CAT systems, which have been developed by Hiroshima University since 1993 and frequently operated in various coastal seas, were placed on the offshore sides of the breakwaters that protect fishery ports. The acoustic transducer was suspended at a depth of 5 m in front of the breakwater and fixed to the seafloor with an anchored rope. The subsurface transducer was connected to the CAT system instrumentation in a plastic box via a cable, as shown in Fig. 4.2.2. The CAT system electronics used a 12 V rechargeable battery connected to a 12 V solar panel. Sound signals were transmitted with 24 V power using two rechargeable batteries with solar panels in a serial connection. A GPS antenna was stored inside the plastic box which was locked for security.

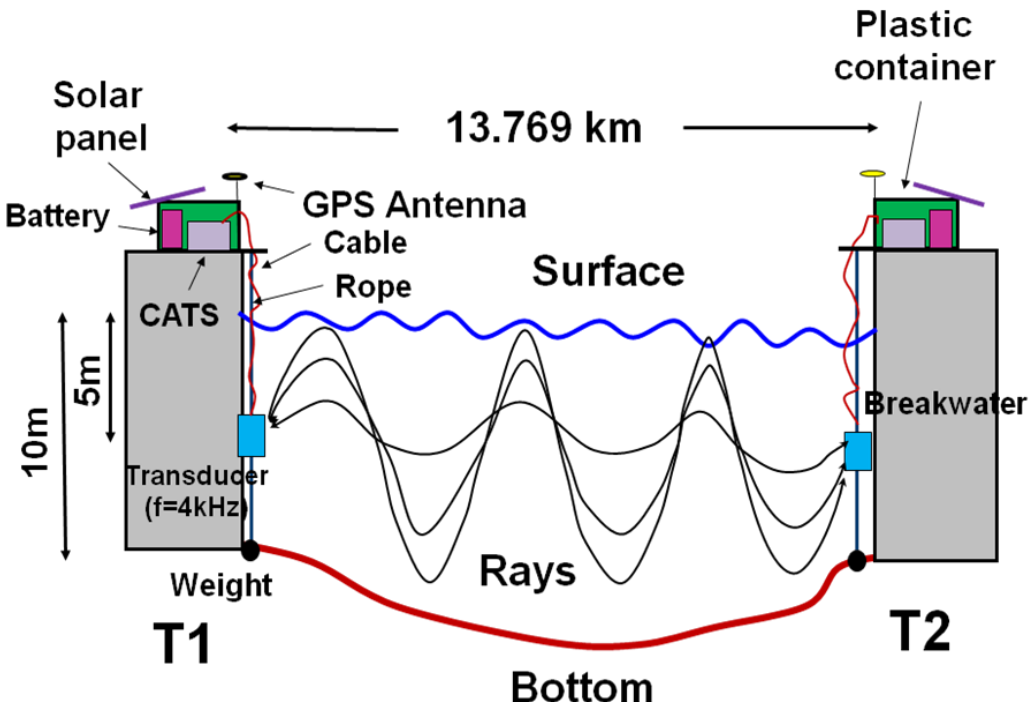

Fig. 4.2.2 *Sketch of the CAT systems set up at the edge of breakwater surrounding the fisheries port.*

Table 4.2.1 *Sound transmission signals and conditions*

transmission interval (min)	carrier frequency (kHz)	frequency bandwidth (kHz)	M sequence code	pulse length (s)	one digit length (ms)	Cycles/digit (Q-value)
10	4	1.3	12	3.071	0.75	3

The acoustic transducers and transmission parameters were the same as those used in a previous study [Adityawarman et al., 2011]. The transmission parameters are listed in Table 4.2.1. In the present study, the transmitted sound with 4 kHz carrier frequency was phase-modulated by a 12^{th} - order M sequence to increase the SNR of received signals by $10\log (2^{12} - 1) = 36$ dB. Three cycles per digit (Q-value) was selected as a suitable value to transmit the phase-modulated sound from the broadband transducer. The time resolution for multipath arrivals (t_r), defined as the one-digit length of the M sequence, was 0.75 ms. The signal was transmitted every 10 min with each station synchronized by GPS time. The received signals were cross-correlated with one period of the M sequence used in the transmission to obtain the arrival pattern with arrival peaks. The travel time associated with the largest arrival peak identified at a sampling frequency of 8 kHz is used here; only peaks with SNR>5 were taken into consideration in the subsequent analysis. The noise level is defined as the median value of the received data (most of the arrival pattern is noise; peaks only constitute a small fraction). Frequent data gaps occurred before the system was improved on 12 April. Furthermore, as indicated above, the SNR of the received signals was considerably smaller for T2 than for T1, with correspondingly fewer data and larger gaps. Many data gaps also appeared from August to early September because of strengthened thermal stratification in the neap tides with currents weaker than those in the spring tides. Thus, only the mid-April to late July and mid-September to October data were used for estimating the net transport from the

reciprocal (two-way) data. These data gaps did not significantly affect the path-averaged sound speed (temperature) estimate which has a much weaker requirement for travel-time measurement accuracy. The temperature was thus accurately estimated using two-way data for the months except November for which only one-way data were used.

Linear interpolation was adopted for regions with data gaps in the 10-min interval original data. The interpolated data were processed using a 1-hour low-pass filter (LPF) called a Butterworth filter to improve the accuracy of travel time measurement and to obtain the hourly mean data. The standard deviation of the high-frequency component, calculated by subtracting the hourly data from the original data, provides a measure of the travel time error t_e. The processed data were further smoothed using a 2-day LPF to remove tidal components and to obtain the 2-day mean data. The fortnightly tidal current still survived in the 2-day mean data owing to the insufficient data length; thus, the monthly mean was further taken to obtain steady currents. A physical currents with absolute values of greater than 0.2 ms^{-1} in the 2-day mean data, which arose because of filter edge effects on both sides of the gaps, were removed in the following analysis. Note that the 2-day mean currents were less than 0.2 ms^{-1}, especially during periods of transport estimation, as shown in the middle illustration of Fig.4.4.2 presented later. The errors for the 10-min interval and hourly mean data are decreased by taking the ensemble average of sequential data and are quantified by $t_e/\sqrt{6}$ for the hourly mean (six ensembles of the 10-min interval data) and $t_e/\sqrt{288}$ for the 2-day mean (288 ensembles of the 10-min interval data). In Sect. 4.5, we discuss the error estimation in detail.

Additional data were obtained for analysis. Observed hourly sea level data were provided by the nearest tide gauge station KIKUMA (Station TG). Monthly CTD data at Station AN were provided by the Hiroshima Prefecture Technology Research Institute (HPTRI). The CTD profile data, converted to sound speed, were used in the ray simulations between T1 and T2 to better understand how acoustic energy propagates in

the sea between the two transceivers. The CTD data were also used in the conversion from sound speed to temperature using the sound speed formula [Mackenzie, 1981]. The 20 m temperature data at Station HY in the Pacific Ocean south of Shikoku were obtained from the HYCOM model output, provided by the Naval Research Laboratory [Chassignet et al, 2009]. The model output served as the typical temperature in the Kuroshio south of Shikoku.

4.3 Processing the acoustic data to obtain along-channel flow

4.3.1 Forward schemes

We consider the reciprocal sound transmission in the vertical section between T1 and T2. The travel times t_1 and t_2 assigned for the transmissions from T1 to T2 and from T2 to T1, respectively, may be expressed by

$$t_1 = \frac{L}{C_{oal} + V_{oal}}, \qquad (4.1) \qquad\qquad t_2 = \frac{L}{C_{oal} - V_{oal}}, \qquad (4.2)$$

where V_{oal} and C_{oal} are the current and sound speeds, respectively, averaged in the vertical section from the upper to lower turning points of the traveling ray (see Fig. 4.3.1). The current V_{oal}, directed from T1 to T2, is taken to be positive. Solving the above two coupled equations, we obtain

$$V_{oal} = \frac{L}{2}\left(\frac{1}{t_1} - \frac{1}{t_2}\right) \approx \frac{C_0^{\,2}}{2L}\Delta t, \qquad (4.3) \qquad C_{oal} = \frac{L}{2}\left(\frac{1}{t_1} + \frac{1}{t_2}\right) \approx \frac{L}{t_m}, \qquad (4.4)$$

where $\Delta t = t_2 - t_1$, $t_1 \approx t_2 \approx t_m$ and $t_m = (t_1 + t_2)/2$. C_0 is the reference sound speed and is nearly equal to C_{oal}. V_{oal} and C_{oal} can be calculated from the travel time data by using the

second term of Eqs. (4.3) and (4.4), respectively. The third term of Eqs. (4.3) and (4.4) is used in the error evaluation in Sect. 4.5. In this study, the section-averaged temperature is calculated using the sound speed formula from the observed sound speed using the monthly varying depth-averaged salinity (32.08-33.17), determined from the station AN data, and half the depth (10 m) in the vertical section that the ray propagates. The estimated annual mean temperature changes at a rate of about 0.01 ℃m^{-1} as the depth changes.

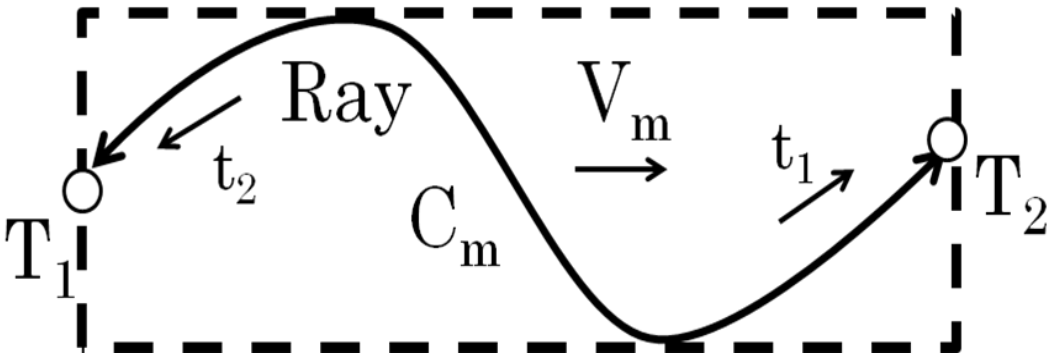

Fig. 4.3.1 *Sketch of the acoustic ray travelling reciprocally between T1 and T2 and the relevant parameters*

4.3.2 Ray simulation and transmission data

Ray simulations were performed by range-dependent bathymetry using a range-independent sound speed profile based on the CTD data at Station AN provided monthly. The results for February, May, August and October are shown as typical cases for the four seasons in Figs. 4.3.2(a)-(d), respectively. Except for Fig. 4.3.2(c) corresponding to August with bottom reflections, rays form refracted-surface-reflected patterns. The ray for the largest peak in the arrival pattern is coloured red and rays with travel times close

to that of the red ray are also shown. Except for in August, the deviation of the travel times from the red ray is smaller than the time resolution (0.75 ms) for multi-path arrival, and so individual arrival rays may be unresolvable and form a broad peak. Thus, the rays that form the broad peak span most of the vertical section except for the near-bottom layer. The arc length and travel time for the red ray are combined to estimate the reference sound speed C_0, and all three values are presented together in Table 4.3.2. The along-line (path-averaged) current and temperature were calculated for the red ray in each diagram. At this site, the tidal current reached $\pm$ 1.5 ms^{-1} in the spring tide and water was well homogenized except in summer and early autumn, with weak thermal stratification of about 1 ℃ from the surface to the bottom. In the case of homogenized water, sound propagates primarily as refracted-surface-reflected rays in the upper 15-25 m of the water column (Figs. 4.3.2(a), 4.3.2(b) and 4.3.2(d)). On the other hand, in the case of strong stratification, sound propagates primarily as refracted-bottom-reflected rays in the water column deeper than 10 m (Fig. 4.3.2(c)).

Stack diagrams of the observed arrival patterns corresponding to the ray simulations for May 2012 are shown with the transmission time increasing upward in Figs. 4.3.3(a) and 4.3.3(b) for the data obtained at T1 and T2, respectively, between 0000 and 0700 on 22 May 2012 (JST). The largest peaks are indicated by red circles. The values of t_1 and t_2 were obtained from these peaks. The corresponding Δt was then used with Eq. (4.3) to obtain the observed along-line current V_{oal} along the acoustic path.

(a) February

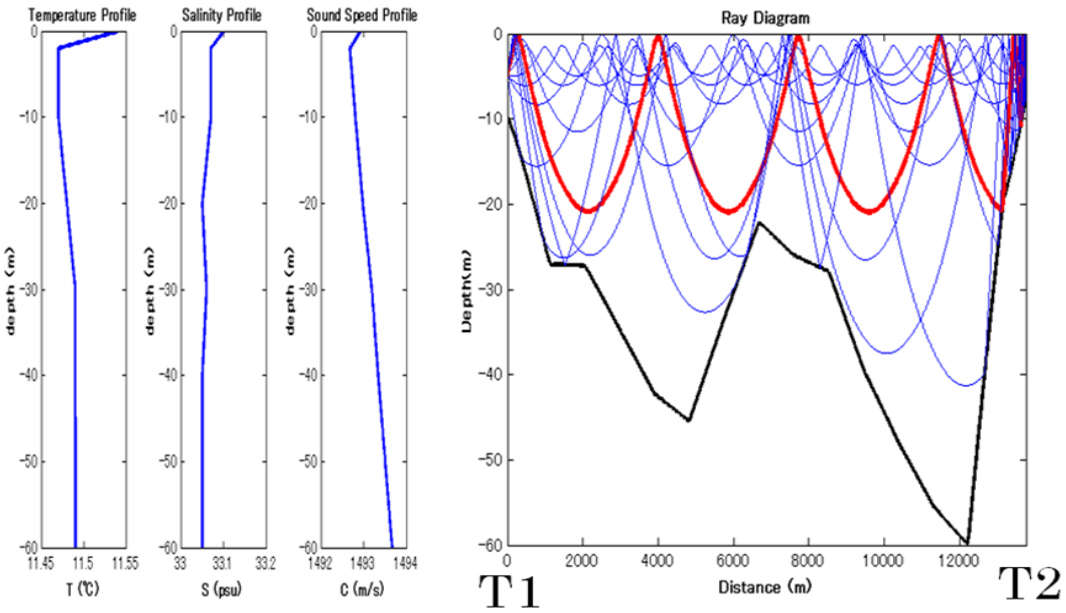

(b) May

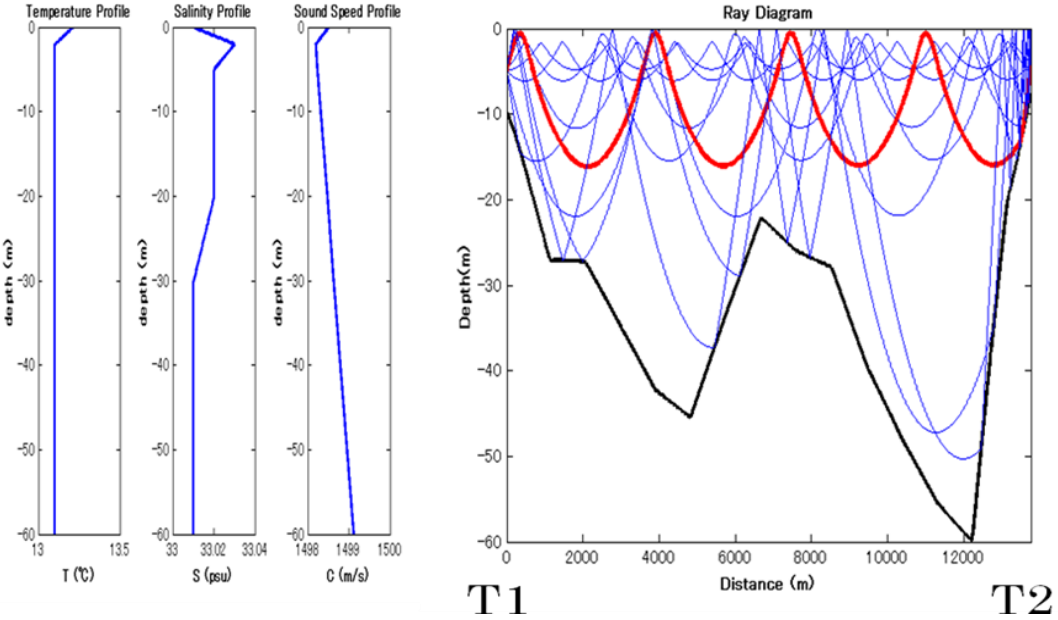

(c) August

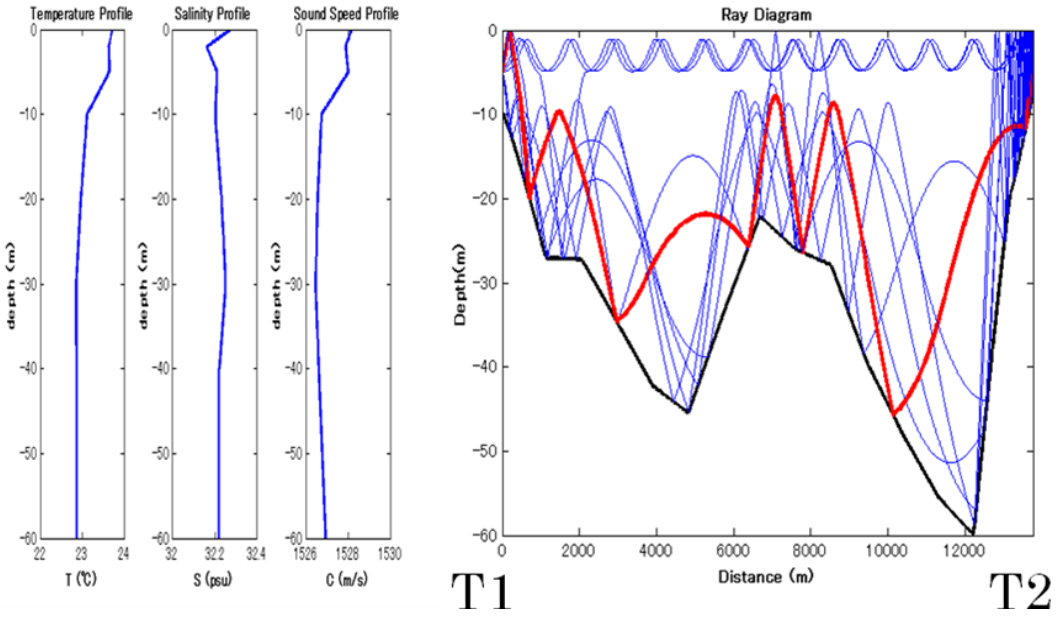

(d) October

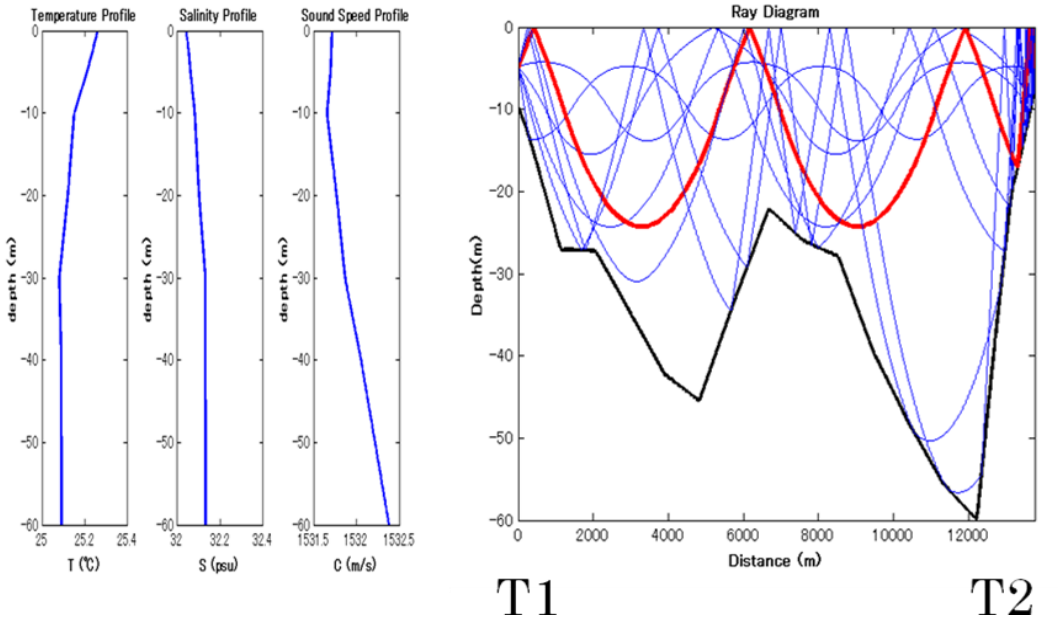

Fig. 4.3.2 *Results of the range-independent ray simulation, performed by using the monthly CTD data at AN. The ray corresponding to the largest arrival peak is coloured with red. The vertical profiles of T, S and C are shown at left of the figure: (a) February (b) May (c) August (d) October.*

(a) T1

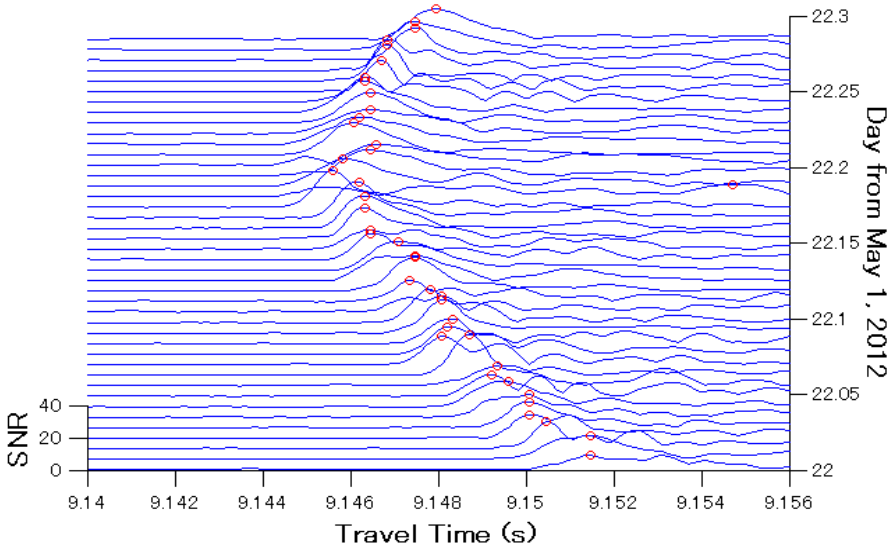

(b) T2

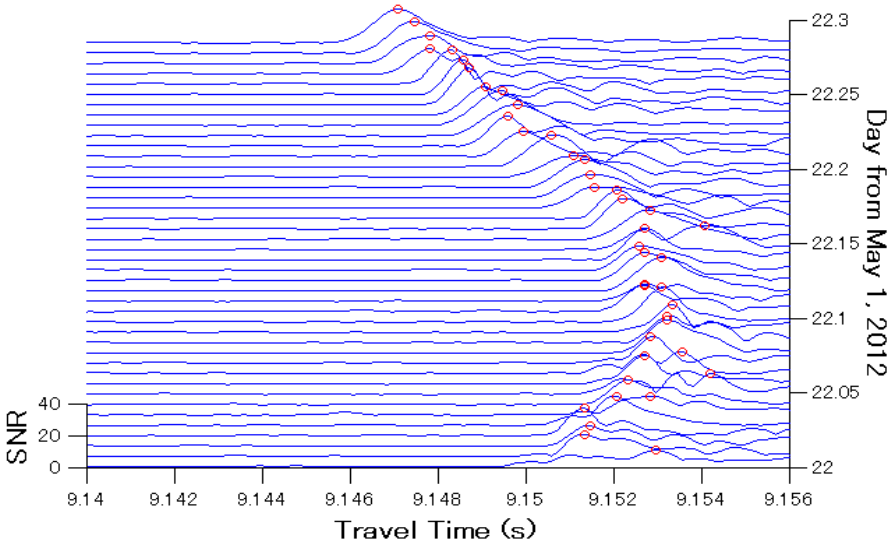

Fig. 4.3.3 *Typical examples of the stack diagram, obtained at (a) T1 and (b) T2 during 00:00-07:00 22nd May 2012 (JST). The correlation arrival patterns are stacked upward with proceeding time. Travel times corresponding to the largest peaks are indicated with red circles.*

4.3.3 Estimate of the along-channel transport

The estimation of the along-channel current V_{eac} from the observed along-line current V_{oal} and tide gauge data is described here. A harmonic analysis of the four major tidal constituents (M2 and S2 for the semi-diurnal constituents and K1 and O1 for the diurnal constituents) was applied to the observed hourly mean along-line current V_{oal} from 1 May to 30 June with the best reciprocal data set to determine the harmonic along-line current V_{hal} [Unoki, 1993]. The predicted along-channel current V_{pac} was independently estimated using tide gauge data and the long-wave equation for progressive tidal waves. Finally, V_{hal} and V_{pac} are used to obtain the angle between the acoustic line and the channel direction.

According to the long-wave theory for progressive tidal waves, V_{pac} is related to η_p as follows [Unoki, 1993]:

$$V_{pac} = \eta_p(x,t)\sqrt{\frac{g}{H}} \qquad (4.5)$$

where η_p is the tidal sea level variation predicted at the nearest tide gauge station and measured upward from the mean sea level (as shown in the first illustration in Fig. 4.3.4), x is the horizontal coordinate measured from the zero-crossing point on the up-slope of the cosine function, t is the time coordinate measured from any selectable point, g is the

acceleration due to gravity (9.8 ms^{-2}) and H is the average water depth for a non-flat seafloor.

Here the predicted along-channel current V_{pac} is regarded as that along the "true" channel direction. The angle of the true current to the transmission line may be calculated by

$$\cos\theta = \frac{V_{hal}}{V_{pac}} \qquad (4.6)$$

where V_{hal} is the harmonic along-line current obtained from the four-constituent harmonic analysis of the observed along-line current (V_{oal}). The value of θ measured clockwise from the transmission line T1-T2, as shown in Fig.4.2.1, is determined considering the direction of V_{oal}. This angle to the true direction is then used in the conversion from V_{oal} to the estimated along-channel current (V_{eac}) over the duration of the experiment:

$$V_{eac} = \frac{V_{oal}}{\cos\theta} \qquad (4.7)$$

where $0 < \theta < \pi/2$ for $V_{oal} > 0$ and $\pi < \theta < 3\pi/2$ for $V_{oal} < 0$. Note that Eq. (4.7) is an extension of Eq. (4.6) because V_{oal} includes not only V_{hal} but also other weak currents such as the remaining tidal constituents and steady currents.

The May-June data for the along-channel conversion V_{eac} of the hourly mean observed along-line current V_{oal} and harmonic along-line current V_{hal} are shown in the second illustration of Fig. 4.3.4. The predicted and estimated along-channel currents (V_{pac}

and V_{eac}) during May 21-25 are compared for time lags of 0 h (third illustration) and 1.17 h (fourth illustration), respectively, using the least-squares fit with a correction angle of $\theta = 49.5^{\circ}$ and a time lag of 1.17 h, which shows that the sea level lags behind the current. It is worth noting that tidal waves at the present site are shifted slightly (1.17 h in phase) from progressive waves. The eastward propagating tidal waves, which enter the inland sea from the Bungo Channel and pass the observation site, meet with the westward propagating ones, which enter from the Kii Channel, at the Bisan-seto, about 100 km east of the observation site [Yanagi, 1989]. It is likely that the observed tidal currents are phase-modulated by the interference of both tidal waves.

The net transport through the Aki-nada Sea *Q* is then calculated with the following formula:

$$Q = V_{eac}\, \mathrm{A} \sin\theta \qquad (4.8)$$

where *A* (=477,936 m^2) is the cross-sectional area of the vertical section from the surface to the seafloor along the sound transmission line T1-T2. V_{eac} is the average along-channel current for the entire vertical cross section, but it may be slightly overestimated because rays do not travel through the near-bottom layer with a weak current.

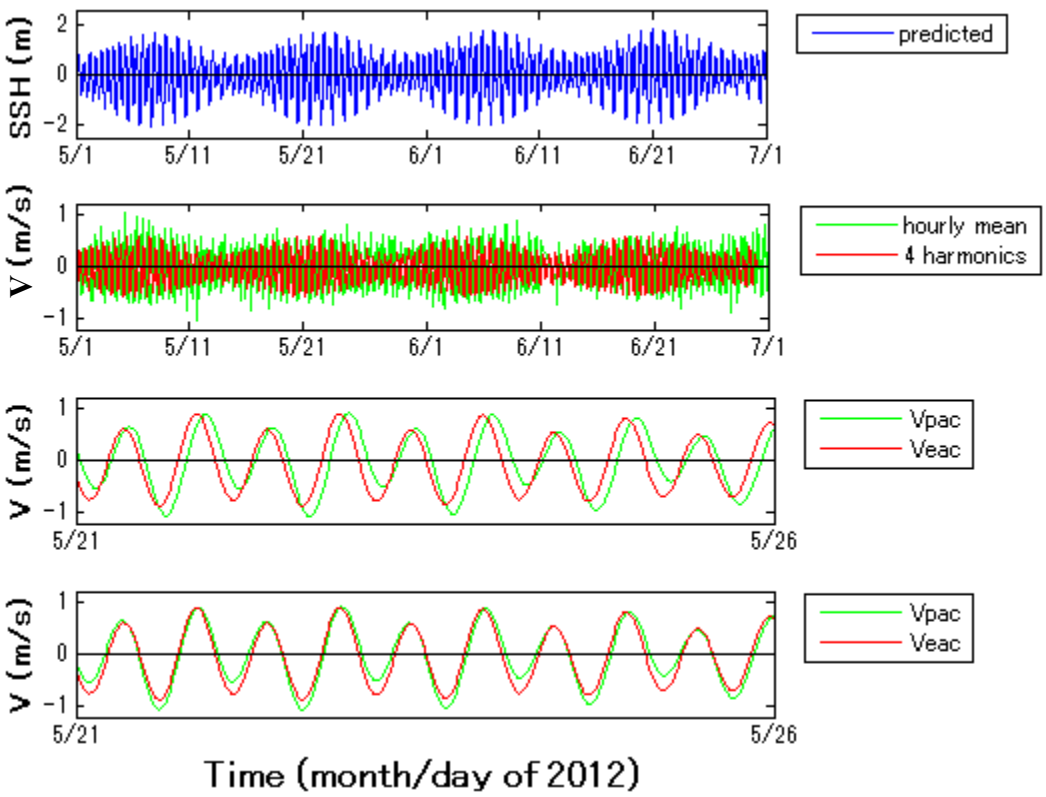

Fig. 4.3.4 *Time plots of (first illustration) the predicted sea surface height and (second illustration) the estimated along-channel current (green line) accompanied by the harmonic analysis result (red line) for the four major harmonic constituents (M2, S2, K1, O1). The estimated along-channel current (red line) is compared with the predicted one (green line) in the third and fourth illustrations. The predicted current is shifted forwards by 0 and 1.17 hours in the third and fourth illustrations, respectively.*

4.4 Temporal variation of along-channel current and temperature

The estimated along-channel current and path-averaged temperature for February and May are shown in Fig. 4.4.1 as representative cases of the worst and best data

acquisition, respectively. For the February data, the fortnightly cycles of tidal current are observable in spite of the many data gaps, and the temperature data indicate a reasonable pattern of seasonal cooling. The 2-day mean data with an absolute current greater than 0.2 ms^{-1}, which appear at the edges of data gaps as filter-edge effects, were removed. Because of the large number of data gaps, the February data were not used in the net transport estimate. The May data are characterized by the regular cycles of semidiurnal, diurnal and fortnightly tides. The magnitude of the hourly mean current reached 1.5 ms^{-1} in the spring tide and 0.5 ms^{-1} in the neap tide with no data gaps. The temperature indicated seasonal warming toward summer.

(a) February

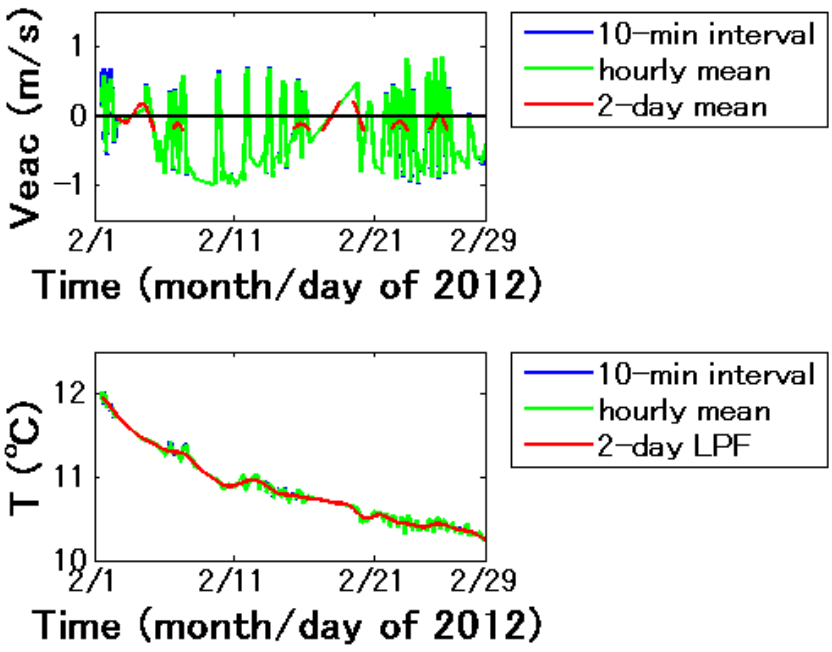

(b) May

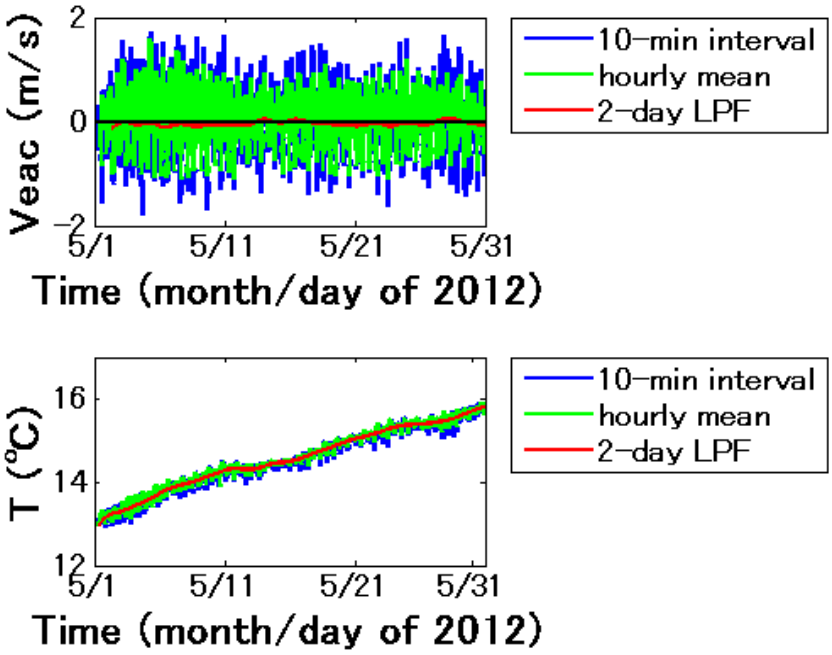

Fig. 4.4.1 *Time plots for the months (a) February and (b) May representing the worst and best data acquisition, respectively; the upper illustration for the estimated along channel current and lower one for the path-averaged temperature. The blue, green and red solid lines are for 10-min interval, hourly mean and 2-day mean data, respectively.*

The estimated along-channel current V_{eac} for February-October, determined using Eq. (4.7) with $\theta = 49.5^{\circ}$, is shown in the upper and middle illustrations of Fig. 4.4.2. The 2-day mean data of V_{eac} are enlarged in the middle illustration. The current data for February-early April had many gaps due to insufficient receiver gain. The gaps in the current data for August to early September were caused by strengthened thermal stratification resulting in rays exhibiting bottom bouncing and the associated decrease in

the signal level at the receiver (T2). The hourly mean estimated along-channel current showed a fortnightly tidal cycle, which ranged from 0.5 to 1.5 ms^{-1}. The 2-day mean current varied due to the surviving tidal components and sometimes saturated at a magnitude of 0.2 ms^{-1} during the periods of February to mid-April and August to early September. Except for these periods, the 2-day mean current was scattered in the range smaller than 0.2 ms^{-1}. A time plot of the temperature for the entire period from February to November (two-way data for February-October and one-way data for November) is also shown with thick blue circles in the lower illustration of the same figure together with the monthly temperature at Station AN. The one-way temperature for the entire period is also shown in the same figure with the blue broken line. For February-October, both the temperatures were nearly equal with a root- mean-squares difference of 0.149 ℃. The 20 m HYCOM temperature is also shown in the same figure, representing typical data in the Kuroshio south of Shikoku. The observed 2-day mean temperature had a minimum of 10.1 ℃ on 10 March and a maximum of 25.9 ℃ on 17 September. The observed 2-day mean temperature was in good agreement with the upper 20 m average temperature at Station AN. Assuming a periodic annual cycle, the temperature in the December－January gap was estimated by linear interpolation using the Station AN data. The annual mean temperature of 17.3 ℃ for the Aki-nada Sea was considerably lower than 22.3 ℃ for the Kuroshio region.

The 2-day mean net transport, calculated by substituting the 2-day mean estimated along-channel current and $\theta = 49.5^{\circ}$ into Eq. (4.8), is shown in Fig. 4.4.3 for mid-April to late July and early September to October. The 2-day mean net transport time series showed a significant scatter due to fortnightly tidal components surviving in the 2-day mean current, and the monthly mean was further taken to suppress the fortnightly components. The monthly mean transport ranged from Q_{oct}= -22,845 m^3s^{-1} (westward) in October to Q_{jul}=2,566 m^3s^{-1} (eastward) in July, implying possible seasonality (maximum

in summer and minimum in winter). The average of monthly mean transport Q_{mean} was -12,250 m^3s^{-1} (westward), forming the following day-weighted average:

$$Q_{mean} = \frac{20 \times Q_{Apr} + 31 \times Q_{May} + 27 \times Q_{Jun} + 20 \times Q_{Jul} + 18 \times Q_{Sep} + 27 \times Q_{Oct}}{143} = -13{,}107 \quad m^3 s^{-1}$$

The above monthly mean transports are nearly equal to the 6-month (143-day) mean transport of -11,651 m^3s^{-1}. Here we have assumed that the current estimated from the travel time data is the average for the entire vertical cross section.

The exchange time of Seto Inland Sea water with Pacific water ($T_{exchange}$) can be estimated by the following formula using the net transport Q and inland sea volume V:

$$T_{exchange} = \frac{V}{Q} \qquad (4.9)$$

$T_{exchange}$ is estimated to be 778 days (2.1 years) for Q=13,107 m^3s^{-1} and 876 days (2.4 years) for Q=11,651 m^3s^{-1} assuming V=8,815 x 10^8 m^3.

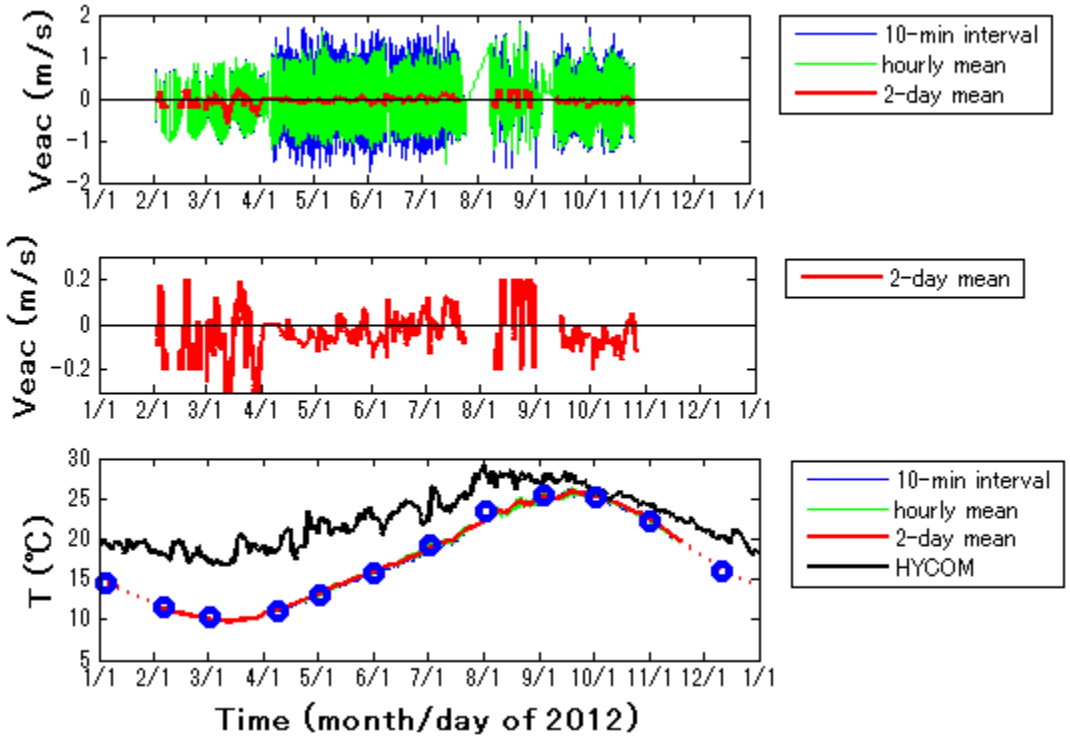

Fig. 4.4.2 *Time plots of the (upper, middle) estimated along-channel current and (lower) path averaged temperature for the 10-min interval data (blue), the hourly mean data (green) and 2-day mean data (red). The 2-day mean data of* V_{eac} *are magnified in the middle illustration. In the lower illustration, the monthly temperature data at AN are plotted with blue circles. The blue broken line shows the 2-day mean data from one-way data. The acoustic data are interpolated with red broken lines through December and January, using the AN data. The daily mean HYCOM data (at location HY in the Kuroshio, outside of the Seto Inland Sea) are also shown with the black line.*

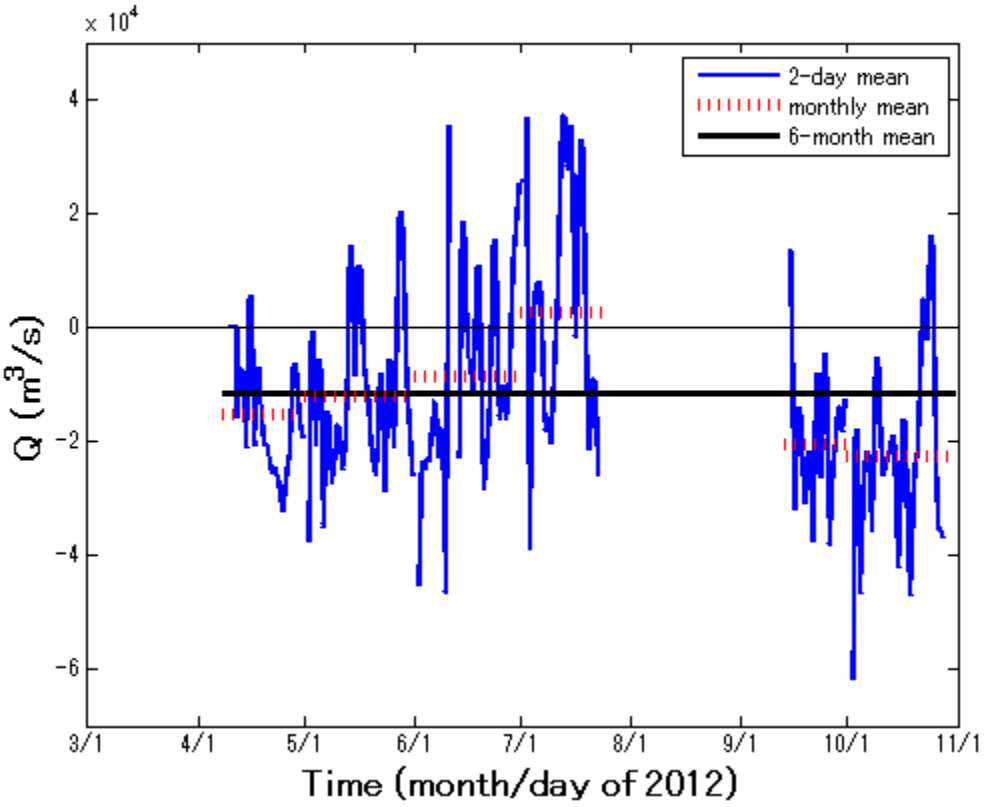

Fig. 4.4.3 *Time plots of the net channel throughflow for the 2-day mean data (blue solid line). The monthly averages of the net throughflow and their 6-month mean are indicated with the red broken line and black solid line, respectively.*

4.5 Error evaluation

Travel time errors in deep-sea acoustic tomography are mainly caused by high-frequency variation due to internal waves. This error source is first examined in coastal-sea tomography. The standard deviation of travel time differences for the period range of 10 min to 1 h was estimated to be t_{e1}=1.40 ms from the February-October observation

data; this is the high-frequency variance of the travel time difference signal. Note that this error is significantly greater than the one-digit length of the M sequence (t_r =0.75 ms), namely, the nominal time resolution for multipath arrival, and so t_{e1} rather than t_r is taken into consideration in the following error analysis. From Eq. (4.3), the travel time error t_{e1} is converted to the along-line velocity error V_e, which ranges from 0.113 to 0.119 ms^{-1} and takes an average of 0.116 ms^{-1}, as shown in Table 4.5.1. For the 1-h moving average, V_e is then $0.116/\sqrt{6}$ = 0.047 ms^{-1} (six ensembles of the 10-min-interval original data). For the 2-day moving average, V_e is reduced to $0.116/\sqrt{288} = 0.007$ ms^{-1} (288 ensembles of the original data).

The error for the 2-day mean net transport (Q_e) can be estimated by taking the total derivative of Eq. (4.8) with respect to V_{eac} and θ,

$$Q_e = \delta Q = A\left(\delta V_{eac} \sin\theta_0 + V_0 \delta\theta \cos\theta_0\right)$$

where V_0 is the average current for February-October and θ_0 is the rotation angle for the estimated along-channel current. By replacing δV_{eac} and $\delta\theta$ by the errors V_e and θ_e, respectively, the above equation is rewritten as

$$Q_e = A\left(V_e \sin\theta_0 + V_0 \theta_e \cos\theta_0\right) \qquad (4.10)$$

The second term on the right-hand side of Eq. (4.10) is assumed to be negligible because the angle is well determined $(\theta_e \approx 0)$ according to the fourth illustration of Fig. 4.3.4. For A=477,936 m^2, $V_e = 0.007$ ms^{-1} and θ_0 = 49.5°, we obtain $Q_e = \pm 2{,}544$ m^{3}s^{-1} for the estimated 2-day transport error.

Differentiating Eq. (4.4) with respect to t_m at a fixed *L*, we obtain the relationship between a small variation (δC_m) of C_m and a small variation (δt_m) of t_m as follows:

$$\delta C_m = \frac{C_0^{\,2}}{L}\delta t_m \qquad (4.11)$$

Note that the negative sign on the right-hand side of Eq. (4.11) is removed as we are dealing with implicitly positive rms errors. The travel time error for sound speed measurement is estimated from the standard deviation of high-frequency variations in the range of 10 min to 1 h. The error is 0.70 ms for the 2-way data during February-October (305 days) and 0.25 ms for the one-way data in November (19 days). The effective error t_{e2} is reduced to 0.67 ms by day-weighted averaging. Note that the travel time error for the one-way data during February-November is 0.69 ms, nearly equal to t_{e2}. The sound speed error C_e is obtained by replacing δt_m in Eq. (4.11) with t_{e2} and ranges from 0.108 ms^{-1} in February to 0.114 ms^{-1} in October with a mean of 0.111 ms^{-1} (see Table 4.5.1). It is reduced to 0.045 ms^{-1} for the hourly mean data (six ensembles) and 0.007 ms^{-1} for the 2-day mean data (288 ensembles).

Table 4.5.1 Characteristic parameters of the ray which forms the largest arrival peak

	Ray parameters and sound speed for the largest arrival peak				
	Ray length L (m)	Travel time (s)	Reference sound speed Co (m/s)	Error velocity Ve (m/s)	Error sound speed Ce (m/s)
Feb	13,771	9.2245	1,492.87	0.113	0.108

May	13769	9.1894	1498.36	0.114	0.109
Aug	13770	9.0200	1526.61	0.119	0.113
Oct	13769	8.9893	1531.71	0.119	0.114

The total derivative of MacKenzie's sound speed formula [MacKenzie formula] with respect to T_m and S_m under fixed salinity (S_0) and depth (D_0) shows that the sound speed variation δC_m is related to the temperature and salinity variations (δT_m and δS_m , respectively) as follows:

$$\delta C_m = \left.\frac{\partial C_m}{\partial T_m}\right|_{\substack{S=S_0 \\ D=D_0}} \delta T_m + \left.\frac{\partial C_m}{\partial S_m}\right|_{\substack{T=T_0 \\ D=D_0}} \delta S_m \qquad (4.12)$$

For the yearly mean temperature and salinity (T_0=17.3 ℃ and S_0=32.7), the fixed depth D_0=10 m and yearly salinity variation range $\delta S_m = \pm 0.5$, as determined from the Aki-nada Sea data, Eq. (4.12) reduces to

$$\delta C_m = 2.993 \delta T_m \pm 0.582 \qquad (4.13)$$

By replacing δC_m with the sound speed error $C_e = \pm 0.007$ ms^{-1} in Eq. (4.13), the temperature error $T_e = \delta T_m$ is composed of two parts:

$$T_e(C) = 0.334 C_e = \pm 0.002$$

$$T_e(S) = \pm 0.194 \qquad (4.14)$$

The composite error for the two sources of temperature error is estimated to be

$$T_e(total) = \sqrt{T_e(C)^2 + T_e(S)^2} = 0.20 \ ^\circ C \qquad (4.15)$$

when all errors are orthogonal.

4.6 Summary

The long-term variations of current and temperature in 2012 were measured using reciprocal sound transmissions along the transect T1-T2 in the Aki-nada Sea of the Seto Inland Sea, Japan. The error of path-averaged current measurement is $\pm$ 0.047 ms^{-1} for the hourly mean data and $\pm$ 0.007 ms^{-1} for the 2-day mean data. The error of sound speed measurement is $\pm$ 0.007 ms^{-1} for the 2-day mean data. The corresponding temperature error is $\pm$ 0.20 ℃.

The observed along-line current was converted to the estimated along-channel current with an angle correction of 49.5 ° from the sound transmission line and a phase correction of 1.17 h from the progressive wave using the nearest tide gauge station data and the long-wave equation. This phase shift from the progressive wave requires further study. Except for August and early September, for which there were many data gaps due to thermal stratification, the estimated along-channel current showed fortnightly tidal variation with an amplitude range of 0.5 to 1.5 ms^{-1}. The monthly mean transport ranged from -22,845 m^3s^{-1} (westward) in October to 2,566 m^3s^{-1} (eastward) in July, implying possible seasonality (maximum in summer and minimum in winter). The net westward transport averaged monthly for the accurately observed period of six months was 13,107±2,544 m^3s^{-1}. The path-averaged temperature was calculated using the sound speed formula from the sound speed data under monthly fixed salinity ranging from 32.08 to 33.17 and a fixed depth of 10 m. The 2-day mean temperature showed a seasonal minimum of 10.1 ℃ on 10 March and a seasonal maximum of 25.9 ℃ on 17 September.

The estimated exchange time of inland sea water is 778 days (2.1 years) for the observed net transport, shorter than the exchange times of 3.0 and 3.3 years estimated for the westward net flow on the basis of the barotropic model developed by Komai et al. [Komai et al, 2008]. This is the first direct-observation data of net transport through the Seto Inland Sea. Further study is required to clarify the dependence of the Kuroshio stream path variation on the net transport.

Reciprocal sound transmissions across seas (at an oblique angle to the flow) can be a robust measure of the along-channel transport as well as the cross-channel temperature.

References

Adityawarman, Y., A. Kaneko, K. Nakano, N. Taniguchi, K. Komai, X. Guo, and N.Gohda , (2011). Reciprocal sound transmission measurement of mean current and temperature variations in the central part (Aki-nada) of the Seto Inland Sea, Japan, *J. Oceanogr*. **67**, 173-182, doi 10.1007/s 10872-011-0016-5.

Adityawarman, Y., A. Kaneko, N. Taniguch, H. Mutsuda, K. Komai, X. Guo, N. Gohda, (2012). Tidal current measurement in the Kurushima Strait by the reciprocal sound transmission method, *Acoustical Science and Engineering*, **33**, 45-51.

Akiyama, H. and S. Saitoh, (1993). The Kyucho in Sukumo Bay induced by Kuroshio warm filament intrusion, *J. Oceanogr.*, **49**, 667-682.

Chassignet, E.P., H.E. Hurlburt, E.J. Metzger, O.M. Smedstad, J.A. Cummings, G.R. Halliwell, R. Bleck, R. Baraille, A.J. Wallcraft, C. Lozano, H.L. Tolman, A. Srinivasan, S. Hankin, P. Cornillon, R. Weisberg, A. Barth, R. He, F. Werner, and J. Wilkin, (2009). US GODAE: Global ocean prediction with the HYbrid Coordinate Ocean Model (HYCOM), *Oceanography,* **22**, 64–75.

Hayami, S. and S. Unoki, (1970). Water exchange and material dispersion in the Seto Inland Sea, *Proc. 17th Conference on Coastal Engineering, Japan Society of Civil Engineers*, 385-393.

Howe, B. M., P. F. Worcester, and R. C. Spindel, (1987). Ocean acoustic tomography: Mesoscale velocity, *J. Geophys. Res.*, **92**, 3785-3805.

Kawabe, M, (1995). Variation of current path, velocity, and volume transport of the Kuroshio in relation with the large meander, *J. Phys. Oceanogr.*, **25**, 3103-3117.

Komai, K., T. Hibino and T. Ohkama, (2008). Influence of the Kuroshio meander/straight on flow in the Seto Inland Sea, *Proc. Japan Soc. Civil Engineers*, **64**, 165-179.

Lin, J., A. Kaneko, N. Gohda and K. Yamaguchi, (2005). Accurate imaging and prediction of Kanmon Strait tidal current structures by the coastal acoustic tomography data, *Geophys. Res. Lett.*, **32**, L14607, doi:10.1029/ 2005GL022914.

MacKenzie, K. V., (1981). Nine-term equation for sound speed in the ocean, *J. Acoust. Soc. Am.*, **70**, 807-812.

Munk, W. and C. Wunsch, (1979). Ocean acoustic tomography: a scheme for large scale monitoring. *Deep-Sea Research Part A. Oceanographic Research Paper*, **26**, 123-161, doi:http://dx.doi.org/10.1016/0198-0149(79)90073-6.

Munk, W., P. F. Worcestor, and C. Wunsch, (1995). *Ocean Acoustic Tomography*. Cambridge Univ. Press, Cambridge.

Park, J-H. and A. Kaneko, (2000). Assimilation of coastal acoustic tomography data into a barotropic ocean model, *Geophys. Res. Lett.*, **27**, 3373-3376.3.

Send, U., Worcester, P., Cornuelle, B., Tiemann, C. and Baschek, B., (2002). Integral measurement of mass transport and heat content in the Strait of Gibraltar from acoustic transmissions. *Deep-Sea Res., Part Ⅱ*, **49**, 4069-4095, doi:10.1016/S0967-0645(02)00143-1.

Takeoka, (1984). Exchange and transport time scales in the Seto Inland Sea, *Continental Shelf Res.*, **3**, 327-341.

Takeuchi, J., N. Honda, Y. Morikawa, T. Koike and Y. Nagata, (1998). Bifurcation current along the southwest coast of the Kii Peninsula. *J. Oceanogr.*, **53**, 45-52.

Taniguchi, N., A. Kaneko, Y. Yuan, N. Gohda, H. Chen, G. Liao, C. Yang, M. Minamidate, Y. Adityawarman, X. Zhu, and J. Lin, (2010). Long-term acoustic tomography measurement of ocean currents at the northern part of the Luzon Strait, *Geophys. Res. Lett.*, **37**, L07601, doi:10.1029/2009GL042327.

Taniguchi, N., C-F. Huang, A. Kaneko, B. M. Howe, Y-H. Wang, Y. Yang, J. Lin, X-H. Zhu and N. Gohda, (2013). Measuring the Kuroshio Current with ocean acoustic tomography, *J. Acoust. Soc. Am.*, **134**, Pt.2.

Unoki, S, (1993), Coastal Physical Oceanography, Tokai University Press, Tokyo.

Worcester, P. F., (1977). Reciprocal acoustic transmission in a midocean environment. *J. Acoust. Soc. Am.*, **62**, 895–905.

Worcester, P. F., R. C. Spindel, and B. M. Howe, (1985). Reciprocal acoustic transmissions: Instrumentation for mesoscale monitoring of ocean currents, *IEEE J. Oceanic Eng.*, **OE-10**, 123-137.

Yamaguchi, K., J. Lin, A. Kaneko, T. Yamamoto, N. Gohda, H-Q. Nguyen and H. Zheng, (2005). A continuous mapping of tidal current structures in the Kanmon Strait. *J. Oceanogr.*, **61**, 283-294.

Yanagi, T, (1989), Coastal Oceanography, Koseisha-Koseikaku, Tokyo.

Yanagi, T., H. Takeoka and H. Tsukamoto, (1982). Tidal energy balance in the Seto Inland Sea, *J. Oceanogr. Soc. Jpn.*, **38**, 293-299.

Zhu, X-H., A. Kaneko, Q. Wu, C. Zhang, N. Taniguchi, and N. Gohda, (2013). Mapping tidal current structures in Zhitouyang Bay, China, using coastal acoustic tomography. *IEEE J. Oceanic Eng.*, **38**, 285-296, doi: 10.1109/JOE.2012.2223911.

Chapter 5 Tomographic mapping of a coastal upwelling and the associated diurnal internal tides in Hiroshima Bay, Japan

5.1 Introduction

Hiroshima Bay is a bay of elliptical shape, located in the western part of the Seto Inland Sea, and is characterized by the biggest oyster aquaculture field in Japan. Conventional coastal upwelling occurs when alongshore winds parallel to a coast (not cross-shore) generate off-shore transport to the right of the wind in the northern hemisphere (due to the Coriolis effect), causing deep waters to rise the surface near the coast [Gill, 1982]. The situation may be different in semi-enclosed bays, where geostrophic balance may not apply; in such cases, cross-shore winds may cause upwelling. Coastal upwelling generated in semi-enclosed bays of the scale of 10 km, like the northern part of Hiroshima Bay, belongs to the latter group generated by cross-shore winds [Taylor and Stewart, 1959; Thomson, 1981; Hunt, 1995]. Internal seiches and surges may be caused by post upwelling processes [David and Schertzer, 1999; Appt et al., 2004; Hutter, 2012]. Rises in sea level associated with internal surges are of great concern in Hiroshima Bay because they can flood the corridor of Miyajima Shrine, a world heritage site [Zhang et al., 2014].

In this chapter, a CAT system was operated to obtain short-interval snap shots of the horizontal distribution of temperature in the northern part of Hiroshima Bay, Japan (Fig.5.2.1). Coastal upwelling and associated internal tides, generated by the northerly wind from a typhoon that passed along the eastern side of the bay, were the major observation targets.

5.2 Site and Methods

A CAT experiment was performed from 11-25 Sept. 2013 in the northern part of Hiroshima Bay, Japan. Four sound transmission and reception stations: H1, H2, H3 and H5 (hereafter referred to as acoustic stations), were set up. The distances between any two acoustic stations were estimated using the global position system (GPS). Distances ranged from 3.9 km to 8.9 km. Because offsets between the subsurface acoustic transducer and the GPS antenna were not measured, ranges between the transducers were corrected using the method presented in Sect. 2.3.

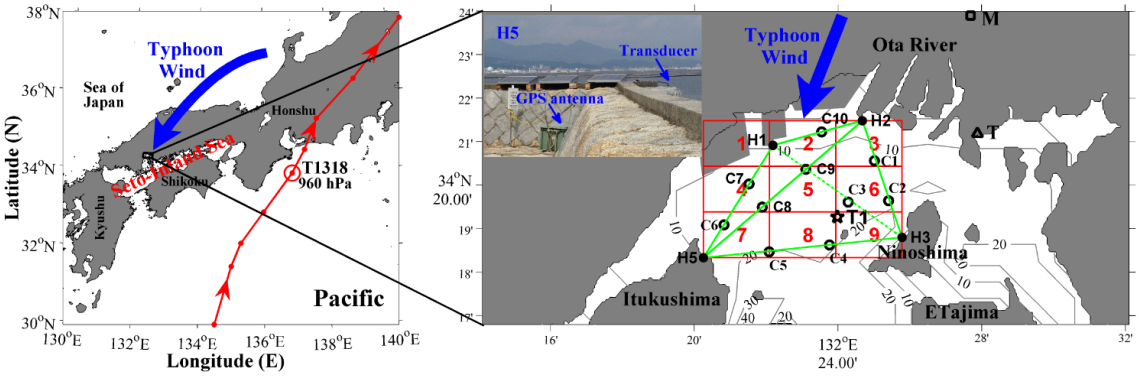

Fig. 5.2.1 *Map of the Seto Inland Sea and adjacent regions, showing the trajectory for the typhoon (T1318) on 16 Sept. The core position of T1318 for the largest northerly wind in Hiroshima Bay is shown by a red circle, accompanied by the typhoon number and air pressure. The northern part of Hiroshima Bay is magnified in the right panel, which shows the four CAT stations (H1, H2, H3 and H5) and ten CTD cast locations (C1-C10). The green solid and broken lines connecting the acoustic stations show the successful and unsuccessful sound transmission lines, respectively. T is the JCG's HIROSHIMA tide gauge station and M is the JMA's Hiroshima Branch. T1 is the position of the temperature array. The tomography domain is divided into nine rectangular sub-domains bounded by red meshes. The photo of the CAT system taken at station H5 is shown in upper left corner of the magnified figure.*

A 10 kHz signal, phase-modulated by one period ($(2^{11}$ -1) digits) of an 11^{th} order M sequence, was transmitted every 10 minutes from the broadband acoustic transducer (ITC-3013). Each digit of the M sequence included 3 cycles of the 10 kHz carrier, and the transmission therefore lasted 3 x 2047/10,000= 0.614 s. The experimental region has a relatively flat seafloor (10-20 m in depth). Temperature profiles from the surface to the seafloor were measured by the temperature array (positioned at T1, as shown in Fig. 5.2.1), at depths of 0, 2, 4, 7 and 10 m. Conductivity-temperature-depth (CTD) casts were done at ten stations (C1-C10) on the sound transmission lines using a small fishing boat. The CTD casts were performed from 1020-1150 on 18 Sept. (Japan standard time: JST), two days after a typhoon (T1318) passed closest to Hiroshima Bay (on 16 Sept.). The trajectory of T1318 was plotted in the same figure using Japan Meteorological Agency (JMA) data. The CTD data not only provided the vertical profile of sound speed in the tomography domain, but also validated the CAT observations. Weekly CTD data, averaged horizontally for five stations distributed in the northern part of Hiroshima Bay, were provided at reference depths of 0, 2, 5 and 10 m on 11, 17 and 24 Sept. by the Hiroshima City Fisheries Promotion Center (HCFPC).

Sea level data (with an interval of 5 min) at the tide gauge station “HIROSHIMA” (marked T in Fig. 5.2.1) were provided by the Japan Coast Guard (JCG). Atmospheric data (air pressure and wind velocity) with an interval of 10 min were provided by the Hiroshima Branch of the Japan Meteorological Agency (marked M in Fig. 5.2.1). These data were used to make the air pressure correction of sea level at a rate of 1 cm hPa^{-1}, and also provided information on the speed and direction of winds blowing over the bay. All these data were subsampled to obtain hourly mean data during the experimental period.

As the number of acoustic stations is four, the maximum number of sound transmission lines is six. However, during this experiment, the number was reduced to five because sound transmission between H1 and H3 was severely interrupted by oyster aquaculture rafts (distributed along the transmission line). Even for the five remaining

successful lines, sound transmission was frequently interrupted by oyster rafts, which increased data gaps. Travel time data with signal-to-noise ratios (SNRs) greater than 4 (12.0 dB) were selected for further analysis. For larger SNR thresholds (>4), the amount of useful data decreases, and for smaller thresholds (<4), data quality decreases. It was confirmed by comparing the valid number and standard deviations of the observation data for SNR=3, 4 and 5. Data in the gaps were interpolated linearly (based on neighboring data). The range-averaged sound speed (temperature) can be calculated with strict positioning accuracy from one-way travel time data, whereas the range-averaged current requires two-way data and strict clock accuracy. Data gaps were greatly reduced by using one-way data in temperature calculations.

5.3 Error evaluation

5.3.1 Effect of range errors on sound speed and temperature

In the mathematical formulation for error estimate, sound speed (C) is calculated (using $C = L/t$) from the station-to-station range (L) and the one-way travel time (t). At $t = t_0$, the range deviation (δL) is transferred to the sound speed deviation (δC):

$$\delta C = \delta L / t_0 \quad . \tag{5.1}$$

For fixed L, the travel time deviation (δt) can be obtained

$$\delta t = -\frac{L}{C^2}\delta C \quad . \tag{5.2}$$

Sound speed is a function of temperature (T), salinity (S) and depth (H). When $S=S_0=31$ and $H=H_0=4$ m (typical value of the Hiroshima Bay experiment), the partial

derivative of sound speed reduces to:

$$\delta C = \left.\frac{\partial f(T,S,H)}{\partial T}\right|_{\substack{H=H_0=4m \\ S=S_0=31}} \delta T \quad . \tag{5.3}$$

According to MacKenzie's formula for sound speed [MacKenzie, 1981], at T_0=24 ^oC, we obtain

$$\delta C = 2.50\delta T \quad , \tag{5.4}$$

where H_0 and S_0 are averages determined from the CTD data. The effect of δT is transferred to δC with a factor of 2.5 within the observational range. The offset of sound speed and temperature, due to the range offset, is determined by equations (5.1) and (5.4), respectively (as shown in Table 5.4.1). It is worth noting that the temperature correction reaches a significant level of about 1 ^oC.

5.3.2 Effect of neglecting current

Due to temperature calculation using the one-way travel time data, we shall now discuss the effect of current on sound speed (converted to temperature by the sound speed formula). By substituting sound speed error (δC) and differential travel time (Δt) (calculated from equations (5.4) and (4.3), respectively) into equation (5.2), the relationship between the temperature error and current reduces to: $\delta T = -0.8V$ for L=5000 m and C_0=1500 ms^{-1} (typical values in Hiroshima Bay).

5.4 Results

5.4.1 Position correction

Owing to importance of accurate distance for the temperature calculation, the offsets exist between the subsurface acoustic transducer and the GPS antenna (Fig.5.2.1) should be adjusted by the position correction method which are proposed in chapter 2.3.

The original and corrected ranges for the five transmission lines are listed in Table 5.4.1.

Table 5.4.1 *Comparison of the GPS-determined and CTD-corrected ranges*

Station pair	H1-H2	H1-H5	H2-H3	H2-H5	H5-H3
GPS range (m)	3944.09	5629.06	5307.81	8922.46	8429.64
Corrected range (m)	3949.98	5620.68	5300.43	8925.46	8448.59
Range offset (m)	5.89	8.38	7.38	3.00	18.95
Sound speed offset δC (ms^{-1})	2.28	2.28	2.12	0.51	3.43
Temperature offset δT (°C)	0.91	0.91	0.85	0.20	1.37

5.4.2 Determining the weighting factors

Insufficient regularization is imposed on the corner sub-domains (1, 3, 7 and 9) and the side sub-domains (2, 4, 6 and 8). Thus, two weighting factors ($\beta 1$ and $\beta 2$) which are mentioned in the Chapter 2.2 are here determined by the root mean squares difference (RMSD) between the CAT solution and the CTD data on 18 Sept. The optimum values are determined to be $\beta 1 = 0.27$ and $\beta 2 = 1.0$ at the point with the minimum RMSD

value (Fig. 5.4.1). Note that $\beta 2$ may generally be useful for the grid method even if it is not effective in the present study.

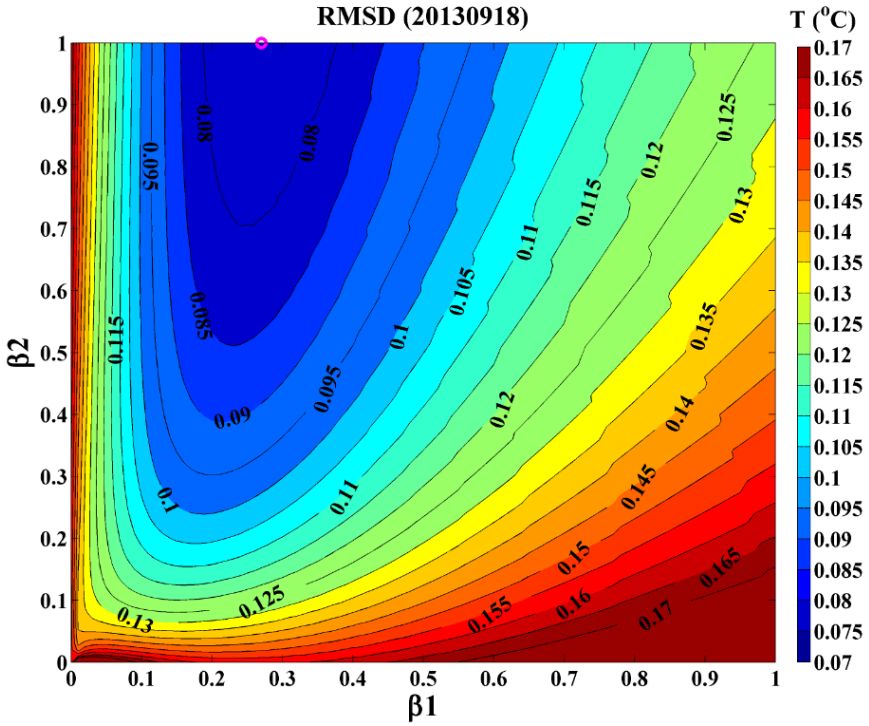

Fig. 5.4.1 *Distribution of RMSD between the CAT solution and CTD data on 18 Sept, plotted on the plane ($\beta 1$, $\beta 2$). The optimal values are marked with a purple dot.*

5.4.3 Acoustical data

A typical example of the received signals for each of the five transmission lines as obtained at 1000 JST on 18 Sept. 2013, close to the time the CTD data were acquired, is plotted in Fig. 5.4.2 with the signal-to-noise ratio (SNR). The travel times of the received signals were determined at the largest arrival peak (as indicated by the red dot). The estimated travel times were 2587.20, 3680.70, 3468.15, 5841.70 and 5529.15 ms with a time resolution of 0.05 ms (sampling frequency=20 kHz) for transmissions between H1→H2, H1→H5, H2→H3, H2→H5 and H5→H3, respectively.

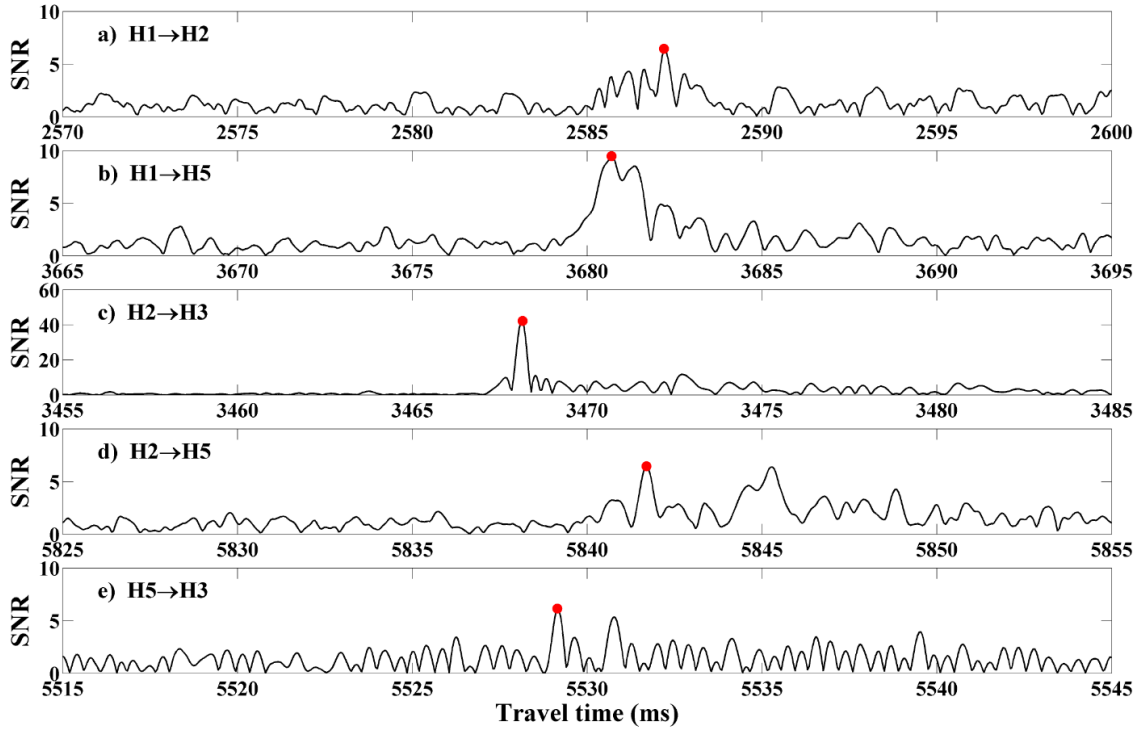

Fig. 5.4.2 *Typical examples of the correlation pattern obtained for each of the five transmission lines on 1000 18 Sept. The largest peak is indicated by a red dot.*

Figure 5.4.3 shows the ray patterns obtained along individual transmission lines by ray simulations that use the range-independent sound speed profile that is the averaged of CTD data from the three stations (C3, C8 and C9) near the center of the tomography domain. Sound speed remains nearly constant in the upper 2 m, but increases rapidly up to a depth of 4 m, and then increases gradually toward the seafloor, forming a near-surface waveguide. In the waveguide, all rays are confined to a depth range of 0 to 8 m, forming refracted-surface-reflected rays. Note that rays travelling with large amplitudes in the larger sound speed layer near the seafloor arrive earlier, in spite of longer ray lengths. The rays refracted near a depth of 8 m that correspond to the largest arrival peaks with a small number of surface reflections are drawn with red lines. The simulated travel times are 2585.40, 3679.40, 3469.10, 5841.10 and 5530.10 ms for H1→H2, H1→H5, H2→H3, H2→H5 and H5→H3, respectively. The simulated travel times are in rough agreement

with the observed travel times. Offsets between the travel times with magnitudes of about 1 ms come from the incorrectness of the range-independent ray simulations.

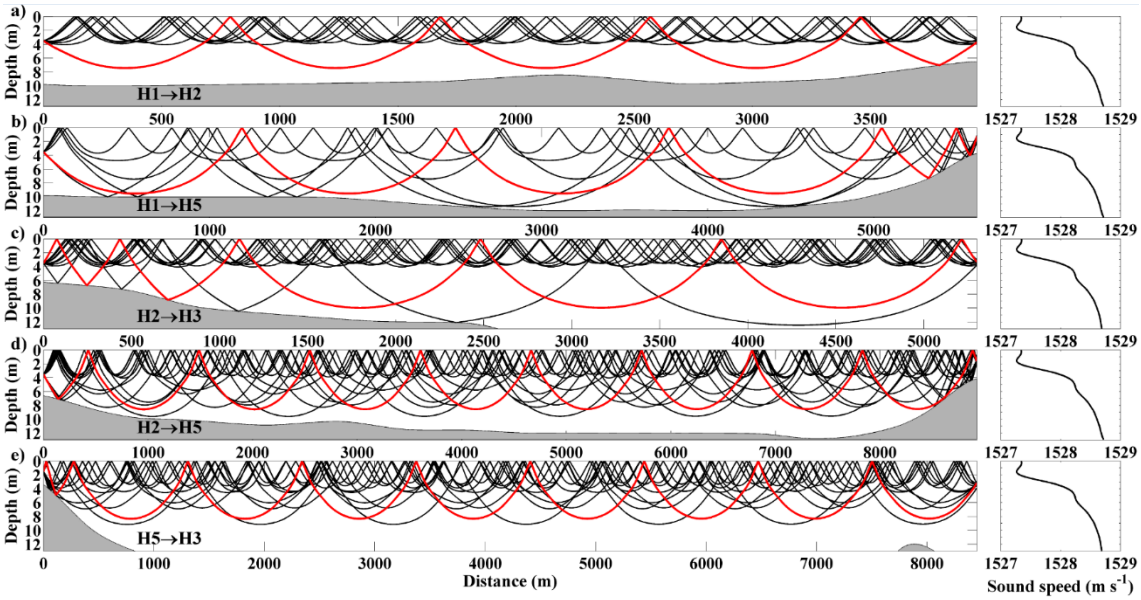

Fig.5.4.3 *Range-independent ray simulation along each transmission line. The red line indicates the ray corresponding to the travel time, which was used in the inversion.*

5.4.4 Oceanographic data

1) CTD temperature

Horizontal distributions of temperature were plotted at depths of 1, 3, 6 and 10 m, using the CTD data obtained on 18 Sept. (Fig. 5.4.4). Most regions deeper than 5 m were occupied by water colder than 24 ºC. This cold water appeared in the southern half of the observation domain in the 3-m section and shrank toward the southwest corner in the 1-m section. Around the northeastern corner, near-surface water was masked by warm water (24.5-24.9 ºC) discharged by the Ota River.

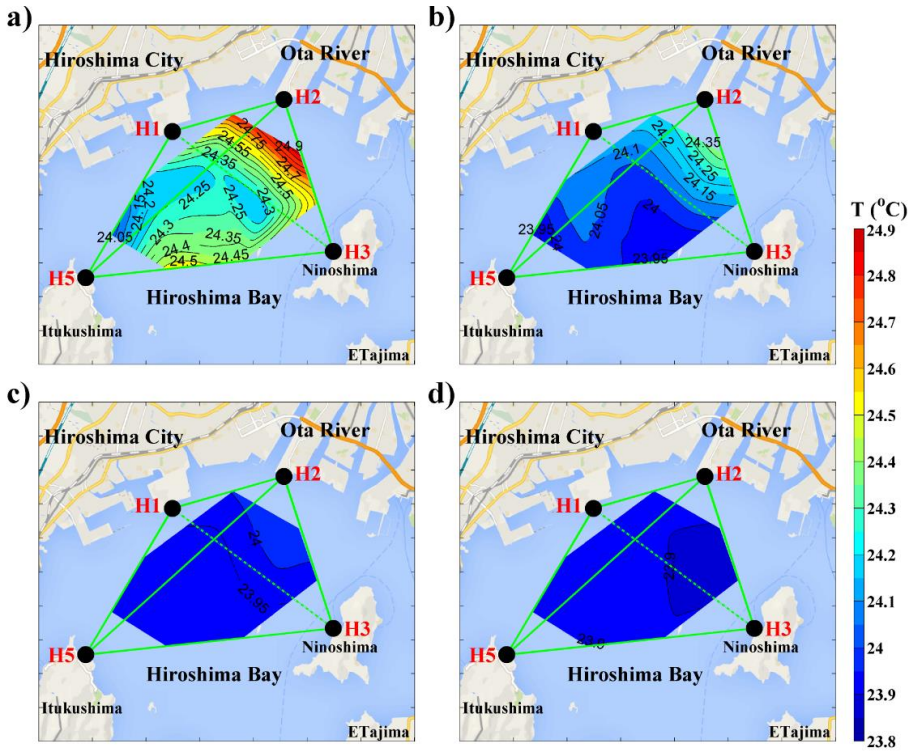

Fig. 5.4.4 *Temperature distributions in the horizontal section, constructed from the CTD data on 18 Sept. for depths of (a) 1m, (b) 3m, (c) 6m and (d) 10 m, respectively.*

Vertical sections of temperature were constructed from the CTD data along the transects C6-C8-C9-C1 and C5-C4-C3-C2, respectively (Fig. 5.4.5). Cold water (24.1 ^{o}C) sloped upward between C6 and C9 and was exposed to the surface around station C6, implying that coastal upwelling was occurring. Cold water was also lifted up around C3 and C4, where 24.1 ^{o}C water occurred around 2 m below the surface. The layer deeper than 5 m was occupied by water colder than 24 ^{o}C.

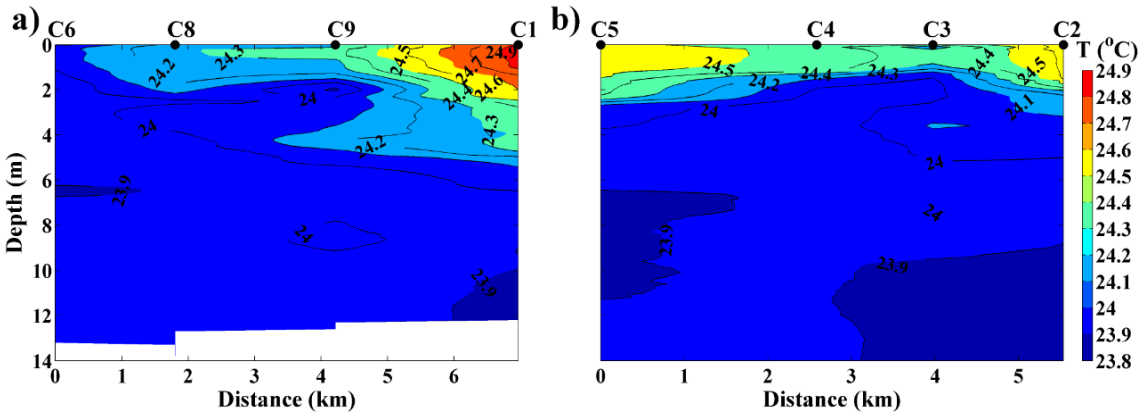

Fig. 5.4.5 *Contour plots of temperature in the vertical sections, constructed from the CTD data on 18 Sept. The left and right panels are for the transects C6-C8-C9-C1 and C5-C4-C3-C2, respectively.*

2) CAT temperature

(a) Path-average

Path-averaged temperatures during the 11-25 Sept. were calculated from one-way travel time data for each of the five transmission lines, and shown with the time plots in Fig. 5.4.6. Temperature varied within a range of 1 °C. Large temperature variations occurred along all the transmission lines after the strongest influence of typhoon T1318 on 16 Sept. Temperature decreased continuously (slanted red arrows) in all the time plots during 16-17 Sept. The diurnal minima of temperature (thick vertical arrows) apparent beginning on 18 Sept. were especially prominent along transmission lines H1-H5 and H2-H5, traversing the central part of the domain. The diurnal oscillation damped with advancing time and largely disappeared by 21 Sept.

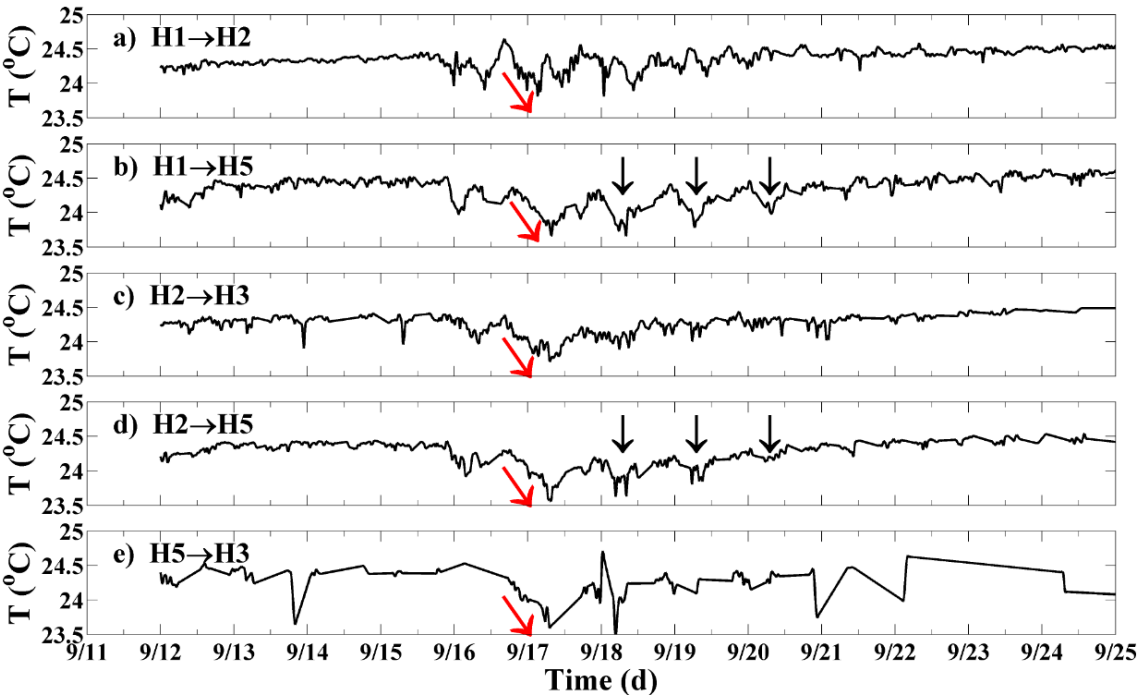

Fig. 5.4.6 *Time plots of the path-averaged temperature calculated for each of the five transmission lines from 0000 11 Sept. to 0000 25 Sept.*

(b) Distribution in the horizontal slice

The results of inversion for the 2-day low-pass filtered temperature, averaged in the upper 8 m, are shown at a bi-hourly intervals with the contour plots in Fig. 5.4.7, between 0000 on 15 Sept. and 2200 on 20 Sept. The hourly mean wind speed and sea level are also shown with vector and time plots on the upper and lower sides, respectively. The observation domain was covered with warm water (greater than 24.4 ºC) until 2000 on 15 Sept., prior to typhoon T1318. Water then cooled gradually with strengthening northerly winds and reached a minimum temperature of 23.9 ºC at 0600-1400 on 17 Sept., forming a cold water zone that extended in an east-west direction. After that, temperature in the extended zone increased. At 2200 on 19 Sept., the temperature became 24.2 ºC, which was 0.2 ºC lower than the pre-typhoon temperature (24.4 ºC).

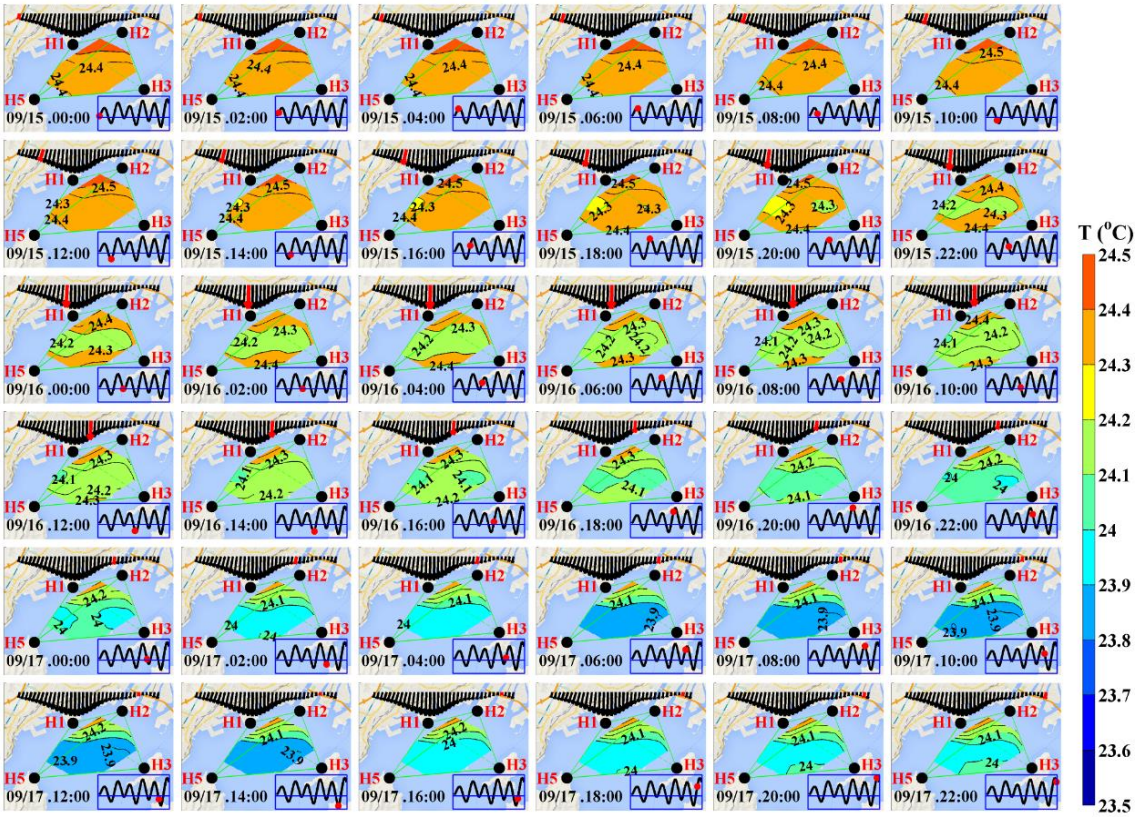

Fig. 5.4.7 *(a) Temporal variations of the 2-day low-pass filtered temperature distribution reconstructed at a bi-hourly interval from 0000 15 Sept. to 2200 17 Sept. The date and the hourly mean sea level variation are indicated in the bottom left and bottom right parts of each panel, respectively. Wind vectors are shown on the upper side. The sea level and wind are indicated by red dots and red arrows, respectively, on the corresponding time plot.*

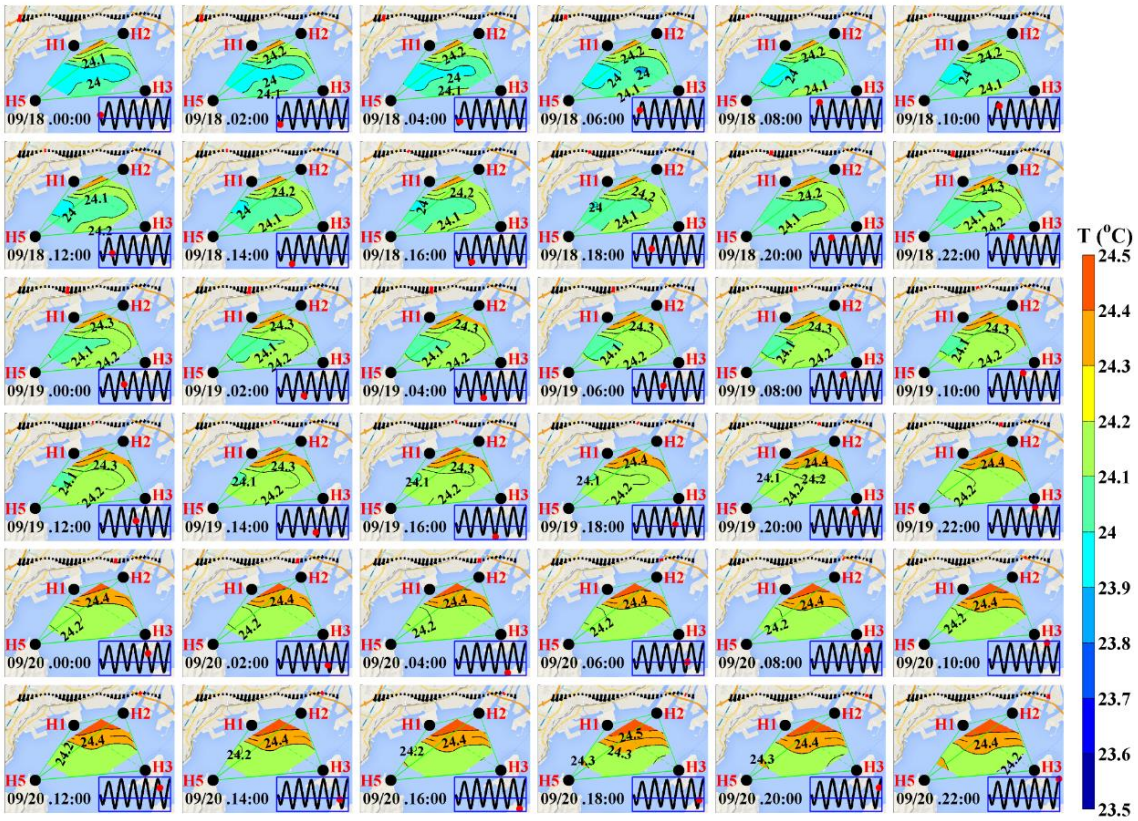

Fig. 5.4. *7 (b) continue from 0000 18 Sept. to 2200 20 Sept.*

The variations in the temperature anomaly processed through a 1-hour to 2-day band-pass filter are shown by the contour plots in Fig. 5.4.8. A zone with a cold water anomaly first appeared around the time of maximum northerly wind (0400 on 16 Sept.) and was replaced by a warm water zone half a day later. The alternation of cold and warm water zones occurred repeatedly at the diurnal period (0800 of 17, 18 and 19 Sept. for the cold water zone). The cold water zones damped with advancing time and split sporadically into two east-west arrayed segments, as seen at 0600 on 18 and 19 Sept.

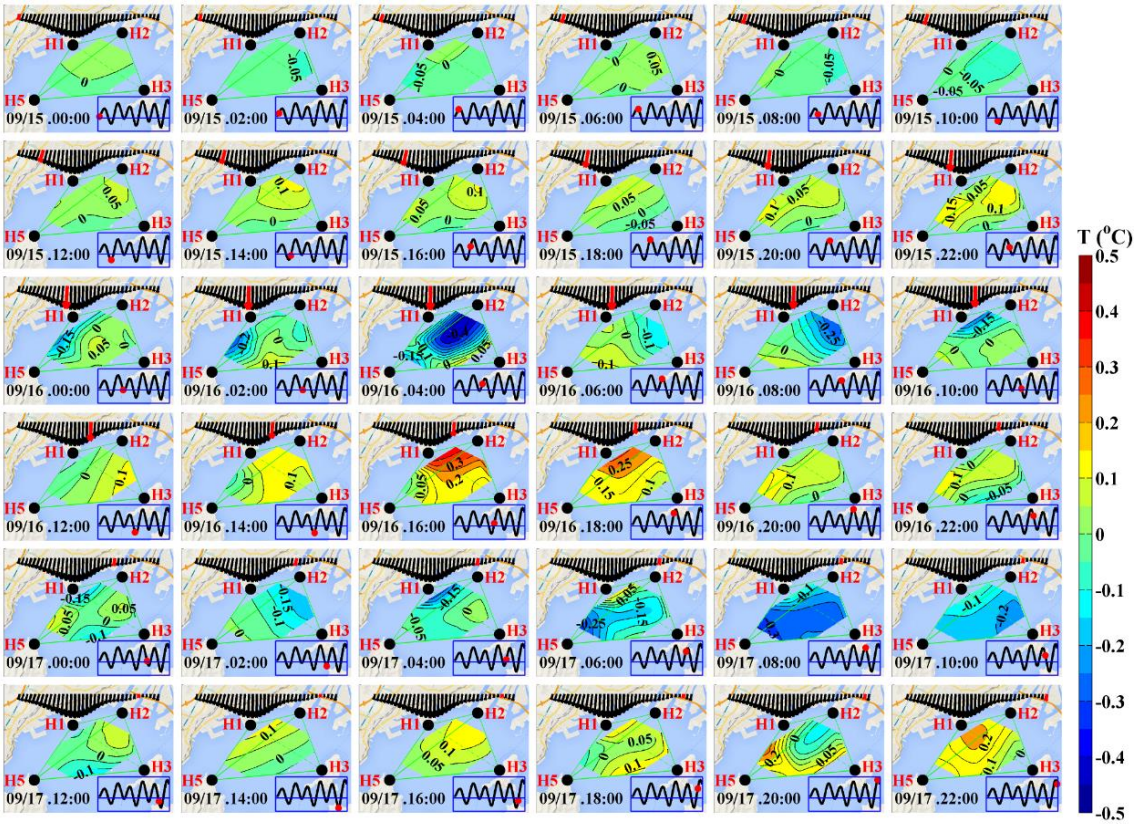

Fig. 5.4.8 *(a) Horizontal distributions of the 1-hour to 2-day band-pass filtered temperature, reconstructed at a bi-hourly interval from 0000 15 Sept. to 2200 17 Sept. The date and the hourly mean sea level variation are indicated in the bottom left and bottom right parts of each panel, respectively. Wind vectors are drawn on the upper side. The sea level and wind are indicated by red dots and red arrows, respectively, on the corresponding time plot.*

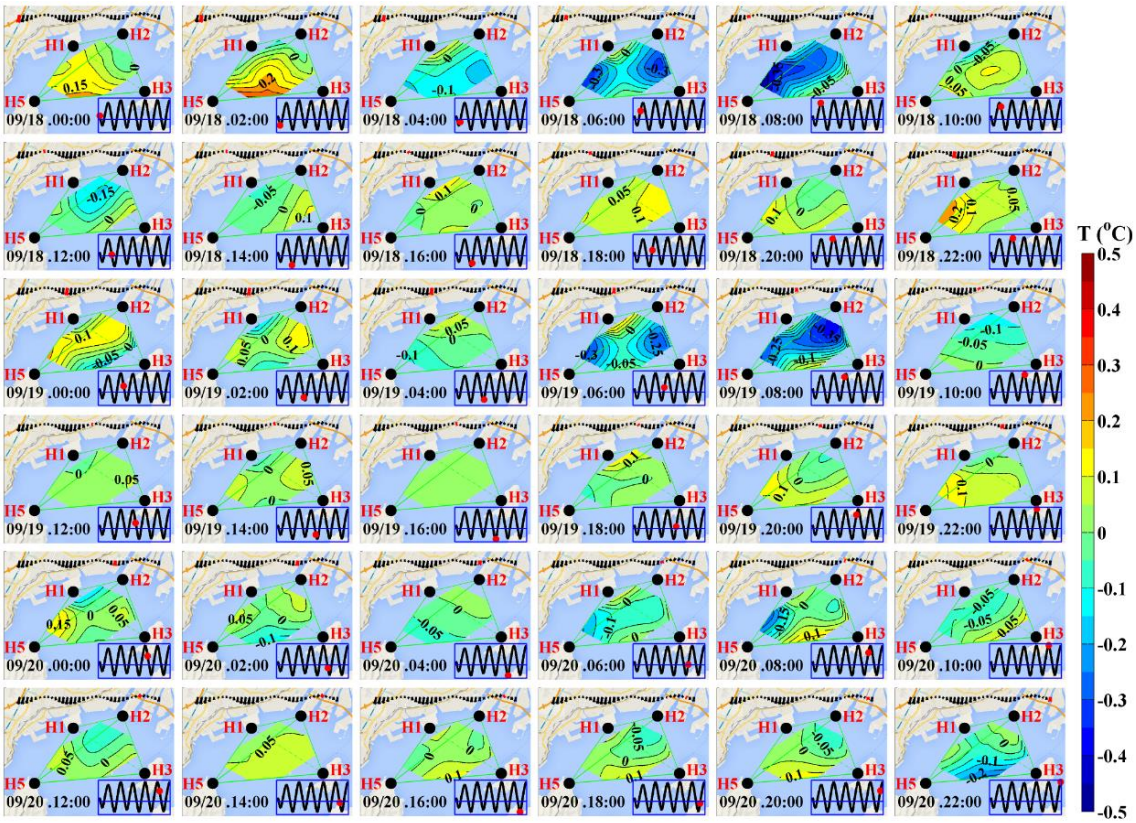

Fig. 5.4.8 *(b) continue from 0000 18 Sept. to 2200 20 Sept.*

5.5 Discussion

5.5.1 Estimating temperature error

The horizontal distributions of temperature, reconstructed from inverse analysis of one-way travel time data, were compared with those constructed from the CTD data for the upper 8 m (Figs.5.5.1a and 5.5.1b). Overall, there was good agreement between the datasets, and the CAT and CTD data varied in the same range (from 23.95 to 24.35 ^{o}C). Warmer water (above 24.3 ^{o}C) existed in the northeastern part of the observation domain in both cases. The temperature difference between the two datasets was small in all regions except for the northern and southern borders (Fig.5.5.1c).

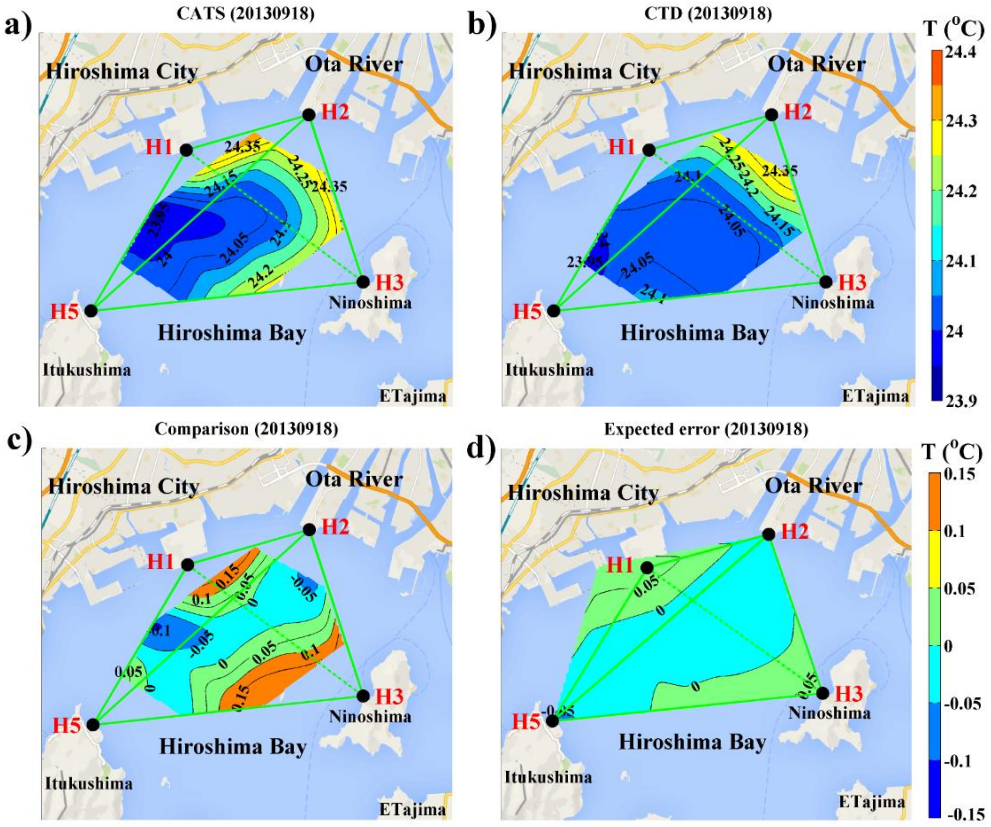

Fig. 5.5.1 *Comparison of the temperature distributions for the upper 8 m, obtained by (a) CAT and (b) CTD on 18 Sept. The temperature difference between (a) and (b) is also shown in (c).The expected error of inversion is shown in (d) with a domain different from (a), (b) and (c).*

The root mean squares difference (RMSD) between the datasets was 0.079 ºC. The expected error of inversion provided in equation (2.18) was less than 0.05 ºC in most regions (Fig.5.5.1d) and the standard deviation was as small as 0.037 ºC. Reciprocal transmission was successfully performed between H1 and H2 in the present experiment. The hourly mean and 2-day mean currents were calculated for the whole period and the mean current was 9.1 cm s^{-1} (directed to H2 from H1) for about two hours during the CTD casts (Fig.5.5.2). The temperature error associated with this mean current is 0.073 ºC, which was close to the 0.079 ºC determined in comparison with the CTD data. Both the

observation errors were twice as large as the estimated inversion error (0.037 ^{o}C), implying that the major source of observation errors comes from neglecting the current effect. The comparison and error estimation validates the appropriateness of inversion using the grid method, accompanied by regularization and additional weightings. It should be noted that no improvements were obtained when the generalized inversion without considering errors and the damped least squares method without smoothing procedures were applied (not shown here).

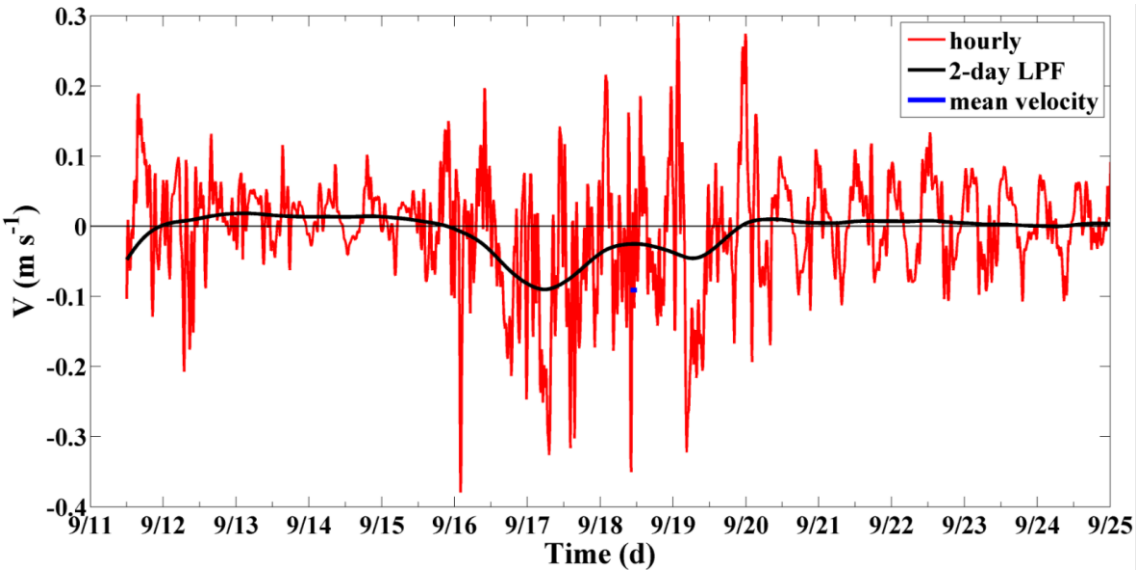

Fig. 5.5.2 *Time plot of the depth-averaged current along the H1-H2 line (directed to H2 from H1). The red and black lines indicate the hourly and 2-day mean currents, respectively. The blue bar indicates the two-hour mean current during the CTD cast.*

5.5.2 Coastal upwelling and diurnal internal tides

The upwelling process in Hiroshima Bay may be simplified by dividing the water column into two layers (an upper layer of 0-3 m and a lower layer of 3-8 m) with the interface at the depth of the steepest sound speed gradient. The CAT measured the average temperature for both layers and the inverted data were interpolated to the temperature array point T1.

The 2-day low-pass filtered CAT temperatures were compared with the 2-day low-pass filtered temperature array data for the upper and lower layers, the 2-day to 1-month band pass-filtered 4-hour interval wind speed data and the 5-min interval sea level data, during the 11-25 Sept. (Fig. 5.5.3.a). The CAT temperature decreased with the growth of upwelling, from 24.33 ^{o}C at 0000 on 15 Sept. to 23.90 ^{o}C at 1000 on 17 Sept. During 16-18 Sept., the CAT, temperature array and CTD data were close to each other and had the same tendencies. However, around the mature phase (on 17 Sept.), the CAT and upper-layer array temperatures were slightly lower than the lower-layer array temperature. This phenomenon, also shown by the CTD data, may be caused by sudden atmospheric cooling due to the strong northerly wind. Except for the above period, the CAT temperature fell between the upper-layer and lower-layer array temperatures. Note that surface cooling due to the strong northerly wind was spread over the whole bay, whereas the upwelling was confined to the northern along-shore region. Thus, the upwelling itself was little disturbed by surface cooling. Furthermore, the water column remained stable even when the surface cooled, because the upper layer contained less saline water (due to freshwater discharge from the Ota River).

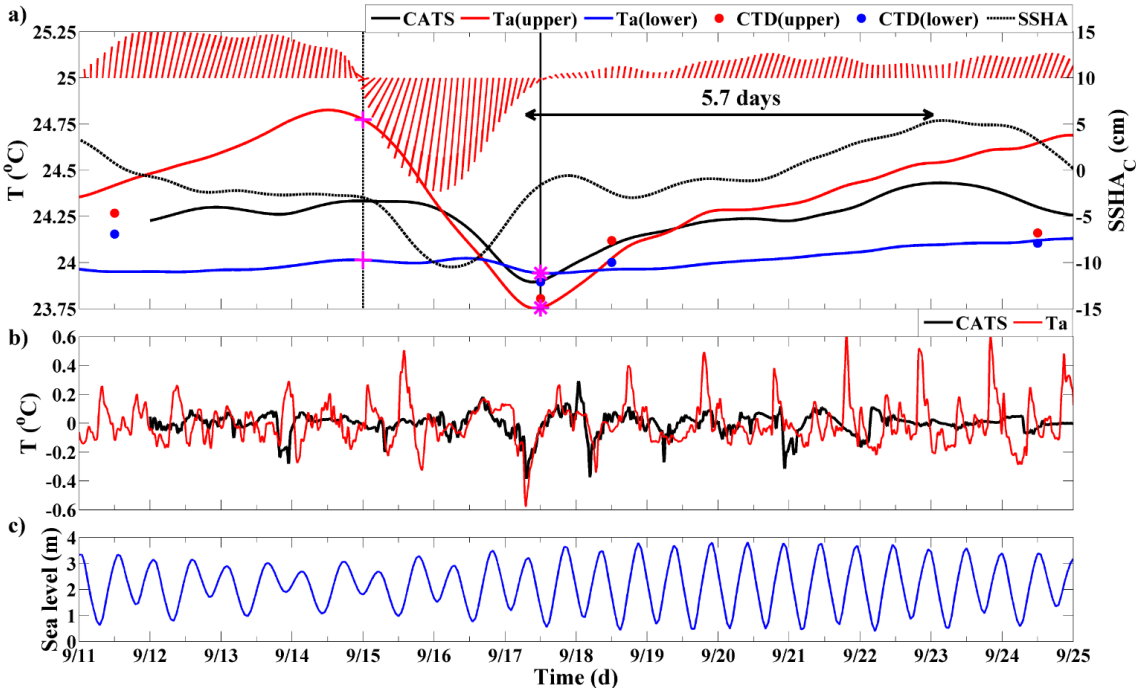

Fig. 5.5.3 *(a) Time plot of the 2-day low pass filtered CAT temperature data (black solid line) together with the hourly sea level data (black broken line) in the subtidal range (2-day to 1-month band-pass filtered) and the 2-day low-pass filtered temperature array data for the upper (red line) and lower (blue line) layers. The red and blue dots indicate the CTD data for the upper and lower layers, respectively. The 4-hour interval wind data smoothed through the (2-day to 1-month) filter, are also shown in the upper part of the figure. The thick horizontal line edged with arrows indicates half the period of the first-mode internal seiches, bounded at the north-south shores of the bay. The marks '+' and '*' placed on the vertical broken and solid lines show the initial and mature phases of upwelling, respectively. (b) Time plots of the 1-hour to 2-day band-pass filtered CAT temperature (black line) and temperature array data (red line). (c) Time plots of the hourly mean sea level variations.*

A significant sea level depression of 7.5 cm occurred several hours after the northerly wind started to blow over Hiroshima Bay. This depression may have been

caused by the offshore (southward) transport of near-shore surface water due to the strong northerly wind. The temperature decrease followed the sea level depression with a time lag of 1.1 days, which corresponds to the growth time of the coastal upwelling. With diminishing northerly winds on 17 Sept., warm water that was transported southward returned to the northern shore as internal seiches or surges. This return of warm water gradually increased the sea level and the temperature until 23 Sept. The sea level anomaly on 23 Sept. was greater by 8.3 cm than the value before the northerly wind began, but the temperature was almost the same before and after the northerly wind. The data obtained during the six-day duration from 17 to 23 Sept. are in good agreement with half the period of the first mode internal seiches (5.7 days) with a north-south bay length of 50 km [Zhang et al., 2014].

The 1-hour to 2-day band-pass filtered temperature data are shown in Fig. 5.5.3b for both the CAT and the temperature array data. Hourly sea level data are presented in Fig. 5.5.3c. The diurnal internal tide was prominent after the diminishing phase of the coastal upwelling on 18 Sept. In the CAT data, the diurnal internal tide continued until 22 Sept., with dominant semi-diurnal external tides and after that suddenly diminished. In contrast, the array data showed semi-diurnal external tides with a prominent magnitude until 25 Sept., when the diurnal external tides grew in addition to the semi-diurnal external tides. For the CAT data processed with horizontal averages, the diurnal internal tides may be less pronounced (in terms of horizontal average) during 22-25 Sept., because the internal tides had different wavelengths.

The diurnal internal tides (array data) were clearly coupled with the semi-diurnal external tide (tide gauge station data) during 18-20 Sept., in spite of a time lag of a few hours (Fig. 5.5.3.b). This implies that the diurnal internal tide was excited through parametric subharmonic instability by the regular semi-diurnal external tide that developed around the spring tide (which occurred from 19 to 21 Sept.) in Hiroshima Bay.

5.5.3 Growth and mixing of upwelling

During the upwelling event, the upper-layer temperature decreased, whereas the lower-layer temperature remained constant (Fig. 5.5.3a). During the initial and mature phases of upwelling, as determined from both the CAT and the temperature array data, the mean temperature (T_1) for the upper layer at time t may be written:

$$T_1(t) = T_{10}\{1-\alpha(t)\} + T_{20} \times \alpha(t) \quad , \tag{5.5}$$

where T_{10}=24.77 ºC and T_{20}=24.01 ºC are the temperatures at the initial phase for the upper and lower layers, respectively, and α is the upwelling fraction of the water originally in the upper layer that has been replaced by lower layer water. Because α depends on t, α is zero for no upwelling and one for complete upwelling, during the mature phase. From equation (5.5), α is determined as follows:

$$\alpha(t) = \frac{T_{10} - T_1(t)}{T_{10} - T_{20}} \quad , \tag{5.6}$$

where $T_1(t)$ is determined from the temperature array data for the upper layer. Fig. 5.5.4 shows that α increased continuously from 0 at 0000 on 15 Sept., to 1.34 at 1000 on 17 Sept. during the mature phase, and gradually decreased after that. On 17 Sept., α was unexpectedly above one, due to the sudden atmospheric cooling. Upwelling is a localized phenomenon along the coast, whereas surface heating and surface cooling spread over the whole bay. Thus, the growth of the upwelling is not disturbed significantly by the surface cooling. The values of α calculated from the CTD data on Sept. 17 and 18 were close to those computed from the array data.

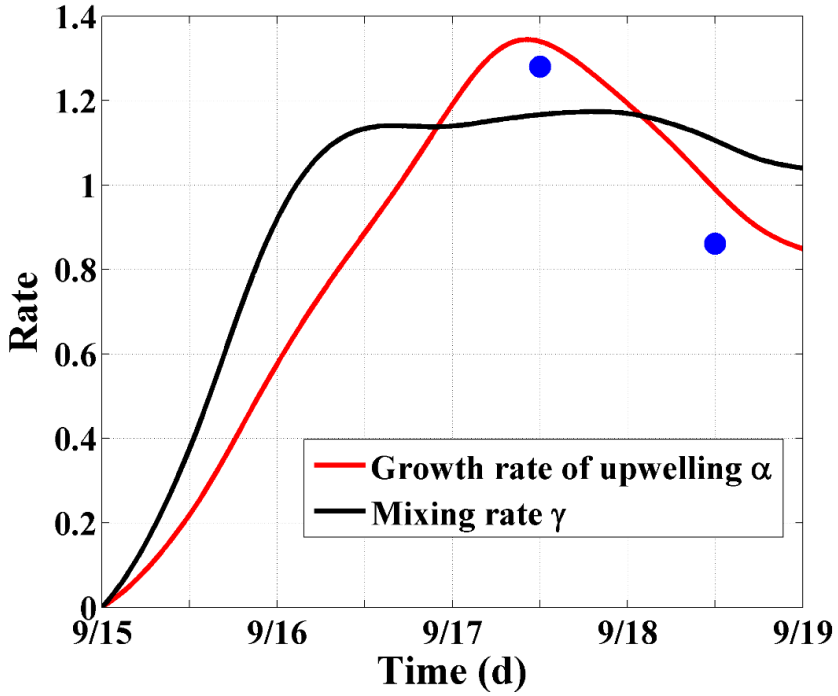

Fig. 5.5.4 *Time plot of the upwelling and mixing fractions from Sept.15 to Sept.19. The red and black lines show the results from the temperature array and CAT data, respectively. The blue dots are plotted based on the CTD data obtained on Sept.17 and 18.*

On the other hand, the CAT temperature T_{CAT} *(t)* provides the depth-weighted average for the upper and lower layers:

$$T_{CAT}(t) = \frac{T_1(t)h_1 + T_{20}h_2}{h_1 + h_2} \quad , \tag{5.7}$$

where h_1 and h_2 are the thickness for the upper and lower layers, respectively. By using T_{CAT}, the mixing fraction γ for the upper and lower layers may be defined as follows:

$$\gamma(t) = \frac{T_{10} - T_1(t)}{T_{10} - T_{CAT}(t)} \quad . \tag{5.8}$$

In the above equation, γ is zero at $t = 0$ and one when $T_1(t) = T_{CAT}(t)$. The value of γ was 1.17 during the upwelling's mature phase. No significant difference existed between the upwelling's growth and mixing processes.

Finally, the upwelling velocity may be simply formulated by:

$$w_e = \frac{h_u}{t_e} \quad , \tag{5.9}$$

where $h_u = \frac{h_1 + h_2}{2}$ is half the total thickness for the upper and lower layers (= 4 m), and t_e is the time elapsed between the initial (maximum northerly wind) and the mature phase (minimum temperature) of the upwelling. According to both the CAT data and the array data, t_e was 27.3 hours. The resulting upwelling velocity was 0.0041 cm s^{-1} (3.52 m day^{-1}).

5.6 Summary

The horizontal distributions of coastal upwelling and the associated diurnal internal tide generated in the northern part of Hiroshima Bay were mapped at 10 minute intervals by four coastal acoustic tomography (CAT) systems which surrounded the observation domain. This upwelling event occurred during 16-17 Sept. 2013 and was caused by a strong northerly wind that, in turn, was due to typhoon T1318, which passed along the eastern side of the bay on 16 Sept.

Path-averaged sound speed (temperature) was calculated for the five sound transmission lines, using one-way travel time data. Special attention was paid to positioning accuracy so that sound speed (temperature) could be measured accurately. Station-to-station ranges, estimated from GPS, were corrected in such a way that the

sound speed determined from the one-way travel time data is equated to that calculated from a couple of CTD datasets along each transmission line. In addition, station positions were adjusted to make a focal point at the geographical position of each transducer.

The horizontal distributions of temperature (averaged over the upper 8 m) were reconstructed (at a 10-min interval) by regularized inversion, using the one-way travel time data obtained along the five transmission lines. The correctness of the inverse method, based on the grid method accompanied by regularization and additional weightings, was well validated in comparison with the CTD data. The current-derived error and the root mean squares differences (RMSDs) of the datasets were 0.073 ^{o}C and 0.079 ^{o}C, respectively, and approximately twice the estimated inversion error (0.037 ^{o}C). This implies that neglecting the current was a major source of error.

The CAT results were examined for two time-scales: 2-day low-pass filtered range and 1-hour to 2-day band-pass filtered range. In the former range, the coastal upwelling in Hiroshima Bay was initiated around 15 Sept., when the northerly wind started to blow over the bay, and reached the mature phase with a minimum temperature of 23.9 ^{o}C at 1000 on 17 Sept., forming an east-west extended cold water zone. The extended zone continued to weaken until 1800 on 18 Sept. and finally, the water temperature returned to 24.2 ^{o}C at 2200 on 19 Sept., which was lower by 0.2 ^{o}C than the pre-typhoon value (24.4 ^{o}C). The parallel increase of temperature and sea level from 17 Sept. (the mature phase of upwelling) to 23 Sept. implies the generation of north-south bounded internal seiches or surges with a period of 11.4 days. In the latter range, a cold water anomaly first appeared at 0800 on 18 Sept. after the mature phase of the upwelling (1000 on 17 Sept.) and reappeared with a one-day period. This diurnal internal tide was pronounced during the decay of the coastal upwelling on 18 Sept. and continued from 18 to 22 Sept., including the spring tide period (from 19 to 21 Sept.) when semi-diurnal external tides were prominent. These diurnal internal tides were still pronounced during the developing phase (22 to 25 Sept.) of the diurnal external tides in the temperature array data, although

they were diminished in the CAT data. The diurnal internal tides (array data) were clearly coupled with the semi-diurnal external tide (tide gauge station data) during 18-20 Sept., in spite of a few hours of lag time. The excited diurnal internal tides may be replaced by the occurrence of near-inertial waves with a period of 21.5 hours in spite of slightly inappropriate periodicity [Onuki and Hibiya, 2015]. Further study is required to understand the mechanism behind this wave coupling.

The upwelling fraction (α) was formulated and estimated using the temperature array data. The α continuously increased, from zero during the initial phase of the upwelling to one during the mature phase. The mixing fraction (γ) in the growth of upwelling was also estimated by the CAT data. Both upwelling and mixing processes followed almost the same curve. This similarity in upwelling and mixing processes suggests that mixing developed as the upwelling grew. The upwelling velocity was 0.0041 cm s^{-1} (3.52 m day^{-1}).

It is concluded that CAT is a quite powerful instrument for mapping the rapidly varying structures of coastal upwelling and the diurnal internal tides coupled with the semi-diurnal external tides.

References

Appt, J., Jo¨rg Imberger and H. Kobus. (2004). Basin-scale motion in stratified Upper Lake Constance, *Limnol. Oceanogr.,* **49**, 919–933.

David C. L. L., and W. M. Schertzer. (1999). Potential Climate Change Effects on Great Lakes Hydrodynamics and Water Quality. Reston, 217 pp., American Society of Civil Engineers.

Hunt, G. L., Jr. (1995). Oceanographic Processes and Marine Productivity in Waters Offshore of Marbled Murrelet Breeding Habitat, *USDA Forest Service Gen. Tech. Rep.*, **PSW-152**, 219-222.

Gill, A. E. (1982). Atmosphere- Ocean Dynamics. 662 pp., Academic Press, New York.

Hutter, K. (2012). Nonlinear Internal Waves in Lakes, 277 pp., Springer, Berlin.

MacKenzie, K. V. (1981). Nine-term equation for sound speed in the ocean, *J. Acoust. Soc. Am.*, **70**, 807-812.

Onuki, Y. and T. Hibiya. (2015). Excitation mechanism of near-inertial waves in baroclinic tidal flow caused by parametric subharmonic instability, *Ocean Dynamics*, **65**, 107-113.

Taylor, C. B. and H. B. Stewart, Jr. (1959). Summer upwelling along the east coast of Florida, *J. Geophys. Res.*, **64**, 33-40.

Thomson, R. E. (1981). Oceanography of the British Columbia coast, 281 pp., Minister of Supply and Services, Canada.

Zhang, C Z, A. Kaneko, X-H. Zhu and J. Lin. (2014). Non-tidal sea level changes in Hiroshima Bay, Japan. *Acta Oceanologica Sinica.*, **33**, 47-55.

Chapter 6 Integrated discussion

6.1 Vertical-slice inversion in Hiroshima Bay

6.1.1 Reciprocal travel time data for the first and second arrival peaks

In Hiroshima Bay, reciprocal travel times are obtained only along the limited sound transmission lines because transmission signals are seriously disturbed by the oyster rafts distributed inside the tomography domain. Horizontal currents are calculated from travel time differences in reciprocal transmission in contrast with temperature calculated from the one-way data.

Figure 6.1.1 shows the time plot of the reciprocal travel time for the first and second arrival peaks. The second peaks are 1 ms-5 ms behind the largest peaks. The wind velocity is also shown with the time plot at uppermost of the figure. Travel times are suddenly disturbed on Sept. 16 by the strong northerly winds due to the typhoon and this effect continues significantly up to Sept. 20. In consideration of the time variations, the observation period is divided into three parts: Period 1 (pre-typhoon) for Sept. 11-15, Period 2 (in-typhoon) for Sept. 16-20 and Period 3 (post-typhoon) for Sept. 21-26. Diurnal and semi-diurnal variations are pronounced during the post-typhoon period while these variations are not visible during the pre-typhoon period.

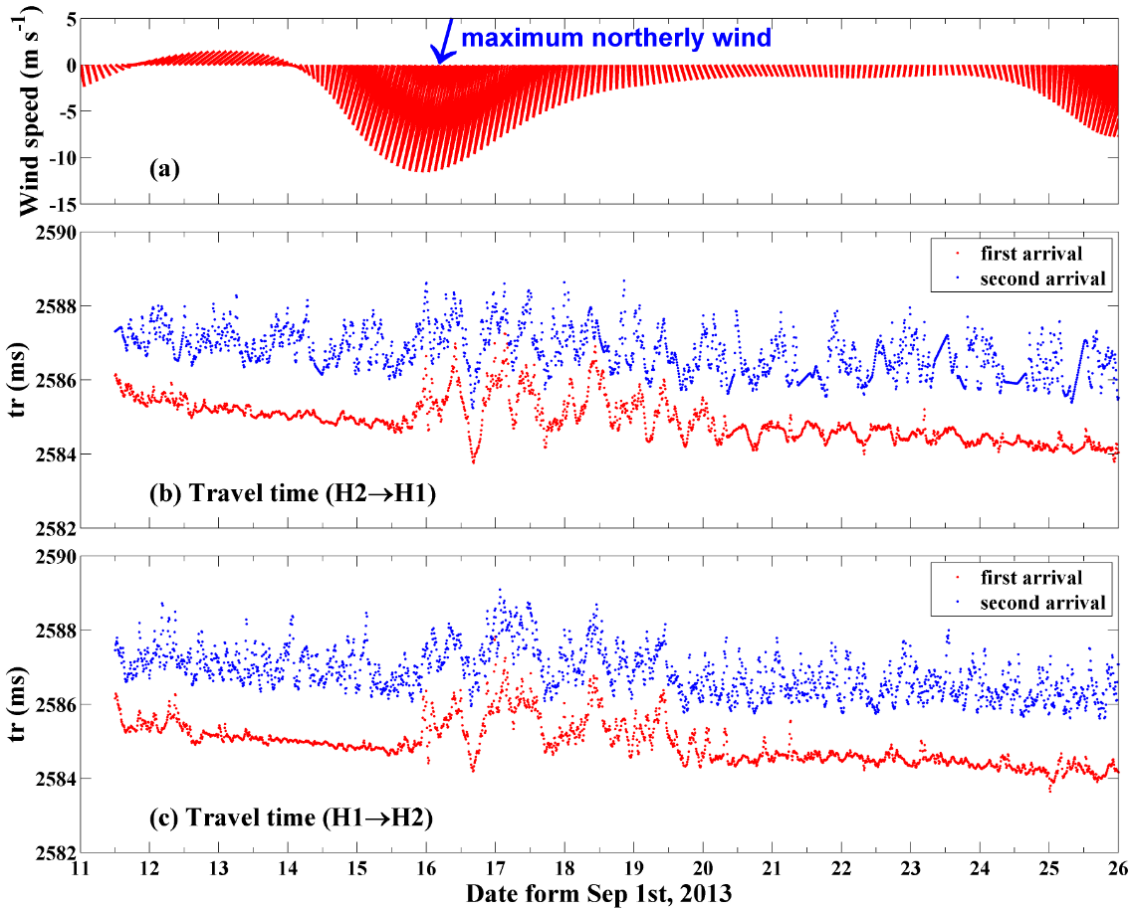

Fig. 6.1.1 *Time plots of reciprocal travel times for the first and second arrivals obtained on both sides along the H-H2 line (b, c). The wind velocity is also shown in uppermost of the figure (a).*

The travel time summation and difference obtained along the H1-H2 line are shown in Fig. 6.1.2 with the time plots. The down-slope trend of the travel time summation is caused by the seasonal warming toward late September, forming the temperature variation the same as in Fig. 6.1.1. The travel time summation is larger for the second arrival than for the first arrival. It means that the second arrival ray travels the regions colder than the first arrival ray. The travel time summation and fifference are remarkably scattered around a mean during the Period-2, especially for the travel times summation data. It should be noted that the semi-diurnal tidal oscillation is manifested in the travel time difference data

during Period-3. The propagation direction of semi-diurnal external tides make an angle to the transmission line T1-T2, they can be measured by the along-line measurement.

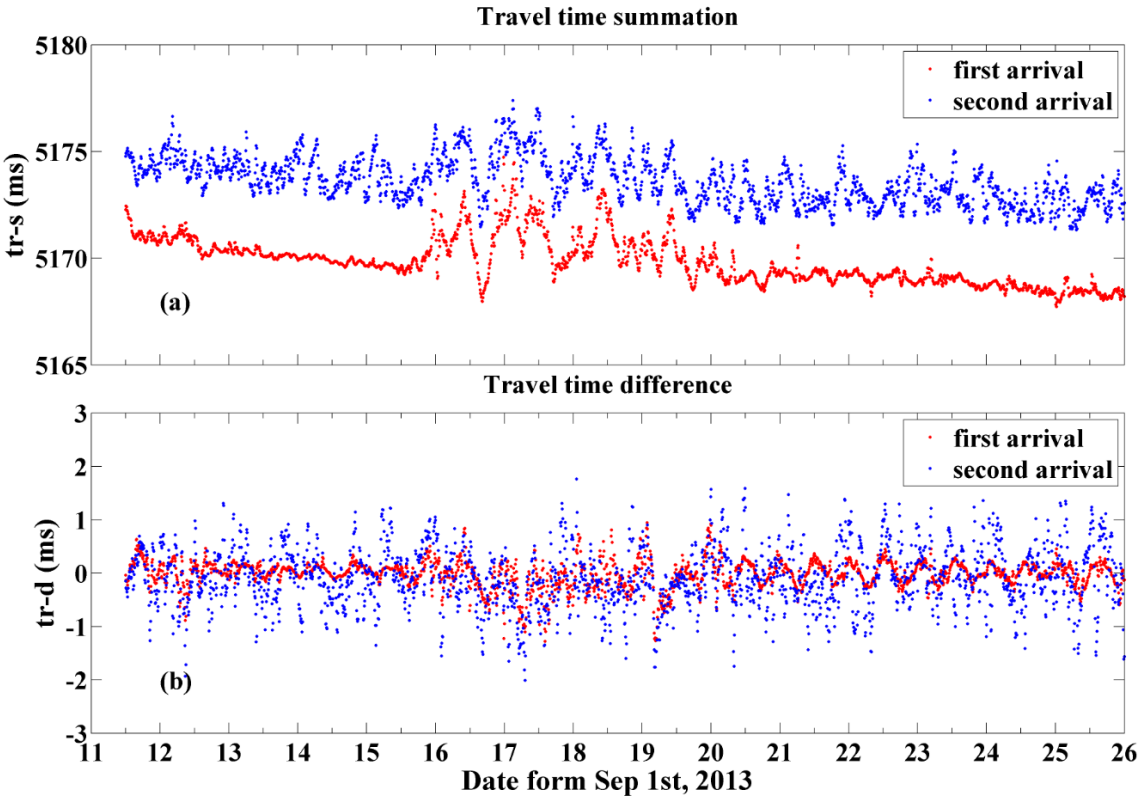

Fig. 6.1.2 *Time plots of the travel time (a) summation and (b) difference obtained for the first and second arrivals along the H1-H2 line.*

6.1.2 Range-independent ray simulation

The sound transmission process between the acoustic stations H1 and H2 is simulated by the ray tracing method [Dushaw and Colosi, 1998]. This is performed by using the range-averaged sound speed profile, estimated from the CTD data inside the tomography domain. The range-independent ray simulation accompanied by the range-dependent bottom topography is performed to determine the ray patterns during the Periods 1, 2 and 3 along the H1-H2 transmission line. For Periods 1 and 3, the weekly

CTD data, provided by the Hiroshima City Fisheries Promotion Center (HCFPC), were used. During Period 2, the CTD casts were done using a small fishing boat. The CTD data not only provide the vertical profile of sound speed in the tomography domain, but also validate the CAT observations.

Figure 6.1.3 shows the ray pattern for each period along the H1-H2 transmission line together with the reference sound speed profile. The travel times, ray paths and ray lengths for multi-rays (at least two rays) are needed in the vertical-slice inversion. For Periods 1 and 2, sound speed gradually increases toward the seafloor, forming a near-surface waveguide in the upper 4 m. On the other hand, in Period 2, the near-surface waveguide is confined to the upper 2 m, and sound speed is decreased with depth from the maximum sound speed depth to the seafloor. Note that variation ranges of sound speed from surface to seafloor are suddenly decreased owing to the typhoon effect from 7 ms^{-1} for Period 1 to 1.5 ms^{-1} for Period 2. The variation range is further decreased to 1.0 ms^{-1} for Period 3 by the surface cooling. Ray patterns are shifted from the refracted-surface-reflected in Periods 1 and 2 to refracted-bottom-reflected in Period 3, depending on the sound speed profiles. The first and second arrival rays are colored red and blue, respectively. Of course, travel times for the first and second arrival rays are close to those for the first and second arrival peaks, obtained in the field observation.

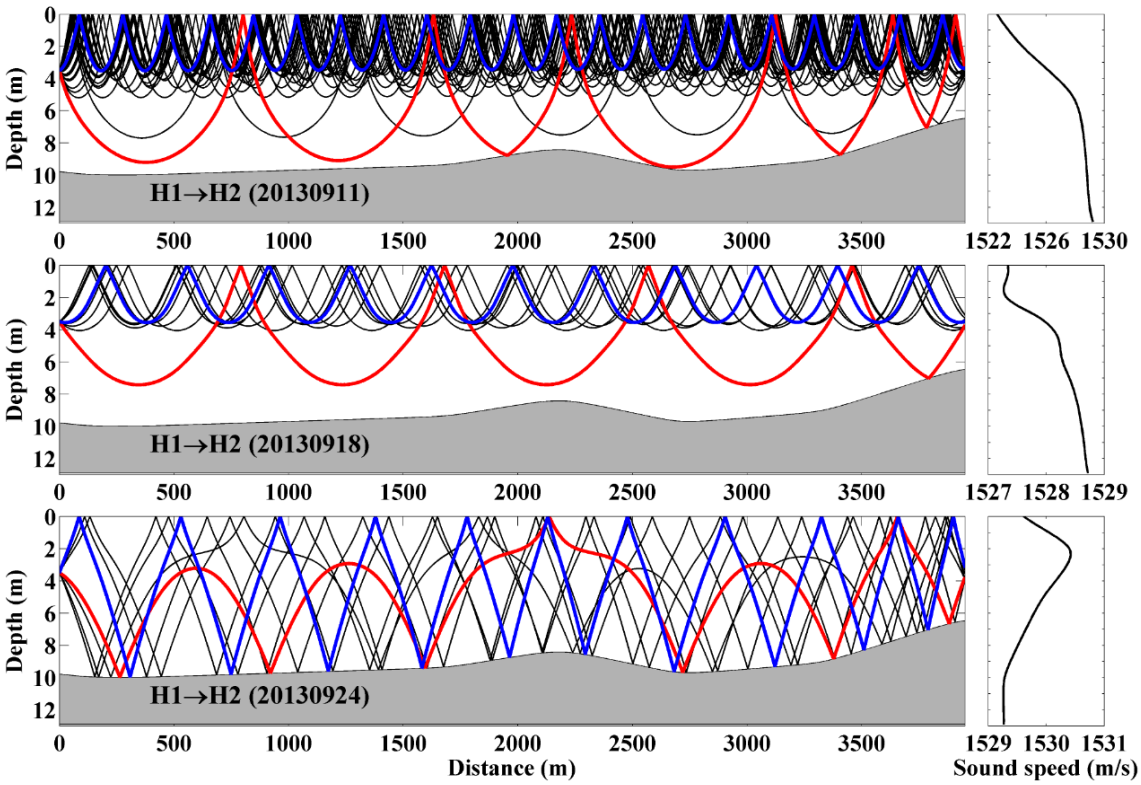

Fig. 6.1.3 *Results of the range-independent ray simulation along the H1-H2 line using the reference CTD data. The red and blue lines show the rays corresponding to the first and second arrival peaks, respectively, obtained in the field observation.*

6.1.3 Inversion for two rays and five layers

Figure 6.1.4 shows the time plots of 2-day low-pass filtered (LPF) current (positive taken from H2 to H1) and salinity, reconstructed by the vertical-slice inversion for 2-ray and 5-layer. For the data analysis, the weighting factor β=0.1 were selected to suppress the edge effect (Layer-1 and Layer-5). The salinity varies from 22 at the surface to 31 at the seafloor before the typhoon attack on 16 Sept. This salinity stratification is severely broken by the typhoon and the salinity values for all layers enter in the range of 30-31, implying the offshore transport of near-surface less saline water (Figure 6.1.4a). The 2-day LPF current shows a prominent estuary circulation, driven by Ota River, in Period 1 (pre-typhoon); the positive current in the upper layer (0-2 m) and the negative current in

the lower layer (4-10 m). During the upwelling (16-18 Sept.), the current become negative for all layers and increase with depth. The estuary circulation is weakly developed during 18-20 Sept. and during 24-26 Sept. It is possible that data quality is worse in periods apart from the CTD date because sound speed profiles in the periods without CTD data are interpolated by using the neighboring CTD data.

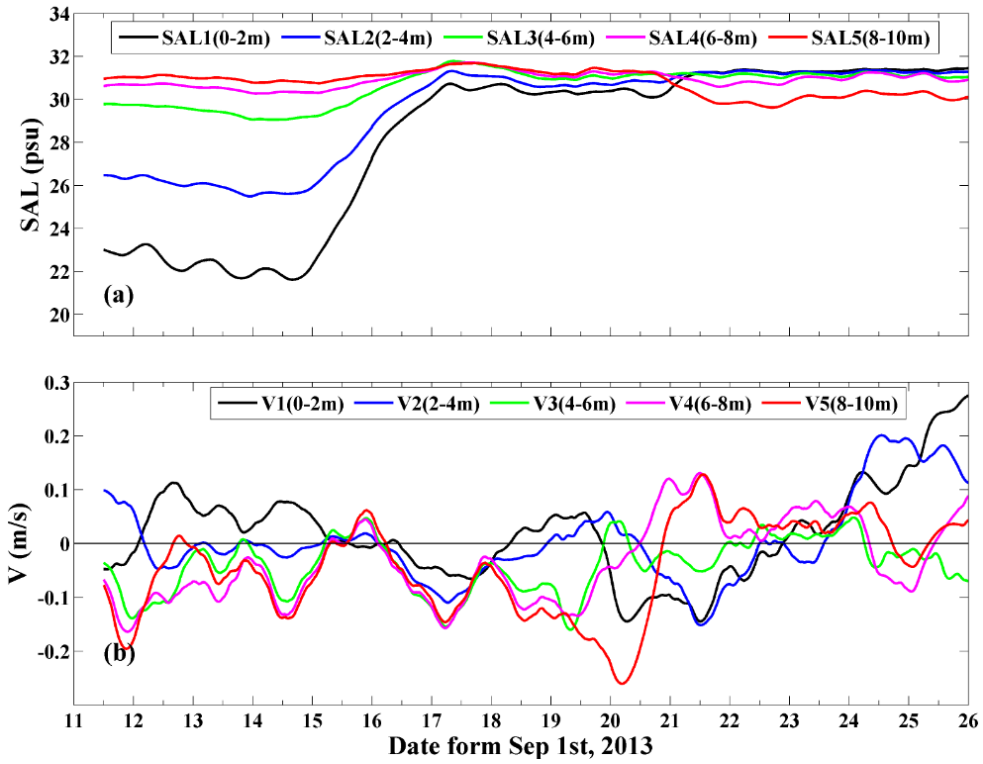

Fig. 6.1.4 *Time plots of the 2-day LPF (a) salinity and (b) current, reconstructed by the vertical-slice inversion for 2-ray and 5-layer. Black, blue, green, pink and red colors are assigned for the first (0-2 m), second (2-4 m), third (4-6 m), fourth (6-8 m) and fifth layers (8-10 m), respectively.*

The vertical profiles of range-averaged sound speed and salinity, reconstructed by the 2-ray and 5-layer inversion, are shown in Figure 6.1.5 and compared with the CTD data on 11, 18 and 24 Sept. The reconstructed sound speed agrees well with the CTD data while the reconstructed salinity underestimates the CTD data especially for the upper two-

layer. This underestimation is caused by that the sound speed is converted to the salinity from the sound speed formula [MacKenzie, 1981] using the one-point temperature array data. Note that no significant differences exist between the generalized and regularized inversions although errors and smoothing procedure are not considered in the former inversion [Bednar et al, 1992]. This means that little errors exist in the acoustic data.

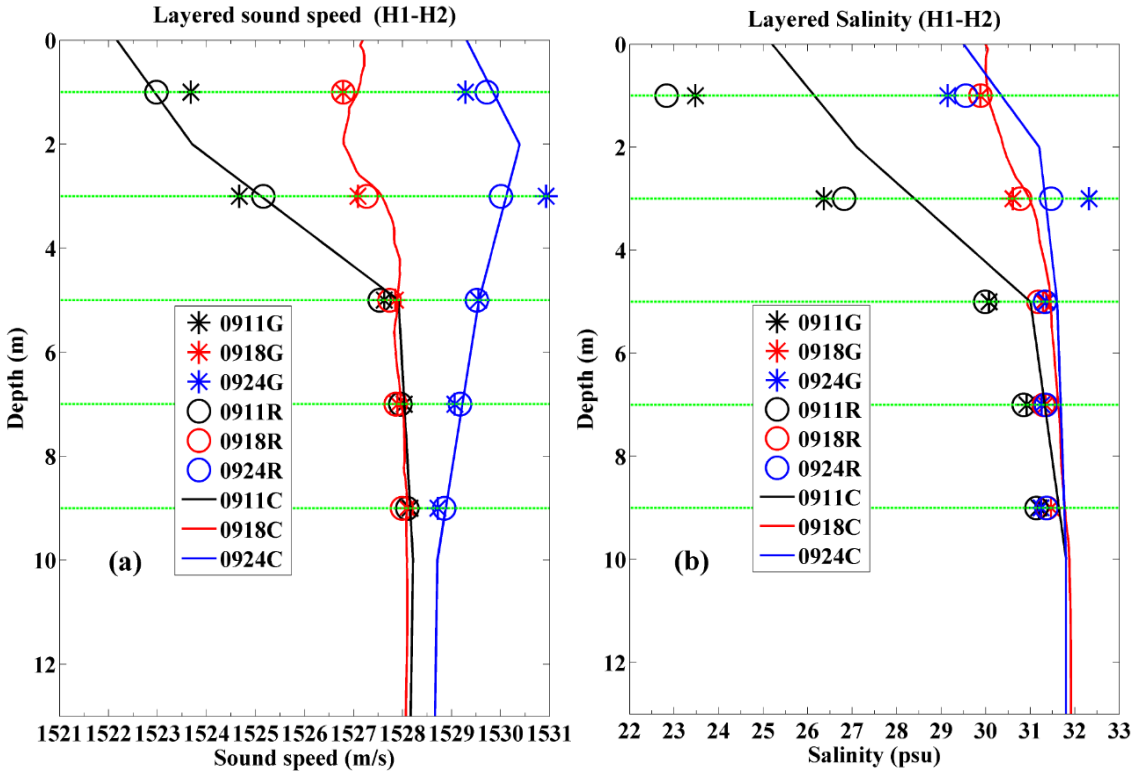

Fig. 6.1.5 *Vertical profiles of (a) sound speed and (b) salinity, reconstructed by the 2-ray and 5-layer inversion. Black, red and blue colors are assigned for the results on 11, 18 and 24 Sept, respectively. The ⋆ and ○ are used for results of the generalized and regularized inversions, respectively, and CTD results are indicated with the solid lines, assigned in the same colors .*

The 5-layer profiles of 2-day LPF current (positive taken from H2 to H1) are reconstructed using the data obtained on 11, 18 and 24 Sept. (Figure 6.1.6). It is clearly seen from the 11-Sept data that the 2-day LPF current is positive in the upper layer (westward) and negative in the lower-layer (eastward). This reverse current system is consistent to estuary circulation, derived from the Ota River discharge. Such reverse current systems is also visible in the 18-Sept and 24-Sept data.

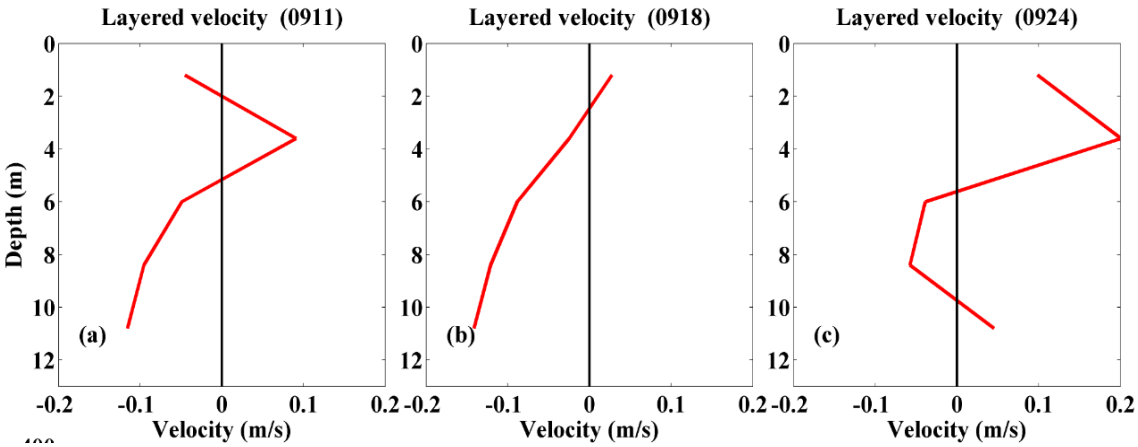

Fig. 6.1.6 *Five-layer profiles of 2-day LPF current, reconstructed using the data obtained on (a) 11, (b) 18 and (c) 24 Sept.*

6.2 Decreasing data gaps by reciprocal data

The number of data gaps is more increased in reciprocal data than in one-way data by the barrier effect of oyster rafts distributed on the sound transmission line and the unequal setting of system receiving gain. Then, better quality data sets are obtained for temperature data, calculated from the one-way data, rather than current data which require the reciprocal data. Generally speaking, the number of processed data decreases and data quality is improved when larger SNR thresholds is adopted. Oppositely, for smaller SNR thresholds, the number of processed data increase and data quality becomes worse.

The asymmetry of data acquisition is especially large between H2 and H3 in the Hiroshima Bay observation; data number much smaller at H2 than at H3. This is caused by that a same policy to select arrival peak data with SNR>4 is imposed on both sides. Data number at H2 is much increased by using the threshold SNR=2.5 as shown in Fig. 6.2.1(a). Reciprocal data between H2 and H3 are constructed with the different SNR thresholds, and currents are calculated from the modified data set (Fig. 6.2.1(b)). In this calculation of current, another constraint is introduced that data with the absolute current of $|V| < 0.2 ms^{-1}$ is selected. By this constraints, valid data in the worse quality station are retrieved from the noisy data because valid travel times in the worse quality station are close to those in the better quality station. The data number of current is significantly increased by picking up the low quality data at the worse station and introducing the constraint for current. Improvement is better understood by comparing with the data, obtained by taking the same threshold policy (SNR=4) for both the stations (Figs. 6.2.1(c) and 6.2.1(d).

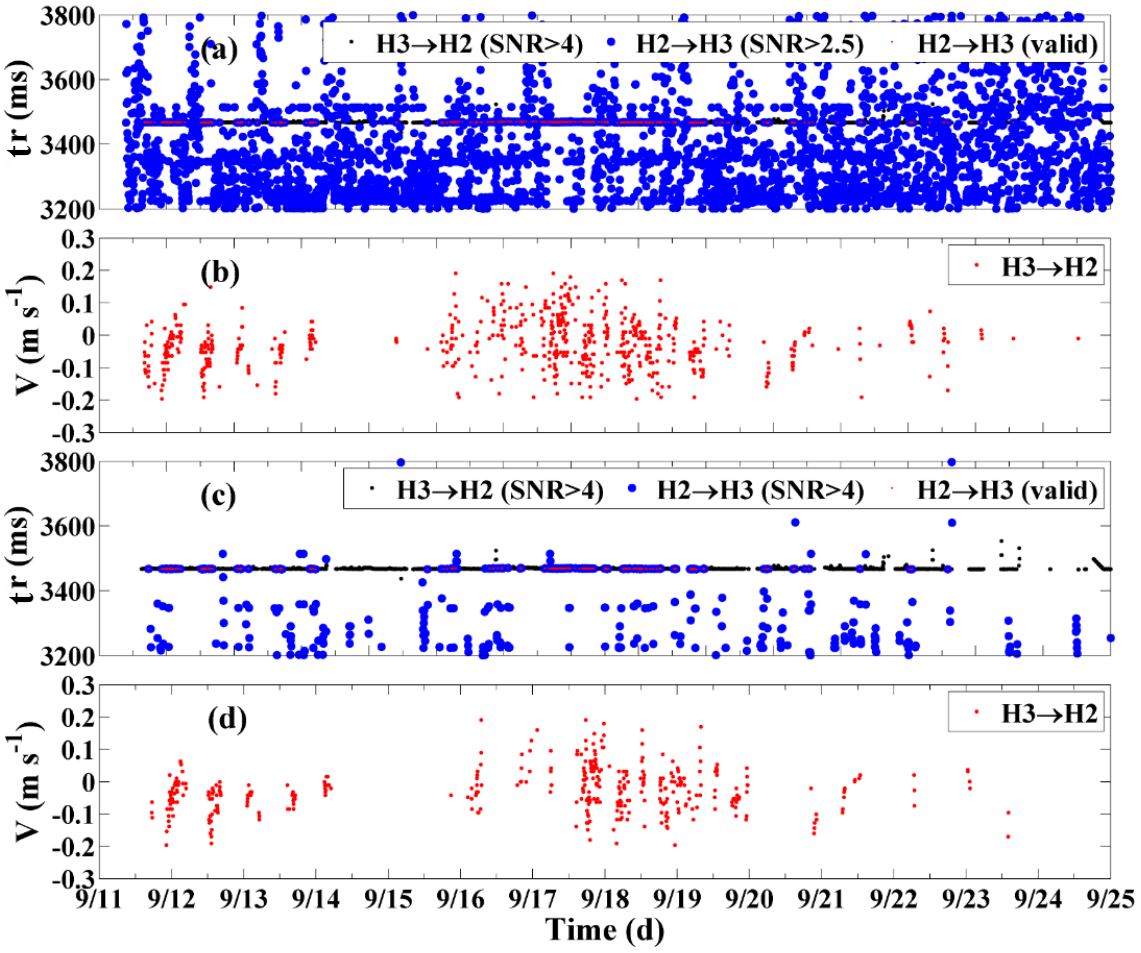

Fig. 6.2.1 *Improvement of the H2 data by using the smaller SNR threshold (SNR=2.5) and the constraints of the absolute current ($|V| < 0.2\,\mathrm{ms}^{-1}$) for the transmission line H2-H3. Results for the different SNR thresholds (SNR=2.5 and 4.0) and the same SNR threshold (SNR=4) are shown in (a) and (b), and (c) and (d), respectively.*

6.3 Function expansion method

It is likely that the function expansion method is not a suitable one in the analysis of Hiroshima Bay tomography data because the number of data is restricted to only five. The inapplicability is here verified by comparing the result of the grid method with that of the function expansion method.

As sketched in Fig. 6.3.1, the deviation of travel time summation $\delta\tau_i$ due to the sound speed deviation ΔC is formulated as follows:

$$\delta\tau_i = -2\oint_{\Gamma_i} \frac{\Delta C(x,z)}{C_0(z)^2} ds = -2\oint_{\Gamma_i} \frac{\Delta C(x,z)}{C_0(z)^2} \frac{dx}{\cos\phi} \tag{6.1}$$

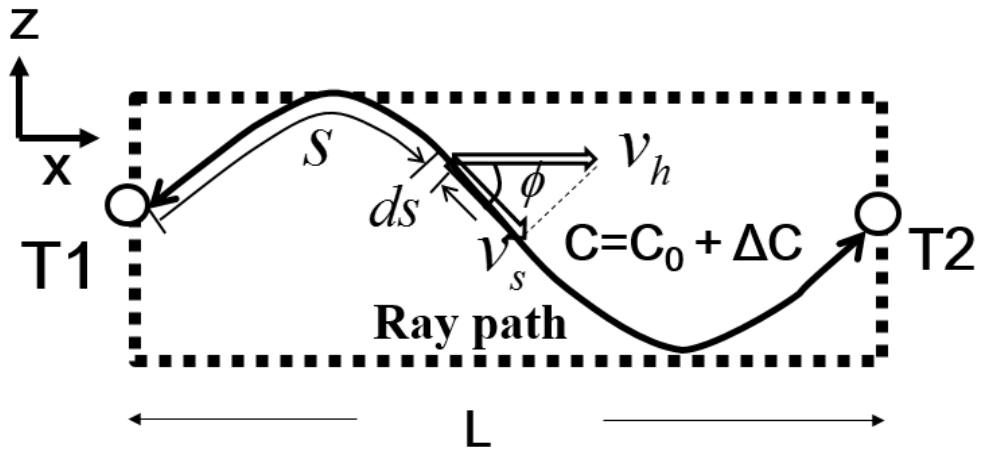

Fig. 6.3.1 *Sketch of the reciprocal sound transmission process between Stations T1 and T2.*

The unknown variables ΔC is expanded into a series of Fourier functions as follows:

$$\Delta C(x,y) = a + \sum_{k=0}^{N_x}\sum_{l=0}^{N_y}\left\{A_{kl}\cos 2\pi\left(\frac{kx}{L_x}+\frac{ly}{L_y}\right) + B_{kl}\sin 2\pi\left(\frac{kx}{L_x}+\frac{ly}{L_y}\right)\right\}$$
$$= \sum_{j=1}^{(N_x+1)(N_y+1)} D_j Q_j(x,y) \qquad (6.2)$$

where $\mathbf{D} = \{D_j\} = \{a, A_{00}, B_{00}, A_{01}, B_{01}, \cdots, A_{N_xN_y}, B_{N_xN_y}\}$,

$$\mathbf{Q}(x,y) = \{Q_j\} = \left\{1,1,0,\cos\frac{2\pi y}{L_y},\sin\frac{2\pi y}{L_y},\cdots,\cos 2\pi\left(\frac{N_x x}{L_x}+\frac{N_y y}{L_y}\right),\sin 2\pi\left(\frac{N_x x}{L_x}+\frac{N_y y}{L_y}\right)\right\}$$

where **D** are the unknown coefficient vector, and L_x=L_y=18 km is the side length of the square inversion domain, which is taken as twice that of the tomography domain. N_x and N_y are taken as 2 (9 km/cycle) in consideration of the data number of five and the resulting number of unknown coefficients becomes 9.

Substituting Eq. (6.2) into Eq. (6.1), we obtain

$$\delta\tau_i = \sum_{j=1}^{(N_x+1)(N_y+1)} D_j \int_0^{L_i} \frac{Q_j}{C_{0j}^2 \cos\phi}\, dx \qquad (6.3)$$

The unknown variables D_j are determined by the damped least squares method accompanied by the L curve method [Park and Kaneko, 2001; Yamaoka et al, 2002].

Figures 6.3.2 (a) and (b) show the horizontal distribution of temperature obtained by the inverse analyses (the function expansion and grid methods, respectively) for the data on 18 Sept. The horizontal temperature distribution measured at the same day by the CTD casts is also shown in Fig6.3.2 (c). It is clear that the result of the grid method is in better agreement than that of the function expansion method in the pattern of distribution. The temperature ranges from 24.05 to 24.4 ^{o}C for the function expansion method and from 23.95 to 24.35 ^{o}C for the grid method. The variation range of temperature obtained by the

grid method is almost the same as that of the CTD data. The suitability of the grid method is also confirmed by the difference with the CTD data (Figs. 6.3.3 (a) and (b)) and the expected errors (Figs. 6.3.3 (c) and (d)). The unsuitability of the function expansion method is also understood by the deviation from the CTD data (Figs. 6.3.3 (a) and 6.3.3 (b)) and the expected error (Fig. 6.3.3 (c) and 6.3.3 (d)). The difference with the CTD distribution range from 0 to 0.3 ºC for the function expansion method and from -0.1 to 0.15 ºC for the grid method. The expected errors are in the range from -0.05 to 0.15 ºC for the function expansion method and from 0 to 0.05 ºC for the grid method.

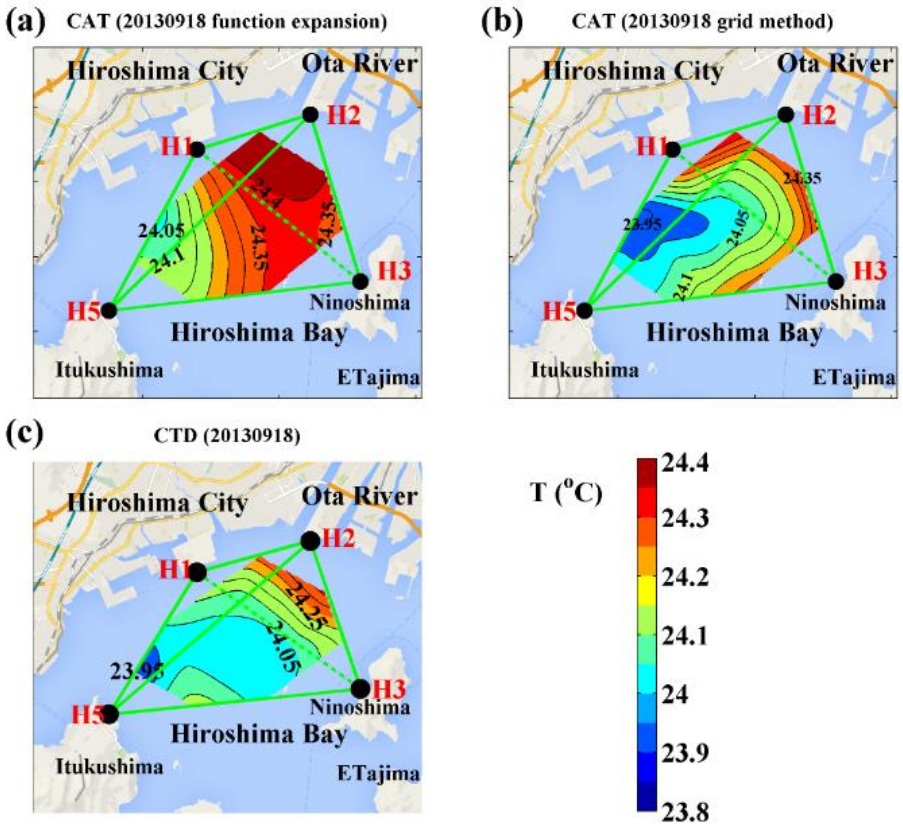

Fig. 6.3.2 *Horizontal distribution of the CAT temperatures on 18 Sept, reconstructed by the (a) function expansion and (b) grid methods. The CTD data obtained at the same date is shown in* (c).

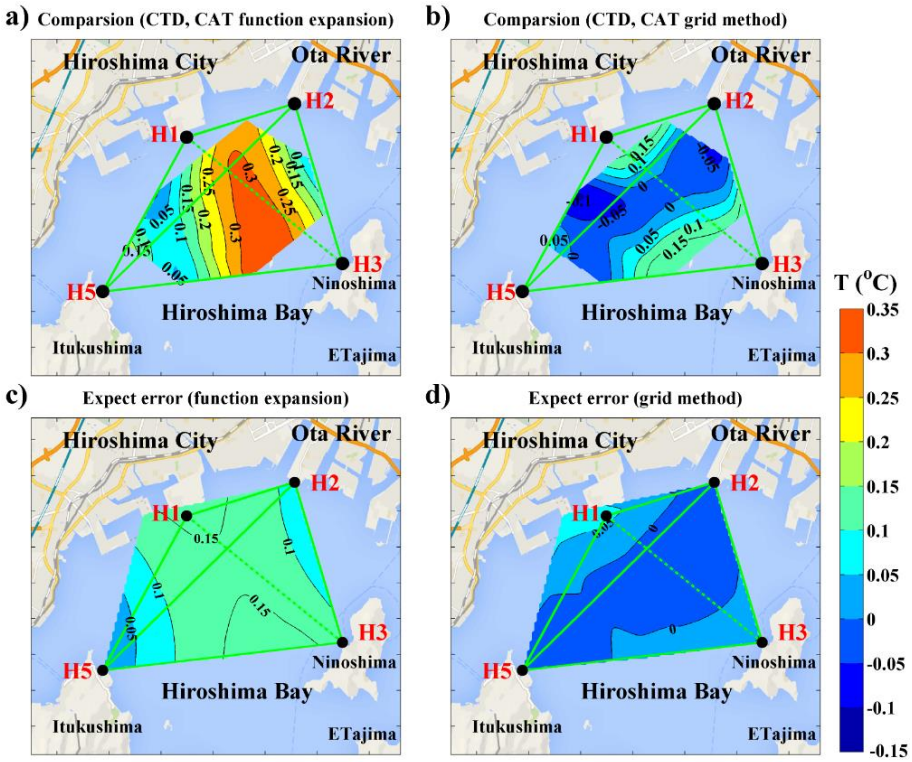

Fig. 6.3.3 *Differences between the CTD data and the CAT temperatures obtained by (a) the function expansion method and (b) the grid method. Expected errors for the function expansion method and the grid method are shown in (c) and (d), respectively.*

References

Bednar, J. B., L. R. Lines and R. H. Stolt. (1992). Geophysical Inversion, Philadelphia: Society for Industrial and Applied Mathematics, 453 pp.

Dushaw, B. D. and J. A. Colosi. (1998). Ray tracing for ocean acoustic tomography, Applied Physics Laboratory, University of Washington, APL-UW TM 3-98.

MacKenzie, K. V. (1981). Nine-term equation for sound speed in the ocean, *J. Acoust. Soc. Am.*, **70**, 807-812.

Park, J.-H. and A. Kaneko. (2001). Computer simulation of the coastal acoustic tomography by a two-dimensional vortex mode. *J. Oceangr.*, **57**, 593–602.

Yamaoka, H., A. Kaneko, J.-H. Park, H. Zheng, N. Gohda, T. Takano, X.-H. Zhu and Y. Takasugi. (2002). Coastal acoustic tomography system and its field application. *IEEE J. Oceanic Eng.*, **27**, 283-295.

Chapter 7 Conclusions

In Chapter 2, the forward problem of sound transmission is first formulated, and range-averaged sound speed and current are related to the travel time summation and difference, deviated from the mean travel time corresponding to the reference sound speed. Next, the grid-segmented method is newly proposed as a method suitable for the horizontal-slice inversion with a limited number of data (five in this study) instead of the well-used function expansion method. The layered method is also applied to the vertical-slice inversion. The expected solution and expected errors of unknown variables (sound speed and current) in segmented sub-domains (horizontal slice) and layers (vertical slice) are determined by the regularized inversion for both slices. The weighting factors are introduced to suppress the side and corner effects of sub-domain and sub-layer. Because strict accuracy less than 1 m is required to station-to-station ranges, special attention is paid to the position correction and a method in which the geographical position of the stations except for the reference station is taken to be unknown variables is newly proposed.

In Chapter 3, the anomalous sea level rises (ASLRs) sporadically generated as post-typhoon effects at the spring tide in September in Hiroshima Bay of the Seto Inland Sea are studied in this chapter. Major factors causing the sea level variations are examined in four time scales; the sub-tidal (2 d to 1 month), intra-seasonal (1 month to 8 months), seasonal (8 months to 2 years) and inter-annual (>2 years). The filter analyses for retrieving individual time scale data are applied to the HIROSHIMA tide gauge station data over 21 years (1991-2011) with an interval of 30 s. The major results obtained in Chapter 3 are summarized as follows:

(1) The total sea level variation has a standard deviation of 12.5 cm. The standard deviations are 3.4 cm, 9.8 cm, 4.7 cm and 4.2 cm for the inter annual,

seasonal, intra-seasonal and subtidal time scales, respectively.

(2) The intra-seasonal seasonal variation makes a significant contribution to the ASLR events of 2001 and 2011, with sea level rises of 12.2 and 8.4 cm, respectively.

(3) The sea level rise owing to thermal expansion is the largest in the seasonally warmest water in September. The sea level rises that reach 10 cm is a major factor of sea level variation in the seasonal time scale.

(4) In the sub-tidal time scale, the major source of sea level variations is provided by the upwelling and associated internal seiches or surges, generated around the northern coast of Hiroshima Bay by the northerly cross-shore wind. In September, a strong northerly wind is sporadically generated by the remote effect from the typhoon passages off the Kii Peninsula in the 400 km east of Hiroshima Bay, and the associated sea level changes reach about 10 cm or more. This post-typhoon effect played an essential role in the ASLR events which occurred in 1995, 2003, 2005 and 2011. The sea level rises were 11.6 cm for 1995, 15.5 cm for 2003, 10.5 cm for 2005 and 12.2 cm for 2011.

In Chapter 4, the long-term variations of current and temperature in 2012 were measured using reciprocal sound transmissions along the transect T1－T2 in the Aki-nada Sea of the Seto Inland Sea, Japan. The observed along-line current was converted to the estimated along-channel current with an angle correction of 49.5° from the sound transmission line and a phase correction of 1.17 h from the progressive wave using the nearest tide gauge station data and the long-wave equation. The error of path-averaged current measurement is ± 0.047 ms^{-1} for the hourly mean data and ± 0.007 ms^{-1} for the 2-day mean data. The error of sound speed measurement is ± 0.007 ms^{-1} for the 2-day mean data. The corresponding temperature error is ± 0.20 ℃. The 2-day mean

temperature showed a seasonal minimum of 10.1 ℃ on 10 March and a seasonal maximum of 25.9 ℃ on 17 September. Major results for the net transport across the Aki-nada Sea are summarized as follows:

(1) The monthly mean transport ranged from -22,845 m3s-1 (westward) in October to 2,566 m3s-1 (eastward) in July, implying possible seasonality (maximum in summer and minimum in winter).

(2) The net westward transport averaged monthly for the accurately observed period of six months was 13,107±2,544 m^3s^{-1}.

(3) The exchange time of inland sea water is estimated to be 778 days (2.1 years) for the observed net transport.

In Chapter 5, temperature variations caused by a typhoon were measured in the northern part of Hiroshima Bay by the four coastal acoustic tomography (CAT) systems. The horizontal distributions of depth-averaged temperature from 0 to 8 m were mapped at ten-minute intervals between the 11^{th} and the 25^{th} of September 2013. The major results obtained in Chapter 5 are summarized as follows:

(1) The horizontal distributions of a coastal upwelling and the associated diurnal internal tides were reconstructed well by the regularized inversion based on the grid segmented method, using one-way travel time data along five successful sound transmission lines.

(2) Station-to-station ranges were corrected in such a way that sound speed (determined from one-way travel time data) was equated to sound speed calculated from a couple of CTD datasets on each transmission line. In addition, all station positions were adjusted to make focal points at the geographical positions of the transducers. The corrections increased the accuracy of temperature measurements to make temperature errors as small as 0.073-0.079 ^oC. The high accuracy made it

possible to map the temperature structure with a variation range of less than 0.5 ºC.

(3) An upwelling grew from 16 to 17 Sept., owing to a typhoon-derived northerly wind. The diurnal internal tide resonated with the semi-diurnal external tide, which was pronounced after the upwelling decayed (18 Sept.), around the time the spring tide occurred.

(4) The upwelling and mixing fractions were formulated. These fractions increased continuously as the upwelling grew. Complete mixing was observed during the upwelling's mature phase.

In Chapter 6, the general discussion is presented.

Reciprocal data is discussed for the first and second arrival peaks in the best two-way data, obtained on the T1-T2 transmission line (closest to the Ota River mouth). Increasing scatters of the travel time summation and difference during Period 2 are visible especially in the first arrival data. Semidiurnal oscillation is also clear in the travel time difference data in Period 3. Ray paths corresponding to the first and second arrival peaks are obtained by the range-independent ray simulation using the CTD data. The vertical-slice inversion for the 2-ray and 5-layer is performed to reconstruct the vertical profile of range-averaged current and sound speed (converted to salinity by the sound speed formula). The reconstructed sound speed profiles are in good agreement with the CTD data on 11, 18 and 24 Sept while the reconstructed salinity underestimates the CTD data. A reason for this underestimation is that the sound speed-salinity conversion is done using the one-point temperature array data. The reconstructed current profiles show the typical pattern of estuary circulation that current is reversed between the upper and lower layers. The estuary circulation is largely disturbed during Period 2 owing to the typhoon effect.

A method of data improvement is proposed for a case in which the asymmetry of data number exists between the travel time data of two acoustic stations. The data number

for the station with smaller data number is increased by utilizing a smaller threshold of SNR and signals are retrieved from the increased noisy data by introducing a constraint for removing unrealistically large absolute current.

The suitability of the grid-segmented method rather than the function expansion method is confirmed with the Hiroshima Bay data.

Acknowledgements

This study was performed under the overall guidance of Prof. Arata Kaneko. I would like to express my gratitude of all those people who helped me.

First of all, I would like to thank my advisor Prof. Arata Kaneko for his patience, continue guidance and support during the whole period of study in Hiroshima University. I enjoyed the great benefit of Prof. Kaneko's meticulous working attitude of keep on improving and perseverant spirit of striving for perfection. It deeply affects my spirit and attitude of research, which made me busy and substantial in the last several years. Special thanks are extended to Prof. Noriaki Gohda for his kind advice and scientific suggestion in field observation and data processing.

I am deeply grateful to the members of the committee, Profs. Yasuaki Doi, Hironori Yasukawa, Hidemi Mutsuda and Kiyoshi Kawanishi (my sub-adviser) for their careful reading , valuable suggestions and helpful criticisms to the doctor dissertation.

I would like to thank Profs. Xiao-Hua Zhu (my former supervisor), Ju Lin and Drs. Masazumi Arai and Naokazu Taniguchi for providing valuable suggestions and contributions. Sincere appreciation is also expressed to former graduate students in our laboratory (Mr.takahashi, Mr. Hirose, Ms. Nakashima and so on) for their associate in the field experiment.

Finally I want to thank my parents, elder brother and sister-in-law for the long-term support to education and lift during the whole student period.